Theory of Lasing, Photon Number Squeezing and Thermal Emission in Quantum Dot Nanolasers

Mark Anthony Carroll

Computational Nonlinear Quantum Optics - CNQO

Department of Physics

University of Strathclyde, Glasgow

18/10/2021

This thesis is the result of the author's original research. It has been composed by the author and has not been previously submitted for examination which has led to the award of a degree.

Signed: Mark Anthony Anthony Carroll

Date: 18/10/2021

Abstract

We develop quantum models capable of describing laser action from the fundamental limit $\beta = 1$ to the thermodynamic limit $\beta \to 0$. By including the variables that describe incoherent and coherent emission we are able to fully characterise the laser threshold as a function of the pump power independent of system size. The case of the so-called "thresholdless" laser where $\beta = 1$ is examined and through bifurcation analysis the true laser threshold is found. The model equations are solved analytically as is the equation for the second-order intensity correlation. We show cases where antibunching is predicted and observe that there is a distinct path of emission for lasing devices as the pump is increased: from thermal to antibunching to coherent. We exploit antibunching regime that preceding the lasing regime by proposing a simple experimental setup capable of producing up to 3 dB photon number noise reduction in comparison with coherent emission. There is moderate output power in the range of pW and we show that effects due to pump fluctuations are negligible. We also show that in the thermodynamic limit our model is capable of recovering the classical laser threshold for macroscopic lasers.

Contents

List of Figures

Acknowledgements

I would like to thank my supervisors Dr. Francesco Papoff and Prof. Gian-Luca Oppo at the University of Strathclyde and my external supervisor Prof. Gian Luca Lippi at Université Côte d'Azur. I would also like to thank Prof. Giampaolo D'Alessandro at the University of Southampton. I am extremely grateful to every one of you for your support.

Chapter 0. Acknowledgements

Chapter 1

Introduction

The advent of the laser, which is an acronym for Light Amplification by Stimulated Emission of Radiation, has been instrumental to the advancement of modern science and technology. It's applications range from laser cooling atoms in the formation of Bose-Einstein condensates to manipulating small particles with optical tweezers [4]. In recent years a lot of attention has been given to nanolasers with semiconductor quantum dots (QD) as the active material. These nonolasers have dimensions on the order of the wavelength of the emitted light resulting in a low modal volume, and along with high Q-factors allow for strong light-matter coupling.

From a research point of view nanolasers offer attractive opportunities to study exotic behaviours in a new quantum limit. It has been shown that these devices display non-classical photon statistics for few emitters such as photon anti-bunching [5, 6]. And a unique characteristic of these devices is that the signature of a lasing threshold disappears [1, 7]. A result of this thresholdless lasing behaviour is that the criteria for lasing has to be reexamined as it is no longer clear when the light emission changes from thermal to coherent. Typically, the input-output curves (I-O) of lasers show the classic s-shape with a well defined laser transition but for nanolasers this disappears and the input-output curve is linear with an ill-defined transition. This can be characterised by the spontaneous emission factor, β, which is the ratio between the spontaneous emission rate into the dominating lasing mode to the total decay rate. For nanolasers $\beta \to 1$ and for standard macroscopic lasers $\beta \approx 10^{-5} - 10^{-8}$.

The motivation behind understanding these devices better is not just academic. Nanolasers with QD gain media have potential for use in future applications where they can be integrated with electronics i.e. on-chip devices and optical interconnects. This desire is driven by the reduced power consumption and low footprint these devices promise. Therefore, a better understanding of nanolasers is paramount if we are to continue with the miniaturization and enhancement of the technologies that govern our world. In this thesis, a theory to describe photon statistics in nanolaser regimes and predict a laser threshold in the nanolaser limit is developed using semiconductor quantum dots (QDs) as the active medium. Specifically, we employ self-assembled Stranski–Krastanov quantum dots, which offer significant advantages over traditional quantum wells due to their strong 3D carrier confinement and high emission efficiency. These QDs are embedded in semiconductor materials, where interactions between localized carrier states and those in the wetting layer enable fast scattering processes, making them ideal for efficient electrical pumping—key for optoelectronic applications. By investigating nanolaser behavior, particularly in the few-emitter limit, we aim to explore non-classical light generation, an essential aspect for quantum information technologies. This choice of QDs not only allows us to probe the crossover from classical to non-classical light sources but also sets the stage for understanding their role in advancing quantum technologies. In the following chapters, we will build on this foundation, analysing nanolaser operation, coherence properties, and emission characteristics in greater detail.

In **Chapter 2** section will focus on the unique behaviours shown by QD nanolasers. This will be highlighted by the need to extend our analyses of the laser dynamics in order to better understand emission properties and potential limitations of the devices. To do this a simple rate equation model will be investigated which can be derived from a master equation using well-founded approximations. And it will be shown how this model is capable of predicting features displayed experimentally.

In **Chapter 3** we develop the system Hamiltonian and introduce the concept of the cluster expansion which allow us the construct the equations of motion. We derive the models in terms of correlation functions and then as expectation values (EVs).

In **Chapter 4** we discuss the flluctuations in the coupling strength between e.m. field in the cavity and QDs which can be ascribed to the positioning relative to the local field value and inhomogeneous broadening of the QD ensemble.

In **Chapters 5** and**Chapters 6** we look at the results of our model before proposing a simple scheme to take advantage of the quantum light predicted by the model. Finally, **Chapter 7** concludes the thesis.

Chapter 2

Overview of lasers

In 1916 Albert Einstein laid the foundations for the laser with the concept of stimulated emission in the paper titled - "On the Quantum Theory of Radiation". This mechanism of producing radiation from excited atoms or emitters prompted Charles Townes and Arthur Schawlow to start working on the maser - microwave amplification by the stimulated emission of radiation - which was the precursor of the laser and used alkali vapour as the gain medium [8]. The maser worked off of the same basic principles as the laser except from the fact that it did not produce radiation with wavelengths in the visible spectrum. The first device capable of producing visible radiation was developed by Theodore Maiman in 1960 whilst working laser at Hughes research lab in America [9]. The overall device size was small enough to fit in a human hand and consisted of a solid-state gain material of ruby crystal which was optically excited by a flashlamp and feedback was provided from two mirrors at either end of the cavity. At the time it was dubbed as a "solution looking for a problem" with many failing to see its usefulness.

2.0.1 Advances and Applications

Since the first solid-state ruby laser there has been an explosion in terms of the variety of gain medium used as the active material as well as the geometry of the resonators required to provide feedback. Not long after the first demonstration of the solid-state ruby laser the gas laser was introduced - the gas in question was a helium-neon vapour.

Gas lasers were the first to to work of off the principle of converting electrical energy into coherent radiation. Some of the advantages of gas lasers compared with their solid-state counterparts include: rapid heat dissipation from the resonator; lower cost as the active material is relatively inexpensive; it is almost impossible to damage the gain material; and, there is a higher volume of the active material which ensures maximum overlap with the modal volume thus greater conversion efficiency. Although the gas laser has a number of advantages it have failed to dominate in applications. This is in part thanks to the inability of the gas laser to minatuarize. Solid state lasers on the other hand have seen rapid minituarization over the last few decades. This has opened up the path for solid state lasers to be integrated with opto-electronic systems and utilised in optical fibre telecommunication where the traffic is expected to grow rapidly in the coming years. Micro- and nano-lasers can also operate in exotic regimes where non-classical light is observed. This has various potential applications in continuos-variable quantum information processing [10] as well as gravitational wave detection [11].

Nowadays, one cannot set their gaze upon an object without it either being manufactured with the aid of a laser or casing a laser within. Lasers are ubiquitous in todays society and their usefulness does not stop at barcode scanners or lighting displays. It is not just the active materials that have changed dramatically but also the dimensions of the devices. Pushing the limits experimentally and theoretically has always been a major driving force in creating devices at the cutting edge of technology - this force permeates all science. This is perhaps most apparent in the evolution of the laser which has seen huge advances, with a ferocious pace, in both macroscopic and micro-and nanolasers.

From its genesis the laser has been fundamental in reshaping and revolutionising sources of medical treatment. The highly coherent and concentrated radiation produced by a laser makes it ideal for destroying tumours and eye surgery both of which require high level precision not thought possible before the introduction of the laser.

Lasers are also helping to usher in a new era in astronomy in the form of gravitational wave astronomy. In 2016 the first detection of gravitational waves was detected at LIGO - Laser Interferometer Gravitational-wave Observatory [12]. The interferometer itself

consists of two 4 km long arms with mirrors at both end where a laser beam being split down each arm. If a gravitational wave passes through the site it will cause a disturbance in space-time by stretching one arm and squeezing the other, this will cause an interference pattern to be observed. The mount by which the arms are moved is 1000 times smaller than the nucleus of an atom which illustrates the precision needed to be capable of detection. This would not be possible without lasers.

Another large laser based collaboration is taking place at the National Ignition Facility (NIF). The facility is three times the size of a football field and houses a chamber where the collective energy of many lasers is directed towards a small cell of hydrogen fuel with the goal being to achieve fusion ignition. The powerful lasers are attempting to recreate the conditions at the centre of the sun where hydrogen atoms are fused together to create helium atoms giving off huge amounts of excess energy in the process.

2.0.2 VCSELs

The first major breakthrough towards laser miniaturisation came in the from of the VCSEL [13, 14] (vertical cavity surface emitting laser). The VCSEL was developed in the 1980's paving the way for extreme miniaturisation in lasers, and at the time boasted the smallest active material volumes ever constructed. The first VCSELs active region consisted of single or stacked quantum wells, but since then many many different gain materials have been used such as quantum dots (QDs) [15] and organic semiconductors [16]. The laser resonator is composed of two distributed Bragg reflector (DBR) mirrors where the active material is sandwiched between them. The DBR mirrors achieve very high reflectivity by layering or alternating materials with different refractive index next to one another; this layered structure comes at the cost of increased thickness of the device. However, the high reflectivity results in large Q-factors and long photon lifetimes within the cavity.

There are obvious benefits in the reduced dimensions of smaller lasers such as increased speed compared with electronics. Electronic components depend on electrons travelling through the wires encountering resistance slowing them down, whereas, pho-

tons emitted from micro- and nanolasers travel at the speed of light virtually unimpeded allowing for faster signal transmission. In the case of optical-interconects it can reduce interconnect energy by eliminating the charging of electrical lines. However, there are complex trade off's to be made when considering the applications of a potential device. For example, depending on what the laser device is being developed for it may be advantageous to have low photon lifetime or long photon lifetime within the cavity [17]. If the device is to sustain low-power operation then a long photon lifetime is desirable. This is in order to reduce the material gain needed to achieve threshold.

2.1 Overview of theory

Typically, three- or four-level models are employed to investigating lasers [18], however, it is possible for them to be reduced to two-levels via adiabatically eliminating the additional levels. If we assume the decay rates of the additional levels are fast compared with the lasing levels they can be adiabatically eliminated. Alternatively, to approximate a two-level system we can think about this in terms of the frequency of the light-field interacting with the lasing levels. In a classical picture the light incident on an atom will induce dipole oscillations. Dipoles are created when incoming light causes the electrons and nucleus to separate polarising the atom in the process. The dipoles are then forced to align in the direction of the propagating light field and begin radiating at the frequency of the incoming field. If the frequency of the field is resonant with an optical transition or natural frequency of the atom then the dipole oscillations will be large and the light-matter interaction will be strong. If, however, the angular frequency of the light does does not match a natural frequency of the atom the dipole oscillations will be small and the light-matter interaction will be weak. Therefore, to a good approximation we can neglect the other levels of the atom as they are said to be off-resonance.

When we think of two-level systems like this it is normally in terms of an atomic species, however, two-level models of this kind can be used to model semiconducting QD nanolasers [19]. In this case decay from the excited to the ground state can be viewed as the re-combination of an electron from the conduction band with a hole from

the valence band.

If we start from a two-level system in free space initially in an excited state then there is a finite probability it will decay to the lower state. In the process of doing so a photon will be released in a random direction with energy equal to the separation between the two levels, known as spontaneous emission. Although our system may seem isolated it is in fact coupled to the electromagnetic field in its vacuum state - the vacuum field. As a result we can think of spontaneous emission as a stimulated emission event triggered by a perturbation from the vacuum field. These perturbations stem from the inherent fluctuations of the vacuum field known as quantum fluctuations.

2.1.1 Quantum fluctuations

The quantum harmonic oscillator is the basis for the quantum theory of light. The electromagnetic field can be described as an infinite set of harmonic oscillators with the energy of each state given by

$$E_n = \left(n + \frac{1}{2}\right)\hbar\omega \tag{2.1}$$

where ω is the angular frequency of the light, $\hbar$ is Planck's constant, and the index $n = 0, 1, 2, ...$ [20]. From Eq. (2.1) when $n = 0$ the energy of the quantum oscillator is $E_0 = \frac{1}{2}\hbar\omega$, this is known as the zero-point energy of the oscillator. This shows that with no photons present there is still a residual energy. This residual energy comes from the vacuum state, $|0\rangle$ (given here in Dirac notation). Fluctuations in the energy of the electromagnetic vacuum field are what give rise to the zero-point energy of the vacuum state. Consider an evacuated cavity with a volume V and at a temperature where the thermal energy is significantly lower than the quantum energy of the oscillator. In this instance the zero-point energy can be equated to the electromagnetic energy within the mode volume. The resulting magnitude of the vacuum field is then given by

$$E_{vac} = \left(\frac{\hbar\omega}{2\epsilon_o V}\right)^{1/2} \tag{2.2}$$

where V is the cavity volume and ϵ_0 is the electric permittivity of free space [20] . From Eq. (2.2) it is clear that the amplitude of the vacuum field fluctuations is greater for

small cavities.

These vacuum field fluctuations can be understood in terms of Heisenberg's indetermination principle which states

$$\Delta E \Delta t \geq \frac{\hbar}{2} \tag{2.3}$$

where ΔE is the uncertainty in the energy and Δt is the uncertainty in the time. From Eq. (2.3) one can see that for the inequality to hold true a large uncertainty in the energy results in a very small uncertainty in the time (and vice versa). This means that pairs of massive particles can come into existence for an extremely brief moment before annihilating one another. These extremely short-lived particles are known as virtual particles. As a result of this uncertainty in the energy, the vacuum is constantly writhing and seething with short-lived virtual particles coming into and out of existence. This process has been likened to a "quantum foam". It is the fluctuations of the electromagnetic field in its vacuum state that cause the quantum phenomenon of spontaneous emission by perturbing the upper state of an emitter.

By putting our system inside a cavity we can either enhance or inhibit spontaneous emission. The cavities most commonly used in the production of nanolasers are called Fabry-Perot resonators. These consist of two highly reflective mirrors with one mirror with some small transmissivity allowing for light output, and their volume is around that of the wavelength of the emitted light cubed. When a photon is emitted spontaneously in free space it will travel in a random direction. However, if we introduce a cavity with curved mirrors we are able to keep the photon inside the cavity for many round trips. And by using cavities with high Q-factors can increase the amount of time the photon interacts with the QD. When a light field is present inside the cavity it will bounce around and interfere constructively giving rise to resonant modes of the cavity where the fields amplitude is greatest. The properties of these resonant modes play an essential role in determining the emission spectra of lasers. By placing a QD on a node of a resonant mode we can enhance the light-matter interaction or inhibit it by placing it off-resonance. The presence of vacuum field fluctuations not only triggers spontaneous emission but results in some interesting quantum phenomena such as the

Casimir effect [21]. The Casimir effect occurs when two metallic plates are placed close to one another resulting in a force - the Casimir force - pushing the two plates together. Vacuum fluctuations born out of virtual particles that arise from the uncertainty principle have many wavelengths. When the two plates come together particles with larger wavelengths cannot exist between them. Therefore, there will be a difference in energy density between the two plates compared with outside the plates resulting in an attractive force between the two plates.

Another consequence of these fluctuations is the Lamb shift of the hydrogen atom. The interaction between vacuum fluctuations and the electron of hydrogen causes the $2s_{1/2}$ state to have a slightly higher energy than the $2p_{1/2}$ state. This results in a shift of the corresponding spectral lines of hydrogen.

Intrinsic to the electromagnetic field is its fluctuations in the case when there are no photons present. It is the fluctuations of the vacuum state that explain why the coupling of a two-level system such as the hydrogen atom with this quantised field alters its properties. Thus, without knowledge of quantum fluctuations and its origins we would not be in a position to explain the rich and exotic behaviours it brings about.

2.2 Experimental markers and how to identify a laser

One particular aspect of the laser that is surprisingly still debated to this day is the laser threshold. In particular, the laser threshold of high-β lasers. So much so that it in response, more than 60 years after the first laser was demonstrated and almost 40 years since laser miniaturisation took off in the 1980s, there are still articles being published asking the question "what is laser threshold?" [22]. An early effort was made by Rice and Carmichael to view threshold in terms of the Fano factor [23], a method that required knowledge of the photon statistics. As a result, there is an active effort to consolidate the criteria on how to recognise lasing and to help separate true lasers from devices masquerading as lasers. There are four key criteria given in [24]: (1) narrow spectral linewidth; (2) the output beam has high directionality; (3) the emission is characteristic of the active material and resonator geometry; and (4) there is to be a

clear threshold for both the intensity and linewidth as a function of the pump. The first three key points are easily verified experimentally, but it is the latter point regarding clear thresholds for the intensity and linewidth that becomes ambiguous for small lasers.

For macroscopic lasers, identifying the laser threshold is not a particularly difficult task. If one were to inspect the intensity as a function of the pump on a log-log plot, then one would observe an S-shaped curve which is characteristic of low-β lasers. The S-shaped curve is composed of a lower branch at low pump values and an upper branch at high pump values that run parallel to one another and are connected by an almost discontinuous jump for large lasers. This jump between the two branches is typically proportional to the reciprocal of β; the point of inflection where the upper and lower branch meet is considered to be the location of the threshold. In a similar fashion, the reduction in linewidth as the pump is increased for macroscopic lasers exhibits a definite threshold. We can, however, call into question the validity of using the linewidth as an indicator of lasing. A reduction in linewidth is synonymous with the a laser operating well above threshold, but a low bandwidth filter is capable of spectrally filtering thermal light. In this case there is certainly a reduction in the linewidth of the device, yet, there are tools we can use that will betray the fact that the radiation is not coherent. Nevertheless, according to the above criteria macroscopic devices do not pose a significant challenge when identifying laser action.

As β approaches unity it becomes more difficult to identify the position of the laser threshold due to the fact that the characteristic S-shaped curve becomes smoother until, in the ultimate limit of $\beta = 1$, it becomes a straight line. At that point, there is no information to be extracted from the I-O curve and it appears as though the threshold is at zero pump value. This is where the terms "thresholdless" [7] and "zero-threshold" [25] lasers come from. There are some cases where taking the first and second derivatives of the I-O curves highlights the response around threshold, i.e. a sharp peak, but ultimately in the limiting case of high-β this is washed out and no extra information is forthcoming. There is a subtlety between zero-threshold and thresholdless that is worth remarking.

In the case of a zero-threshold, what is meant is that there is no threshold and the

emission is coherent from the zero-pump power, i.e. always coherent with no losses to overcome. It was pointed out in [23] that the equation that shows this behaviour was derived in the thermodynamic limit and as such should not be applied in the limit of high-β. In the case of thresholdless this means that due to the smoothing out of the I-O curve the threshold region spreads out to the point that there is no clear cut threshold location but a broad region of the pump where the emission slowly becomes coherent. In this limit, then, it is not viewed as a second-order phase transition which is only well defined in the thermodynamic limit. This begs the question: how can a true laser threshold be defined in the limit of $\beta = 1$?

2.2.1 If not I-O then what?

In terms of experimental evaluation of the laser threshold, one technique that relies on computing correlation functions has proved extremely useful in the limit $\beta \to 1$. The most widely measured being the first-order and second-order correlation functions. The former is used as a measurement of the coherence time of the device (as well as measuring the visibility of interference fringes) and thus gives information based on the linewidth of the emitted radiation, while the latter is used to identify the *type* of light that is being emitted. As discussed above, linewidth measurements on their own are not always the best measure of laser threshold. Therefore, it is the second-order intensity autocorrelation function, $g^{(2)}(\tau)$, that is employed to find the laser threshold of small lasers where knowledge of the type of light being emitted is indispensable in determining lasers from laser-like LEDs [15].

The most general expression of the second-order intensity correlation is given by:

$$g^{(2)}(\tau) = \frac{\langle I(t)I(t+\tau)\rangle}{\langle I(t)\rangle^2}, \tag{2.4}$$

where $I(t)$ and $I(t+\tau)$ are the intensities at time t and $t+\tau$, respectively; τ is the delay time between the measured intensities. It was the famous Hanbury Brown-Twiss experiments, first used as stellar interferometers, that led to the idea of the second-order correlation function. The set up is consists of an input beam from a source which

is met by a 50 : 50 beam splitter sending the beam down two different paths. The two distinct outputs are detected by photomultiplier tubes (PMT) and sent into an electronicmultiplier–integrator, where the intensity correlation is proportional to the two photocurrents. A delay τ is also introduced to one of the beams by way of change the length of one of the paths. However, it is the second-order intensity correlation at zero delay time which is used experimentally.

Light can be separated into three categories given by the different limits of $g^{(2)}(0)$, see Fig. 2.1. Thermal light is identified by photons that *bunch* together where $g^{(2)}(0) > 1$, i.e. the light emitted from a broadband source such as an incandescent lightbulb. Whereas, perfectly coherent emission of time-independent intensity and phase is defined by $g^{(2)}(0) = 1$; it is clear from Eq. 2.4 that when $\tau = 0$ the measured result is $g^{(2)}(\tau = 0) = 1$ when $I(t)$ is constant. The third and final type of light is defined by $g^{(2)}(0) < 1$ which is forbidden in the classical interpretation of light, thus is known as quantum light. Values of $g^{(2)}(0) < 1$ can only be understood if one ignores the classical view of light being an electromagnetic wave and instead treats the emission as a beam of individual photons. A characteristic trait of quantum light is the apparent ability of photons to space themselves out, this has come to be known as photon *antibunching*. The first experimental observation of the quantum phenomenon of antibunching was by Kimble et al. in 1977 [26]. Recently, experiments using micropillar lasers with semiconductor QDs have observed antibunching, where the effective number of QDs interacting with the cavity mode was estimated to be 15 [27].

It is instructive to consider the statistical information of the different types of light in the photon interpretation in Fig. 2.1; an important subtlety is conveyed in the following. Let us first consider the photon statistics of a perfectly coherent beam of light. In this case, the photons are arranged randomly within the stream and as a result obey Poissonian statistics. Poissonian statistics have the property that the relative fluctuations around the average value are given by:

$$\frac{\Delta n}{\langle n \rangle} = \frac{1}{\sqrt{\langle n \rangle}}, \tag{2.5}$$

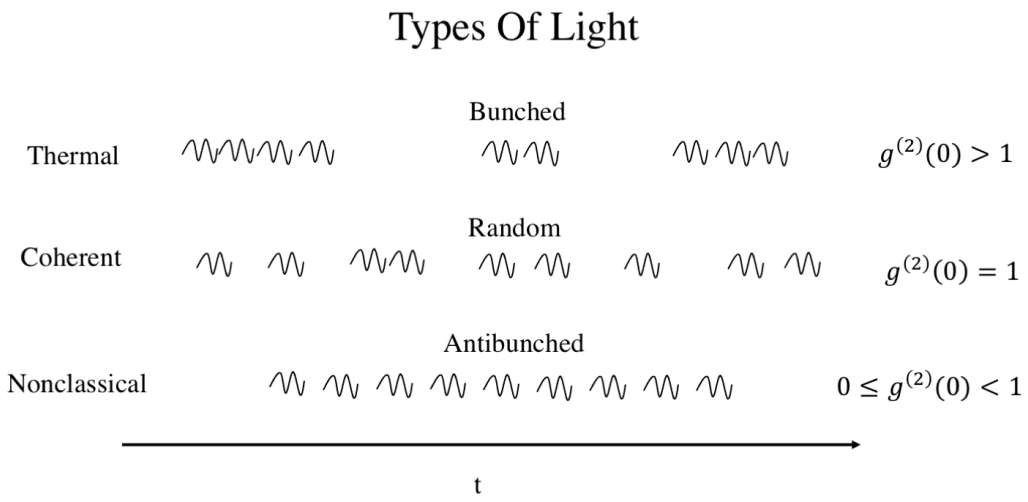

Figure 2.1: Schematic illustration of the three different types of light when viewed as a stream of photons and the values of $g^{(2)}(0)$ taken by them. Knowledge of the temporal evolution of the photon stream helps one determine the type of emission being emitted.

where Δn and $\langle n \rangle$ is standard deviation and average photon number, respectively. From Eq. 2.5 it is clear to see that in the limit of large average photon numbers the relative fluctuations are reduced dramatically (classical limit) compared with small average photons where the flucuations are large (quantum limit). Super-Poissonian statistics have the property of $\Delta n > \sqrt{\langle n \rangle}$ and sub-Poissonian statistics have the property that $\Delta n < \sqrt{\langle n \rangle}$. Therefore, classical thermal light which has large photon number flucuations, i.e. bunching, is associated with having super-Poissonian statistics and antibunched light, which has intrinsically less noise than a coherent source, is associated with sub-Poissonian statistics. However, an important point of note is that sub-Poissonian photon-counting statistics need not imply photon antibunching, but can in fact be accompanied by photon bunching as was shown by Zou and Mandel [28].

From the above discussion it is clear that identifying the laser threshold for devices in the limit of $\beta \to 1$ is a difficult task and that one cannot rely on any single experimental tool or marker. Instead, several characteristic traits such as linewidth reduction, $g^{(2)}(0) = 1$ and high beam directionality are needed simultaneously. However, the dif-

ference between measurements mentioned aboove in the thermodynamic limit and the limit in which $\beta \to 1$ is that in the former there is a second order phase transition, i.e. there is a finite vlaue of the order parameter at which the state changes equivocally. In the case of small lasers there is no second-order phase transition as it is not defined - it can only be defined for infinite system sizes. Thus, even with all the simultaneous markers the *true* laser threshold is washed out and ill-defined, we can only see the effects after coherence builds up in the system. Nevertheless, is has been well known since the early 1960s that the difference between thermal and coherent light is that in the latter the average value of the coherent field amplitude is non-zero, whereas in the case of the former it is exactly zero [29]. This precise and well defined definition of laser threshold opens the opportunity to be exploited and could provide an exact mathematical description of the laser threshold in small lasers without ambiguity.

2.3 Modelling

An important question one should ask is the following: In solving a particular system of equations, or model, what information can be gained? There are various types of models currently employed to better understand lasers and the effects of their operation. These include rate equations (REs) [1, 7, 23, 30, 31], a master equation approach [23] and cluster expansion quantum elcetrodynamics models [5,15,31] (CEQED). How much information can be captured from them depends on their level of sophistication, i.e. whether or not statistical information about the emission can be drawn etc. Therefore, from an applications point of view, this information is crucial and can determine which approach is best suited to the problem.

The very first lasers were described incredibly well mathematically by the eminent Maxwell-Bloch equations which constitute a semiclassical theory; the field is treated classically and the matter quantum mechanically. They were table-top devices and as such came well within the jurisdiction of the thermodynamic limit, i.e. $\beta \to 0$. In this limit, there is no ambiguity concerning second-order phase transitions and the Maxwell-Bloch equations show clearly a definite laser threshold at finite pump energy. However, what they do lack is the capability of describing the incoherent emission

that precedes the laser threshold. This is because the photon number solution is zero below threshold; the non-zero coherent photon field emerges through a transcritical bifurcation only for pump powers above threshold. As such, when it comes to cavity quantum electrodynamics it is the REs that have been used historically.

An important remark is that it is possible, under certain conditions, to recast the Maxwell-Bloch equations into an equivalent set of REs. In semiconductors the rate of dephasing of the medium polarisation is typically many orders faster than the other dynamical variables and as such can be adiabatically eliminated, thus reducing the system dimension to that of the REs [23]. However, a crucial difference is that the reduced Maxwell-Bloch equations ignore the *quantum fluctuations* associated with spontaneous emission.

In the limit of small lasers, where the spontaneous emission factor approaches unity, $\beta \to 1$, the REs have found usefulness thanks to their simplicity, and their intrinsic ability to describe the incoherent *and* coherent portions of the radiation within the cavity. They can be considered the simplest mathematically, but are nevertheless very powerful. However, they cannot tell us where the location of the laser threshold is. It could be argued that this is not entirely true as in the macroscopic case its location can be discerned from the almost discontinuous jump between the upper and lower branches of the response curve. In want of other markers, this technique is typically used experimentally, however, laser threshold has more than one signifier as we have discussed and using the inflection point of the response curve is not always possible, e.g. where $\beta \to 1$ and in this case RE that include Langevin forces have been shown to account for the transition to lasing via $g^{(2)}(0)$ [1].

Below, we introduce the approach of a master equation from a quantum Hamiltonian before giving a simple analysis of a set of rate equations containing noise enabling them to access the photon statistics.

2.3.1 Master equation approach

In order to describe the dynamics of the two-level cavity system we can use a Master equation. This comprises of a density matrix describing the evolution of the two-level

system and the Jaynes-Cummings Hamiltonian that describes the interaction between said system and one resonant cavity mode. This describes the dynamics of a reversible process which is given by the von Neumann equation

$$\frac{\partial}{\partial t}\rho = -\frac{i}{\hbar}[H_{JC}, \rho], \tag{2.6}$$

where $\rho(t)$ is the density matrix and H_{JC} is the Jayens-Cummings Hamiltonian. For the device to work as a laser it must have a channel from which photons from the cavity can escape. To capture the losses the cavity system is coupled with the environment. This is achieved by the inclusion of the Lindblad terms which act as the coupling to the environment within the Markov approximation. The Markov approximation states that the environment relaxes back to its thermodynamical equilibrium and provides a response to the system before any other event takes place. So the decays depend only on the density matrix of system at time t. The coupling of the system with the environment can be seen schematically in Figure .(2.2). The master equation is thus in the general Lindblad form given by

$$\frac{\partial}{\partial t}\rho(t) = \frac{i}{\hbar}[H_{JC}, \rho(t)] - \mathcal{L}_p\rho(t) - \mathcal{L}_\gamma\rho(t) - \mathcal{L}_\kappa\rho(t). \tag{2.7}$$

The Lindblad operators in Eq. (2.7) are

$$\mathcal{L}_\kappa\rho = \frac{\kappa}{2}(a^\dagger a\rho(t) + \rho(t)a^\dagger a - 2a\rho(t)a^\dagger), \tag{2.8}$$

which describes the cavity decay, and

$$\mathcal{L}_x\rho = \sum_{i=1}^{N}\frac{x_i}{2}(\Gamma_x^{(i)\dagger}\Gamma_x^{(i)}\rho(t) + \rho(t)\Gamma_x^{(i)\dagger}\Gamma_x^{(i)} - 2\Gamma_x^{(i)}\rho(t)\Gamma_x^{(i)\dagger}), \tag{2.9}$$

where together $\mathcal{L}_p\rho(t)$ and $\Gamma_p^{(i)} = \sigma_i^\dagger$ describe the pumping mechanism from the ground to excited state. Emission into non-lasing modes is represented together by $\mathcal{L}_\gamma\rho(t)$ and $\Gamma_\gamma^{(i)} = \sigma_i$.

From the master equation it is possible to derive simple rate equations which can

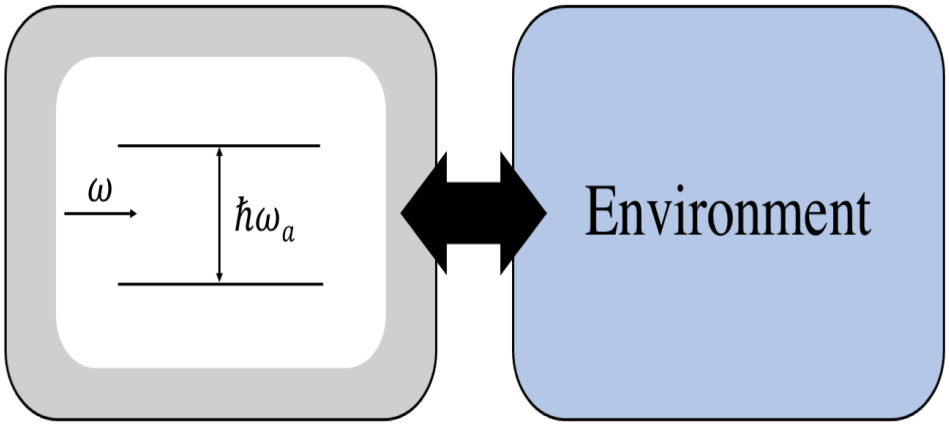

Figure 2.2: The two-level system on the left is coupled to the environment shown as a reservoir on the right.

be generalised to N-emitters. Using Eq. 2.7, it can be shown that the expectation value evolution of an operator is

$$\frac{d}{dt}\langle A\rangle = \frac{1}{i\hbar}\langle[A, H_{JC}]\rangle + \frac{\kappa}{2}\langle[a^\dagger, A]a + a^\dagger[A, a]\rangle + \sum_{x\epsilon P,\gamma}\sum_{i}^{N}\frac{x^{(i)}}{2}\langle[\Gamma_x^{(i)\dagger}, A]\Gamma_x^{(i)} + \Gamma_x^{(i)\dagger}[A, \Gamma_x^{(i)}]\rangle \tag{2.10}$$

where $a^\dagger$ (a) creates (destroys) a photon in the cavity mode, $\sigma_i^\dagger$ (σ_i) raises (lowers) an electron in the i'th emitter and $\Gamma_x^{(i)} = \sigma_i$. Using Eq. 6 we can write equations for the average photon number $\langle a^\dagger a\rangle$, inversion $\langle\sigma_i^\dagger\sigma_i\rangle$ and photon assisted polarisation $\langle\sigma_i a^\dagger\rangle$

$$\frac{d}{dt}\langle a^\dagger a\rangle = \sum_{i}^{N} 2g_i \mathrm{Im}[\langle\sigma_i a^\dagger\rangle] - \kappa\langle a^\dagger a\rangle, \tag{2.11}$$

$$\frac{d}{dt}\langle\sigma_i^\dagger\sigma_i\rangle = P_i\langle\sigma_i\sigma_i^\dagger\rangle - 2g_i \mathrm{Im}[\langle\sigma_i a^\dagger\rangle] - \gamma_i\langle\sigma_i^\dagger\sigma_i\rangle, \tag{2.12}$$

$$\left(\frac{d}{dt}+\frac{1}{2}(P_i+\gamma_i+\kappa_i)\right)\langle\sigma_i a^\dagger\rangle = ig_i(\langle\sigma_i^\dagger\sigma_i a a^\dagger\rangle - \langle\sigma_i\sigma_i^\dagger a^\dagger a\rangle). \tag{2.13}$$

Where κ is the cavity decay rate, γ is the decay rate into non-lasing modes, and P is the pumping rate. g_i is the light-matter coupling between the i'th emitter and the cavity mode, and can be measured experimentally by fitting experimental data to the model. It From here we note that if the polarisation of the material decays on a timescale that is much faster than the other dynamic variables then we can adiabatically eliminate the polarisation, i.e. set its time derivative to zero, $\frac{d\langle\sigma_i a^\dagger\rangle}{dt}=0$. At this point once Eq. (2.13) is rearranged the equation for the polarisation is substituted into the equations for the photon number and inversion. Thus, we are left with two rate equations able to describe the systems dynamics that agree very well with the results of the master equation [19].

2.3.2 Rate equation analyses

As shown in the previous section we can derive a set of RE from a completely quantum approach, under approximations, using a master equation which involves coupling our cavity system with the environment. Although powerful, on their own RE lack the ability to describe photon statistics; in order to describe lasing and the laser threshold it is neccessary to have access to the photon statistics like $g^{(2)}(0)$. However, by including Langevin noise terms [1,32] the important statistical information about the system can be recovered. The model outlined in [1] does not consider QDs, but rather two-level emitters. In the rest of this section I shall refer to general emitters, but note that this model can be applied to discrete two-level QDs.

As mentioned before there is a potential technological use for nanolasers in telecommunications, therefore, much time and effort is spent on understanding the properties and limitations of these devices. It is important that the question of weather we are gaining or losing performance by reducing device size is answered as the viability of these devices could be impacted. If reducing size comes at a cost of increasing the noise of these devices then this would make them impractical for use in telecommunications.

The rate equations for the photon number, n_p, and the inversion, n_e, are

$$\frac{dn_e}{dt} = \gamma_p(n_o - n_e) - \gamma_r(2n_e - n_o)n_p - \gamma_t n_e + F_e, \tag{2.14}$$

$$\frac{dn_p}{dt} = \gamma_r(2n_e - n_o)n_p + \gamma_r n_e - \gamma_c n_p + F_p, \tag{2.15}$$

where γ_c is the decay rate of the cavity mode, γ_r is the light-matter coupling strength, and γ_p is the pumping rate. The total decay rate is $\gamma_t = \gamma_r + \gamma_{bg}$, where γ_{bg} is the decay into background, or non-lasing modes. The first term on the RHS of Eq. (2.14) is the pump rate into the upper laser level and the second and third terms give the rates of stimulated and spontaneous emission, respectively. The third term on the RHS of Eq. (2.15) is the decay rate of photons out of the cavity mode and F_e and F_p are the stochastic Langevin forces [32]. To understand the role of the Langevin terms consider the average value $\langle F(t)\rangle = 0$, i.e., it takes on negative and positive values just as often and thus the time average is 0 - this is also true of the statistical average. The term $\langle F(t)F(t-\tau)\rangle = 0$. $\langle F(t)\rangle$ can be likened to a random number generator and is characterised as a memoryless proccess resulting in no correlation relative to an earlier values, e.g., $\langle F(t-\tau)\rangle$. Since $F(t)$ and $F(t-\tau)$ fluctuate randomly with respect to one another this also leads to the following result $\langle F(t)F(t-\tau)\rangle = 0$. The Langevin terms above correspond to the inherent random fluctuations in the lasers physical processes and are key to understanding intensity noise of the laser as well as linewidth. With the added noise terms it is possible to explore statistical information about these devices such as the RIN, Fano factor and the intensity correlation, $g^{(2)}(0)$, all of which give valuable information about the performance of the device. In particular $g^{(2)}(0)$ is useful quantity in this new regime where thresholdless lasing occurs.

By solving equations Eq. (2.14) and Eq. (2.15) either analytically or by integrating, the steady state values of the photon number and the inversion are found. From here we can plot the photon number as a function of the pump rate for different values of the spontaneous emission factor, β. This allows for a comparison of standard lasers with nanolasers. When $\beta = 1$, as is the case for nanolasers, there is only one mode available for the photons couple to - the lasing mode. This is a result of the low modal

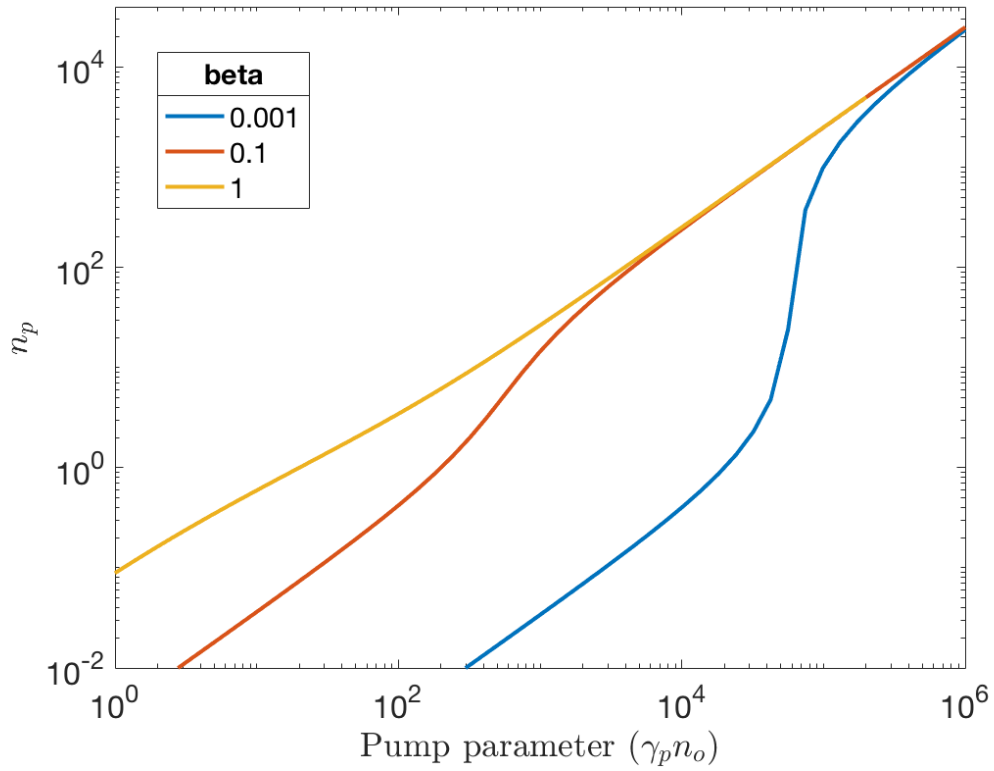

Figure 2.3: Number of emitters: 20 (yellow), 200 (red) and 20000 (blue). The pump rate has been scaled with the number of emitters in order to compare the curves better. This figure was produced by recalculating the top panel of Fig. 3 in [1].

volume restricting other cavity modes. From Fig. 2.3 we can see that for $\beta = 1$ the input-output curve approaches that of a straight line. When comparing the yellow curve with the other curves it is clear there is no distinct threshold which comes in the form of a kink in the curve. This is the route of term thresholdless lasing. A lot of debate has surrounded the community in how we classify such lasers as one of the long standing criteria for a laser was the existence of a threshold.

When the spontaneous emission factor is small, as it would be for a typical macroscopic laser, there is a pronounced s-shaped curve. Comparing the transition curves best illustrates this point. For 200 emitters (red), there is smooth trajectory as a function of the pump which contrasts with that of the curve corresponding to the 20000 emitter (blue) device. The blue curve shows a pronounced s-shape with a large jump in

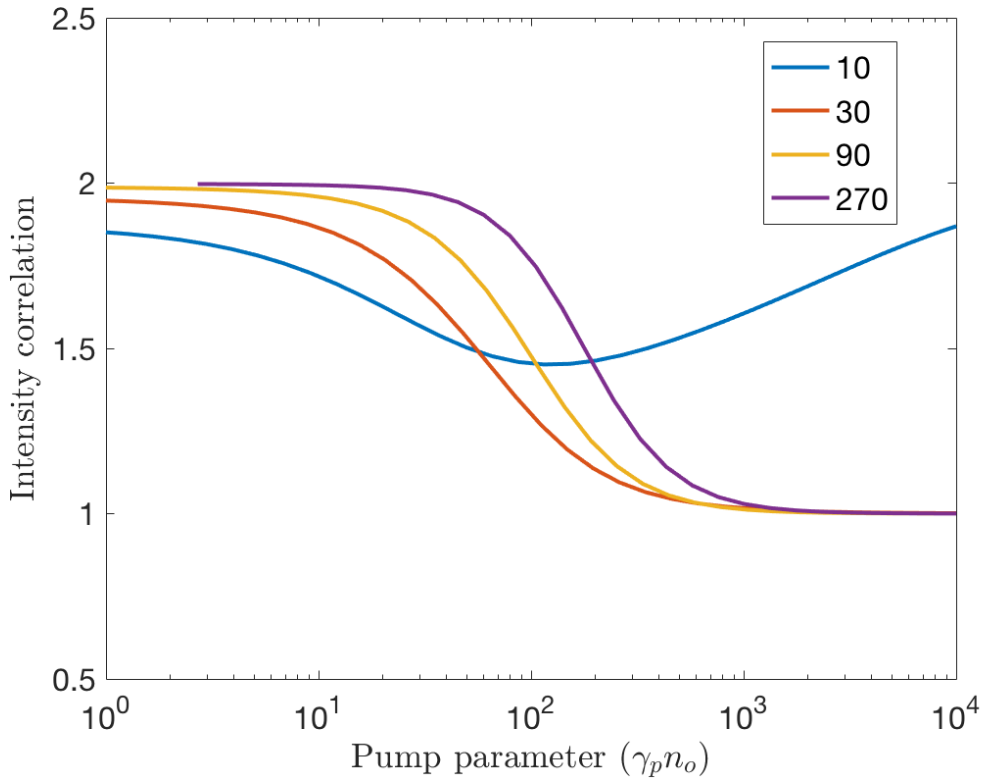

Figure 2.4: Four different devices with different number of emitters. The yellow, red and purple curves show devices that make a laser transition. The blue curve shows how too few emitters means lasing cannot occur. This figure was produced by recalculating Fig. 5a in [1].

the output over a very short pump rate. The abrupt transition is almost a discontinuous jump and behaves effectively as a switch in this phase transition.

The new feature of thresholdless lasing means we must extend our analyses of the laser dynamics due to the uncertainty in the the laser threshold in the input-output curves. In order to do this we look at the intensity correlation function, $g^{(2)}(0)$, which can give us important information on the photon statistics of the system. This statistical information is obtained through the inclusion of the Langevin forces in Eqs., i.e., F_e and F_p. If $g^{(2)}(0) > 1$ then this would correspond to photons bunching together, i.e. thermal light. For the light to be considered chaotic the intensity autocorrelation function must take values closer to $g^{(2)}(0) \approx 2$. This is a manifestation of their Bosonic nature and in this case the light displays super-Poissonian statistics. If $g^{(2)}(0) = 1$

the emission would be purely coherent corresponding to a laser and when $g^{(2)}(0) < 0$ this means the photon statistics are sub-Poissonian resulting in photon anti-bunching, a purely quantum phenomenon with no classical counterpart. Figure 2.4 shows the intensity correlation as a function of the pump rate for four different devices which have different numbers of emitters. The blue curve is of particular interest as it has a clear dip but never actually reaches a value of one. This is significant as it tells us this device which only has 10 emitters does not emit coherent light and this result has also been observed experimentally [15]. Therefore, the simple rate equations are powerful as they are able to predict and reproduce behaviours of nanolasers. To understand this result better we can see how adding emitters to the cavity affects the interaction with the field. The light-matter coupling scales as $\gamma_r = \gamma_r\sqrt{N}$. Therefore, it is clear that by increasing the amount of emitters the interaction with the field is stronger. The other curves in Fig 2.4 highlight this point by showing that increasing the number of emitters means the device is capable of lasing as $g^{(2)}(0) = 1$.

The relative intensity noise (RIN) is given by

$$RIN = \frac{\langle \Delta n_p^2 \rangle}{\langle n_p \rangle^2}, \tag{2.16}$$

where $\langle \Delta n_p^2 \rangle$ is the variance of the photon number, and $\langle n_p \rangle$ is the expectation value of the photon number. The RIN can help us understand the quantum noise properties of the devices under consideration. As stated before, the noise amplitude is important if nanolasers are to be used in telecommunications. Figure 2.5 shows the RIN as a function of the pump for the same four devices considered in Fig 2.4. As the pump rate increases the RIN for all four devices decreases. This trend continues for the 30, 90 and 270 emitter devices, however, when there are only 10 emitters the RIN levels out and stops decreasing. Thus, devices with fewer emitters have greater RIN compared to those devices which have greater numbers of emitters and increasing the pump rate further does not change the RIN. Inspecting Figs 2.4 and 2.5 reveals to us the region of the pump where the lasing transitions begin for the three lasing devices; this region is also where the RIN curve of the non-lasing device diverges from the other curves. This

behaviour illustrates that the noise amplitude is significantly reduced for the lasing devices compared with the non-lasing device which is in agreement with the $g^{(2)}(0)$ approaching 1. Again, the RE with added Langevin forces continue to be a valuable tool in analysing statistical information that sheds light on the noise and emission properties of nanolasers.

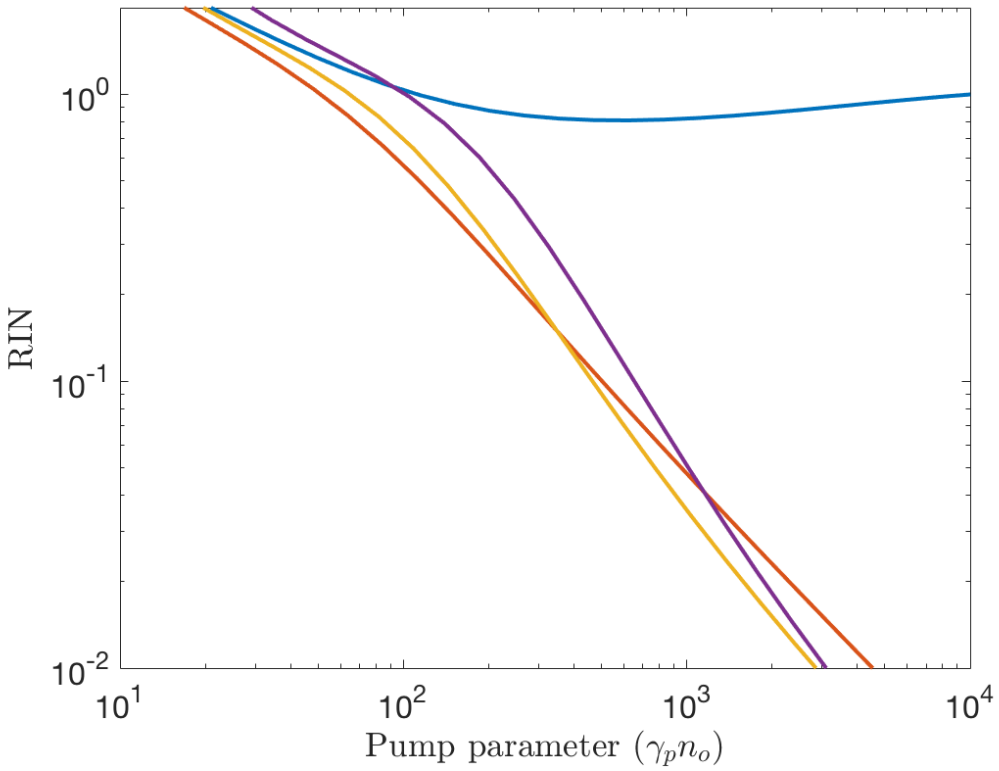

Figure 2.5: RIN for the same four devices with different emitter numbers. The RIN for the 10 emitter device diverges from the other lasing devices who RIN continue to decrease as the pump is increased. This figure was produced by recalculating Fig. 5b in [1].

2.4 Conclusion

Nanolasers have potential future applications as useful devices if they are integrated with current technology. Reduced size along with low power consumption and footprint are just some of the advantages they offer. RE employed to model small lasers can

be derived from a quantum master equation and display results in line with more rigorous and sophisticated approaches. The phenomenon of thresholdless lasing has been discussed and understood in terms of the small modal volumes and spontaneous emission factors close to unity. It has also been shown that the inclusion of Langevin forces in RE gives statistical information of the system and this can be directly applied to look at the $g^{(2)}(0)$ and the RIN. For devices which have few emitters, we have seen that lasing is not possible and only by including more emitters in the cavity can lasing be achieved. These are just some of the important properties investigated and the knowledge gained will lead to a better understanding of nanolasers for future study. The models considered in this chapter lack coherent variables like the coherent field and standard polarization. This means that for the RE, we have to extend them to include Langevin forces to increase their reach into photon statistics, shedding more light on the onset of lasing. However, the limitations of these models become apparent when attempting to identify the crucial transition point— the emergence of a nonzero coherent field amplitude signifying lasing threshold. In the following chapter, we'll explore a novel approach that directly integrates these previously neglected coherent variables. By doing so, we not only bridge the gap between incoherent and coherent emission regimes but also gain the capability to pinpoint the exact moment when lasing begins. This shift in perspective will illuminate the entirety of the lasing process, from the incoherent pre-threshold state to the coherent emission regime above laser threshold.

Chapter 3

Model derivation

3.1 Incoherent and coherent variables

Semiconductor quantum models for QD nanolasers that are capable of describing the photon number above and below laser threshold have been developed in recent years [31]. They are in stark contrast to the classical Maxwell-Bloch equations which only describe emission above laser threshold. Although these new quantum models describe the photon number across both incoherent and coherent emission regimes, they are not able to directly identify the onset of lasing, i.e., when a nonzero coherent field emerges. In order to resolve this problem, extensions to the models are made which see higher-order correlations introduced allowing for access to the photon statistics. With the photon statistics it is possible to describe the type of emission and hence observe the transition from incoherent to coherent emission. The discussion so far illustrates that there is a need to track the evolution of the coherent processes explicitly via their expectation values. At the level of the Maxwell-Bloch equations the equivalent coherent variables are the coherent field amplitude and the medium polarisation amplitude.

The coherent variables are implicit in the previous models (see Section 3.3 on how to extract them through the cluster expansion) and as such they cannot directly observe the lasing threshold which corresponds to the emergence of a nonzero coherent field amplitude. The models derived within this chapter differ with respect to previous models in that they consider the coherent and incoherent variables separetley [5,15,31].

3.2 The structure of the system Hamiltonian

The photon operators of the system Hamiltonian obey the Bosonic commutation relations

$$[b_i, b_j]_- = 0 = [b_i^\dagger, b_j^\dagger]_- \tag{3.1}$$

$$[b_i, b_j^\dagger]_- = \delta_{ij} \tag{3.2}$$

and the carrier operators obey the Fermi anti-commutation relations

$$[c_i, c_j]_+ = 0 = [c_i^\dagger, c_j^\dagger]_+ \tag{3.3}$$

$$[c_i^\dagger, c_j]_+ = \delta_{ij}. \tag{3.4}$$

where δ_{ij} is the Kronecker delta. The Bosonic operators b and $b^\dagger$ correspond to single-particle operators and it can be shown that N Bosonic operators are formally equivalent to $2N$ Femi operators under the specific requirements that the compound Fermi operator is symmetrical with respect to creation and annihilation operators [33], i.e., they contain equal numbers of creation and annihilation operators. This is true also for Fermionic operators which are mixed as in the case of the standard polarisation $v^\dagger c$. Therefore, we refer to the coherent filed operator b, carrier number $c^\dagger c$, and standard polarisation $v^\dagger c$ as single particle operators; and, the photon number operator $b^\dagger b$ and photon assisted polarisation $bc^\dagger v$ correspond to two particle operators.

The structure of the system Hamiltonian takes the form

$$H = H_{free} + H_{int} \tag{3.5}$$

where H_{free} corresponds to the non-interacting part and H_{int} to the interacting part of the Hamiltonian. The non-interacting part of the Hamiltonian is itself made up of contributions from the free electromagnetic field H_E and free electrons in the quantum

dot H_{QD}

$$H_{free} = H_E + H_{QD}. \tag{3.6}$$

The free photon energy part of the second quantized Hamiltonian is given by

$$H_{\mathrm{E}} = \hbar \sum_q \nu_q \Big(b_q^\dagger b_q + \frac{1}{2} \Big) \tag{3.7}$$

where ν_q is the frequency of a photon in the q-th mode and the quantum mechanical operators $b_q, b_q^\dagger$ annihilate and create a photon in the q-th mode, respectively. The sum over q takes into account lasing and non-lasing modes.

The free electron part of the Hamiltonian describes charge carries in the conduction and valence band states with respective energies $\epsilon_{c,n}$ and $\epsilon_{v,n}$ in the n-th quantum dot

$$H_{QD} = \sum_n \Big(\varepsilon_{c,n} c_n^\dagger c_n + \varepsilon_{v,n} v_n^\dagger v_n \Big) \tag{3.8}$$

where $c_n, c_n^\dagger$ and $v_n, v_n^\dagger$ are the annihilation and creation operators, respectively, for conduction and valence electrons of the n-th quantum dot.

The full two-particle light-matter interaction is described by

$$H_{int} = -i\hbar \sum_{n,q} \Big[g_{nq} \Big(b_q c_n^\dagger v_n + b_q v_n^\dagger c_n \Big) - g_{nq}^* \Big(b_q^\dagger v_n^\dagger c_n + b_q^\dagger c_n^\dagger v_n \Big) \Big] \tag{3.9}$$

with g_{nq} corresponding to the light-matter coupling strength between a photon in the q-th mode and the n-th quantum dot. The total system Hamiltonian is thus

$$\begin{aligned} H = \hbar \sum_q \nu_q \Big(b_q^\dagger b_q + \frac{1}{2} \Big) + \sum_n \Big(\varepsilon_{c,n} c_n^\dagger c_n + \varepsilon_{v,n} v_n^\dagger v_n \Big) \\ -i\hbar \sum_{n,q} \Big[g_{nq} \Big(b_q c_n^\dagger v_n + b_q v_n^\dagger c_n \Big) - g_{nq}^* \Big(b_q^\dagger v_n^\dagger c_n + b_q^\dagger c_n^\dagger v_n \Big) \Big]. \end{aligned} \tag{3.10}$$

It should be noted that this is a simplified system Hamiltonian for a semiconductor as in reality the Hamiltonian should also contain contributions from phonon and Coulomb interactions between charge carriers. However, at sufficiently low temperatures $\approx$ 4K these interactions are weak enough such that they may be neglected [5].

One final remark on the structure of the system Hamiltonian concerns the two-particle operators coming from the interaction part of the Hamiltonian: $b_q^\dagger c_n^\dagger v_n$ and $b_q v_n^\dagger c_n$. Quantum mechanically, operators of the former kind describe a process where a photon in mode q is created in conjunction with an electron being destroyed in the valance band and subsequently created in the conduction band of the n-th quantum dot. The reverse process is true of the latter operator term. Processes of this kind do not conserve energy thus we eliminate them from the interaction Hamiltonian. The elimination of these terms is know as the rotating wave approximation (RWA). Therefore, the final form of the system Hamiltonian is

$$H = \hbar \sum_q \nu_q \Big(b_q^\dagger b_q + \frac{1}{2} \Big) + \sum_{n,q} \Big[\Big(\varepsilon_{c,n} c_n^\dagger c_n + \varepsilon_{v,n} v_n^\dagger v_n \Big) - i\hbar \Big(g_{nq} b_q c_n^\dagger v_n - g_{nq}^* b_q^\dagger v_n^\dagger c_n \Big) \Big]. \tag{3.11}$$

3.3 The Cluster expansion

The intrinsic nature of light-matter interaction and it is structure within the system Hamiltonian leads to an infinite hierarchical coupling to higher order terms which is a characteristic problem of many-body interactions. This coupling to higher order terms dictates that the quantum dynamics follow from

$$i\hbar \frac{d}{dt} \langle \hat{N} \rangle = E[\langle \hat{N} \rangle] + P[\langle \hat{N} + 1 \rangle] \tag{3.12}$$

where the functionals E and P describe coupling to terms of the same and higher order, respectively [33]. Therefore, we must find a way to systematically truncate the infinite system of ordinary differential equations. This is achieved through expressing the dynamics in terms of correlation functions which are obtained through the cluster expansion.

3.3.1 Pure Bosonic operators

An expectation value $\langle ... \rangle$ can be expressed in terms of all possible combinations of lower operator products. For example, the expectation value of a four-particle operator takes the form $\langle \hat{O}\hat{O}\hat{O}\hat{O} \rangle$ and can be expanded in the following way[1][2]

$$\langle \hat{O}\hat{O}\hat{O}\hat{O} \rangle = \delta\langle \hat{O}\hat{O}\hat{O}\hat{O} \rangle + \langle \hat{O} \rangle \delta\langle \hat{O}\hat{O}\hat{O} \rangle + \langle \hat{O} \rangle \langle \hat{O} \rangle \delta\langle \hat{O}\hat{O} \rangle + \delta\langle \hat{O}\hat{O} \rangle \delta\langle \hat{O}\hat{O} \rangle + \langle \hat{O} \rangle \langle \hat{O} \rangle \langle \hat{O} \rangle \langle \hat{O} \rangle \tag{3.13}$$

where Eq.(3.13) contains the purely correlated part, singlet-triplet, singlet-doublet, doublet-doublet and singlet contributions, respectively. These cover all possible factorisations for a four-particle expectation value which is the lowest order needed to investigate the photon statistics. Implicit in this notation, however, is the fact that one must consider all possible realisations of the operator positions; for *bosons* this is not too cumbersome, but this is not true of *fermions* when there are more than two, i.e. in the case of pure carrier expectation values. The easiest and cleanest way to implement the cluster expansion is to first prepare all strings of operator products into normal order where all creation operators on the left and all annihilation operators on the right of the expectation value. Once this is done label the operators as such $\langle \hat{O}_1\hat{O}_2\hat{O}_3\hat{O}_4 \rangle$ in order to keep track of each one throughout the expansion. Another important point to note is that when expressing the different 'clusters' keep the order of the numbers, e.g. $\delta\langle \hat{O}_1\hat{O}_3 \rangle \delta\langle \hat{O}_2\hat{O}_4 \rangle$. $g^{(2)}(0)$ is obtained through the intensity correlation $\delta\langle b^\dagger b^\dagger bb \rangle$

$$g^{(2)}(0) = 2 + \frac{\delta\langle b^\dagger b^\dagger bb \rangle}{\langle b^\dagger b \rangle}^2 , \tag{3.14}$$

[1] Here the δ is dropped in front of single-particle expectation values as there is no distinction between itself and the correlated part

[2] $\hat{O}$ represents any single-particle operator either bosonic or fermionic

where $\langle b^\dagger b\rangle$ is the expectation value of the photon number [5, 31]. The full cluster expansion of the intensity correlation is

$$\langle b_1^\dagger b_2^\dagger b_3 b_4\rangle = \delta\langle b_1^\dagger b_2^\dagger b_3 b_4\rangle + \langle b_1^\dagger\rangle\delta\langle b_2^\dagger b_3 b_4\rangle + \langle b_2^\dagger\rangle\delta\langle b_1^\dagger b_3 b_4\rangle + \langle b_3\rangle\delta\langle b_1^\dagger b_2^\dagger b_4\rangle + \langle b_4\rangle\delta\langle b_1^\dagger b_2^\dagger b_3\rangle \tag{3.15}$$
$$+\langle b_1^\dagger\rangle\langle b_2^\dagger\rangle\delta\langle b_3 b_4\rangle + \langle b_1^\dagger\rangle\langle b_3\rangle\delta\langle b_2^\dagger b_4\rangle + \langle b_1^\dagger\rangle\langle b_4\rangle\delta\langle b_2^\dagger b_3\rangle + \langle b_2^\dagger\rangle\langle b_3\rangle\delta\langle b_1^\dagger b_4\rangle$$
$$+\langle b_2^\dagger\rangle\langle b_4\rangle\delta\langle b_1^\dagger b_3\rangle + \langle b_3\rangle\langle b_4\rangle\delta\langle b_1^\dagger b_2^\dagger\rangle + \delta\langle b_1^\dagger b_2^\dagger\rangle\delta\langle b_3 b_4\rangle + \delta\langle b_1^\dagger b_3\rangle\delta\langle b_2^\dagger b_4\rangle$$
$$+\delta\langle b_1^\dagger b_4\rangle\delta\langle b_2^\dagger b_3\rangle + \langle b_1^\dagger\rangle\langle b_2^\dagger\rangle\langle b_3\rangle\langle b_4\rangle.$$

The extra terms arise from all the possible permutations of the operators. Dropping the subscripts we get

$$\langle b^\dagger b^\dagger b b\rangle = \delta\langle b^\dagger b^\dagger b b\rangle + 2\langle b^\dagger\rangle\delta\langle b^\dagger b b\rangle + 2\langle b\rangle\delta\langle b^\dagger b^\dagger b\rangle + \langle b^\dagger\rangle\langle b^\dagger\rangle\delta\langle b b\rangle \tag{3.16}$$
$$+ 4\langle b^\dagger\rangle\langle b\rangle\delta\langle b^\dagger b\rangle + \langle b\rangle\langle b\rangle\delta\langle b^\dagger b^\dagger\rangle + \delta\langle b^\dagger b^\dagger\rangle\delta\langle b b\rangle + 2\delta\langle b^\dagger b\rangle\delta\langle b^\dagger b\rangle + \langle b^\dagger\rangle\langle b^\dagger\rangle\langle b\rangle\langle b\rangle.$$

3.3.2 Pure carrier expectation values

In the case of expectation values which consist solely of fermionic operators it is not enough to simply group them into two's and carry out the expansion as if they were bosons; we must also take care to deal with the possible permutations between creation and destruction operators. Using the same notation from the book of Kira and Koch [33] we can write the cluster expansion of a two-particle fermionic expectation value as

$$\langle k^\dagger p^\dagger l m\rangle = \langle k^\dagger p^\dagger l m\rangle_{singlets} + \delta\langle k^\dagger p^\dagger l m\rangle \tag{3.17}$$

The difference lies in the treatment of the singlet part; if this were purely bosonic we could easily factorise it into two singlet expectation values, e.g.

$$\langle b^\dagger b\rangle = \delta\langle b^\dagger b\rangle + \langle b^\dagger\rangle\langle b\rangle, \tag{3.18}$$

but for fermions we need to cycle through all possible combinations of destruction and creation operators too. Thus

$$\langle k^\dagger p^\dagger lm\rangle_{singlets} = \langle k^\dagger m\rangle\langle p^\dagger l\rangle - \langle k^\dagger l\rangle\langle p^\dagger m\rangle \tag{3.19}$$

where the minus sign is due to the fact that we have swapped the operators which obey anti-commutation relations. Inserting equation Eq. (3.19) into equation Eq. (3.17) gives

$$\langle k^\dagger p^\dagger lm\rangle = \langle k^\dagger m\rangle\langle p^\dagger l\rangle - \langle k^\dagger l\rangle\langle p^\dagger m\rangle + \delta\langle k^\dagger p^\dagger lm\rangle \tag{3.20}$$

3.3.3 Example of a mixed expectation value with more than two fermionic operators

The expansion of an operator like $\langle b^\dagger c^\dagger v^\dagger vc\rangle$ does not require any more rules than have already been discussed. This is a three-particle expectation which means we need to consider the extra ways we can group the operators. Symbolically we have

$$\langle \hat{O}\hat{O}\hat{O}\rangle = \delta\langle \hat{O}\hat{O}\hat{O}\rangle + \langle \hat{O}\rangle\delta\langle \hat{O}\hat{O}\rangle + \langle \hat{O}\rangle\langle \hat{O}\rangle\langle \hat{O}\rangle. \tag{3.21}$$

The purely correlated part is trivial and there is no need for any factorisation. As the bosonic operators commute with the fermionic operators, to deal with the singlet part we have to factor out the bosonic operator and apply the same methods as were used in Eq. (3.19) which results in

$$\langle b^\dagger c^\dagger v^\dagger vc\rangle_{singlets} = \langle b^\dagger\rangle\langle c^\dagger c\rangle\langle v^\dagger v\rangle - \langle b^\dagger\rangle\langle c^\dagger v\rangle\langle v^\dagger c\rangle. \tag{3.22}$$

At this point, we have the purely correlated part and the singlet contributions which leaves the singlet-doublet correlations to construct. If we notice that right hand side of equation Eq. (3.22) contains all possible single-particle expectation values we can combine these to construct the singlet-doublet terms. For example, $\langle b^\dagger\rangle\langle c^\dagger c\rangle\langle v^\dagger v\rangle$ is

made up of three distinct terms which we can use to build $\langle\hat{O}\rangle\delta\langle\hat{O}\hat{O}\rangle$:

$$\langle b^\dagger\rangle\delta\langle c^\dagger v^\dagger vc\rangle, \tag{3.23}$$

$$\langle c^\dagger c\rangle\delta\langle b^\dagger v^\dagger v\rangle, \tag{3.24}$$

$$\langle v^\dagger v\rangle\delta\langle b^\dagger c^\dagger c\rangle. \tag{3.25}$$

These terms will have positive sign because they come from the positive part of the singlet factorisation, whereas the term $\langle b^\dagger\rangle\langle c^\dagger v\rangle\langle v^\dagger c\rangle$ has a minus sign in front therefore the terms it contributes will also have a minus sign. Putting all this together we get

$$\begin{aligned}\langle b^\dagger c^\dagger v^\dagger vc\rangle = \delta\langle b^\dagger c^\dagger v^\dagger vc\rangle + \langle b^\dagger\rangle\langle c^\dagger c\rangle\langle v^\dagger v\rangle - \langle b^\dagger\rangle\langle c^\dagger v\rangle\langle v^\dagger c\rangle + \langle b^\dagger\rangle\delta\langle c^\dagger v^\dagger vc\rangle \\ + \langle c^\dagger c\rangle\delta\langle b^\dagger v^\dagger v\rangle + \langle v^\dagger v\rangle\delta\langle b^\dagger c^\dagger c\rangle - \langle c^\dagger v\rangle\delta\langle b^\dagger v^\dagger c\rangle - \langle v^\dagger c\rangle\delta\langle b^\dagger c^\dagger v\rangle.\end{aligned} \tag{3.26}$$

3.4 The Heisenberg Equation

Now that the system Hamiltonian is known and we have a systematic truncation scheme in place we can calculate the equations that govern the quantum dynamics using the Heisenberg equation of motion

$$i\hbar\frac{d}{dt}\hat{O} = \left[\hat{O}, H\right]_- \tag{3.27}$$

where $\hat{O}$ corresponds to any system operator of interest. It is helpful to utilise the linear additivity property of the commutator in order to express the commutator in the Heisenberg equation as a linear superposition of the free and interacting parts of the system Hamiltonian

$$\left[\hat{A}, \sum_i B_i\right]_- = \sum_i \left[\hat{A}, B_i\right]_- \tag{3.28}$$

where the sum is over the interacting and non-interacting parts of the system Hamiltonian. Thus, giving

$$\left[\hat{O}, H\right]_- = \left[\hat{O}, H_E\right]_- + \left[\hat{O}, H_{QD}\right]_- + \left[\hat{O}, H_{int}\right]_-. \tag{3.29}$$

Using the fact that the Bosonic photon operators commute with the Fermi electron operators simplifies the computation of the commutators in Eq. (3.29). This leaves us with the easier task of evaluating the following commutators

$$\Big[b_q, H\Big]_- = \Big[b_q, H_E\Big]_- + \Big[b_q, H_{int}\Big]_- \tag{3.30}$$

$$\Big[c^\dagger v, H\Big]_- = \Big[c^\dagger v, H_{QD}\Big]_- + \Big[c^\dagger v, H_{int}\Big]_- \tag{3.31}$$

$$\Big[c^\dagger c, H\Big]_- = \Big[c^\dagger c, H_{QD}\Big]_- + \Big[c^\dagger c, H_{int}\Big]_- \tag{3.32}$$

The single particle operators form the basis of the quantum dynamics and all higher order operators are derived from them.

To derive the Heisenberg equations for the fundamental single-particle operators - b, $c^\dagger v$ and $c^\dagger c$ - we start by evaluating their commutators in Eqs.(3.30-3.32) utilising the Bosonic commutation and Fermionic anti-commutation relations. For b_q, we set $q = s$ where s is the index of the lasing mode

$$\Big[b_s, H_E\Big]_- = \hbar\nu_s b_s \tag{3.33}$$

for the non-interacting part and

$$\begin{aligned}\Big[b_s, H_{int}\Big]_- &= i\hbar \sum_{n,q} g^*_{nq} v^\dagger_n c_n \delta_{qs} \\ &= i\hbar \sum_n g^*_{ns} v^\dagger_n c_n\end{aligned} \tag{3.34}$$

for the interacting part of the system Hamiltonian. Substituting these results into the Heisenberg equation for b_s and dividing through by $i\hbar$ we get

$$\frac{d}{dt} b_s = -i\nu_s b_s + \sum_n g^*_{ns} v^\dagger_n c_n. \tag{3.35}$$

where b_s is now the field operator of a coherent laser field coupled to the standard polarisation operator. Eq.(3.35) clearly illustrates that the Heisenberg equation for the coherent field operator is driven by the polarisation of an ensemble of n quantum dots.

Applying the same methods the derivation of the Heisenberg equation for the standard polarisation and population operators follow in a similar fashion Thus, one obtains the full set of single-particle operator equations

$$\frac{d}{dt}b_s = -i\nu_s b_s + \sum_n g^*_{ns} v^\dagger_n c_n, \tag{3.36}$$

$$d_t v^\dagger_l c_l = -i\nu_{\varepsilon_l} v^\dagger_l c_l + \sum_q g_{ql}[2b_q c^\dagger_l c_l - b_q], \tag{3.37}$$

$$\frac{d}{dt}c^\dagger_l c_l = -2\Re \sum_q g_{ns} b_q c^\dagger_l v_l, \tag{3.38}$$

where $\nu_{\varepsilon_l} = \frac{\varepsilon_{c,l}}{\hbar}$ is the resonant frequency of the emitters. These equations are very important and useful as all higher-order Heisenberg equations can be constructed from them; all one has to do is apply the chain rule. This is faster and more efficient than calculating the commutator of a higher-order operator.

3.5 Heisenberg equations of two particle operators

The Heisenberg equations for all operator terms up to the two-particle level, excluding two-particle fermionic terms, are:

$$d_t b_s = -i\nu_s b_s + \sum_n g^*_{sn} v^\dagger_n c_n, \tag{3.39}$$

$$d_t v^\dagger_l c_l = -i\nu_{\varepsilon_l} v^\dagger_l c_l + \sum_q g_{ql}[2b_q c^\dagger_l c_l - b_q], \tag{3.40}$$

$$d_t c^\dagger_l c_l = -\sum_q [g_{ql} b_q c^\dagger_l v_l + g^*_{ql} b^\dagger_q v^\dagger_l c_l], \tag{3.41}$$

$$d_t b^\dagger_s b_s = \sum_n [g_{sn} b_s c^\dagger_n v_n + g^*_{sn} b^\dagger_s v^\dagger_n c_n], \tag{3.42}$$

$$d_t b_s c^\dagger_l v_l = -i\Delta\nu b_s c^\dagger_l v_l + g^*_l c^\dagger_l c_l - \sum_q g_{ql}[2b^\dagger_q b_s c^\dagger_l c_l - b^\dagger_q b_s] - \sum_{n\neq l} g^*_{sn} c^\dagger_l v^\dagger_n v_l c_n, \tag{3.43}$$

$$d_t b_s c^\dagger_l c_l = -i\nu_s b_s c^\dagger_l c_l - \sum_q [g_{ql} b_s b_q c^\dagger_l v_l + g^*_{ql} b^\dagger_q b_s v^\dagger_l c_l] - \sum_{n\neq l} g^*_{sn} v^\dagger_n c^\dagger_l c_n c_l, \tag{3.44}$$

$$d_t b_s b_s = -2i\nu_s b_s b_s + 2\sum_n g^*_{sn} b_s v^\dagger_n c_n, \tag{3.45}$$

$$d_t b_s v^\dagger_l c_l = -i(\nu_s + \nu_{\varepsilon_l}) b_s v^\dagger_l c_l + g_{sl}[2b_s b_s c^\dagger_l c_l - b_s b_s] - \sum_{n\neq l} g^*_{sn} v^\dagger_n v^\dagger_l c_n c_l, \tag{3.46}$$

where $\Delta\nu = \nu_{\varepsilon_l} - \nu_s$ is the detuning between the cavity mode photons and the emitters. We excluded the equations for two-particle fermionic operators, responsible for supperadiant effects, since we are focusing on regimes where the medium polarisation is large compared to the other decay rates of the system [34]. From these equations it is possible to arrive at two different types of models; one for expectation values and one for correlations.

It is important to bring attention to the operator terms $b_s b_s$ and $b_s v^\dagger_l c_l$ and their equations. In Section (3.2) it was made clear that the RWA resulted in the terms which do not conserve energy being neglected from the interaction part of the Hamiltonian. However, the same operator terms arise out of the system Hamiltonian Eq. (3.11) and as a result we do not neglect them.

3.5.1 Dissipation and pump

We include dissipation directly at the level of the Heisenberg equations via the Lindblad formalism. It is important to note that the order in which dissipation and pump is added is crucial if one is to preserve mathematical consistency between the correlation and expectation value models; only then can a simple change of variables allow for the transformation from one to the other.

3.6 Cluster Expansion Nonlinear QED Models - CNQED

In the following there are six systems of equations; three where the variables are in terms correlations and their equivalent in terms of expectation values (EVs). The correlation models are derived first from the Heisenberg equations which explicitly contains the conservative and dissipative parts. Only after the system is expressed solely in terms of correlations is the pump added phenomenologically. The only route to the expectation value models is through a change of variables where the cluster expansions in the tables (given below) are used. This is the only way to ensure the two models are equivalent and consistent mathematically.

3.6.1 Coherent-Incoherent Model

The algorithm to derive the model in terms of correlations is as follows:

1. Derive the Heisenberg equation for the variable of interest - if the variable is described by an operator greater than the single-particle operators then use the Eqs. (3.36-3.38) to construct it.

2. Take the expectation value of all operator terms.

3. Apply the cluster expansion and neglect the purely correlated part if bigger than a two particle correlation, e.g. terms like $\delta\langle\hat{O}\hat{O}\hat{O}\rangle$ are neglected.

The system variables of the first model we will consider come from the operators appearing explicitly in the system Hamiltonian and their singlet factorisation: $b, v^\dagger c, c^\dagger c, b^\dagger b$ and $bc^\dagger v$. Table 3.1 gives an overview of the EVs that appear at this level; their cluster

expansions are given in Table 3.2. Following the steps in the above algorithm leads to the corresponding Coherent-Incoherent model (CIM), named so on the account of the incoherent *and* coherent terms appearing explicitly,

$$d_t\langle c_l^\dagger c_l\rangle = r(1-\langle c_l^\dagger c_l\rangle) - (\gamma_{nl}+\gamma_{nr})\langle c_l^\dagger c_l\rangle - 2\mathfrak{Re}[g_l(\delta\langle bc_l^\dagger v_l\rangle) + \langle b\rangle\langle c_l^\dagger v_l\rangle], \tag{3.47}$$

$$d_t\delta\langle b^\dagger b\rangle = -2\gamma_c\langle b^\dagger b\rangle + 2\mathfrak{Re}\sum_n g_n(\delta\langle bc_n^\dagger v_n\rangle + \langle b\rangle\langle c_n^\dagger v_n\rangle), \tag{3.48}$$

$$\begin{aligned} d_t\delta\langle bc_l^\dagger v_l\rangle = &-(\gamma+\gamma_c+i\Delta\nu)\delta\langle bc_l^\dagger v_l\rangle + g_l^*[\langle c_l^\dagger c_l\rangle + \delta\langle b^\dagger b\rangle(2\langle c_l^\dagger c_l\rangle - 1) \\ &- |\langle v_l^\dagger c_l\rangle|^2], \end{aligned} \tag{3.49}$$

$$d_t\langle b\rangle = -(\gamma_c+i\nu)\langle b\rangle + \sum_n g_n^*\langle v_n^\dagger c_n\rangle, \tag{3.50}$$

$$d_t\langle v_l^\dagger c_l\rangle = -(\gamma+i\nu_{\varepsilon_l})\langle v_l^\dagger c_l\rangle + g_l[2\langle b\rangle\langle c_l^\dagger c_l\rangle - \langle b\rangle], \tag{3.51}$$

where γ_c is the cavity decay rate, γ_{nl} is the decay rate into non-lasing modes, γ_{nr} is the non-radiative decay rate, g is the light-matter coupling strength between the emitter and cavity mode, and r is the pump rate per emitter. The total pump rate is given by $\sum_N r$, where the sum is over the number of emitters. Figure 3.1 shows a system schematic with key parmeters from the model as well as important physical processes.

The cluster expansion is an efficient way to break the coupling to higher-order correlations, but it does introduce nonlinear terms which are absent for the equivalent EV based system. Fortunately, there is a way to revert back to the EV based model and restore the linearity of the system, however, as already discussed this must be done carefully in order to preserve mathematically consistency between the two models.

Table 3.3 gives the identities for the three-particle EVs truncated at the two-particle level. Using these identities we can transform the above correlation based model into

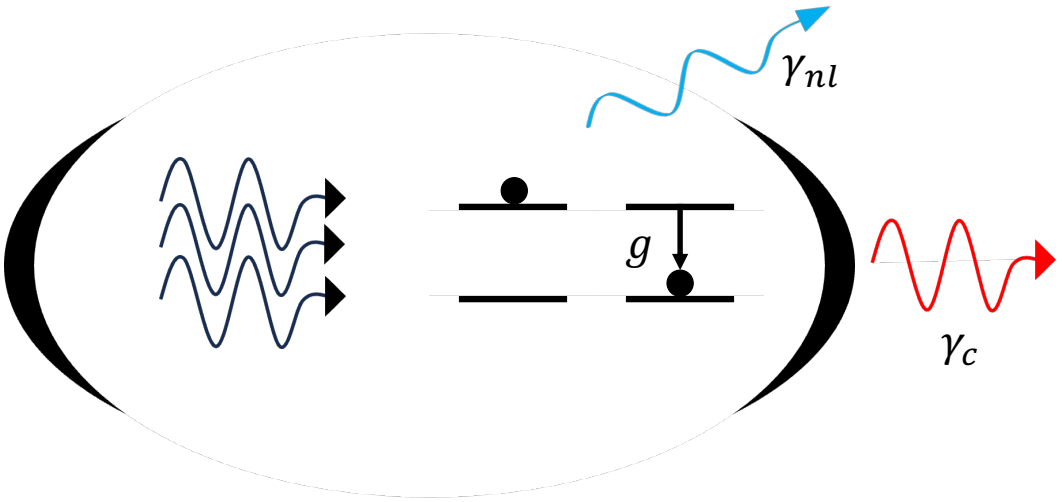

Figure 3.1: The two-level system on the left is coupled to the environment shown as a reservoir on the right.

the equivalent EV based model

$$d_t\langle c_l^\dagger c_l\rangle = r(1-\langle c_l^\dagger c_l\rangle) - (\gamma_{nl}+\gamma_{nr})\langle c_l^\dagger c_l\rangle - 2\mathfrak{Re}(g_l\langle bc_l^\dagger v_l\rangle), \tag{3.52}$$

$$d_t\langle b^\dagger b\rangle = -2\gamma_c\langle b^\dagger b\rangle + 2\mathfrak{Re}\sum_n g_n\langle bc_n^\dagger v_n\rangle, \tag{3.53}$$

$$\begin{aligned} d_t\langle bc_l^\dagger v_l\rangle = &-(\gamma+\gamma_c+i\Delta\nu)\langle bc_l^\dagger v_l\rangle + g_l^*[\langle c_l^\dagger c_l\rangle + \langle b^\dagger b\rangle(2\langle c_l^\dagger c_l\rangle - 1)] \\ &+ \langle c_l^\dagger v_l\rangle\sum_{n\neq l} g_n^*\langle v_n^\dagger c_n\rangle \end{aligned} \tag{3.54}$$

$$d_t\langle b\rangle = -(\gamma_c+i\nu)\langle b\rangle + \sum_n g_n^*\langle v_n^\dagger c_n\rangle, \tag{3.55}$$

$$d_t\langle v_l^\dagger c_l\rangle = -(\gamma+i\nu_{\varepsilon_l})\langle v_l^\dagger c_l\rangle + g_l[2\langle b\rangle\langle c_l^\dagger c_l\rangle - \langle b\rangle]. \tag{3.56}$$

Fig. 3.2 compares the correlation based model Eqs. (3.47-3.51) with the EV based model Eqs. (3.52-3.53) for different numbers of QDs. The parameter values used taken from [5] are normalised with respect to the nonradiative decay rate, $\gamma_{nr} = 10^9 s^{-1}$. The perfect overlap between both sets of curves clearly demonstrates the mathematical equivalence between the two models.

Particle order	Bosonic	Fermionic	Mixed
1	$\langle b \rangle$	$\langle c^\dagger c \rangle, \langle v^\dagger c \rangle$	N/A
2	$\langle b^\dagger b \rangle$	$\langle c_l^\dagger v_n^\dagger v_l c_n \rangle, \langle v_n^\dagger c_l^\dagger c_n c_l \rangle$	$\langle b c^\dagger v \rangle$
3	None	None	$\langle b^\dagger b c^\dagger c \rangle, \langle b b c^\dagger v \rangle, \langle b^\dagger b v^\dagger c \rangle$

Table 3.1: Operator expectation values appearing in the CIM.

EV	Cluster expansion
$\langle b^\dagger b \rangle$	$\delta\langle b^\dagger b \rangle + \langle b^\dagger \rangle \langle b \rangle$
$\langle b c^\dagger v \rangle$	$\delta\langle b c^\dagger v \rangle + \langle c^\dagger v \rangle \langle b \rangle$
$\langle c_l^\dagger v_n^\dagger v_l c_n \rangle$	$\delta\langle c_l^\dagger v_n^\dagger v_l c_n \rangle + \langle c_l^\dagger c_n \rangle \langle v_n^\dagger v_l \rangle - \langle c_l^\dagger v_l \rangle \langle v_n^\dagger c_n \rangle$
$\langle v_n^\dagger c_l^\dagger c_n c_l \rangle$	$\delta\langle v_n^\dagger c_l^\dagger c_n c_l \rangle + \langle v_n^\dagger c_l \rangle \langle c_l^\dagger c_n \rangle - \langle v_n^\dagger c_n \rangle \langle c_l^\dagger c_l \rangle$
$\langle b^\dagger b c^\dagger c \rangle$	$\delta\langle b^\dagger b c^\dagger c \rangle + \langle b^\dagger \rangle \langle b \rangle \langle c^\dagger c \rangle + \langle c^\dagger c \rangle \delta\langle b^\dagger b \rangle$
$\langle b b c^\dagger v \rangle$	$\delta\langle b b c^\dagger v \rangle + \langle b \rangle^2 \langle c^\dagger v \rangle + 2\langle b \rangle \delta\langle b c^\dagger v \rangle$
$\langle b^\dagger b v^\dagger c \rangle$	$\delta\langle b^\dagger b v^\dagger c \rangle + \langle b^\dagger \rangle \langle b \rangle \langle v^\dagger c \rangle + \langle b \rangle \delta\langle b^\dagger v^\dagger c \rangle + \langle v^\dagger c \rangle \delta\langle b^\dagger b \rangle$

Table 3.2: Table containing all cluster expansions of the EV in Table 3.1. All Bosonic operators are assumed to act on the cavity lasing mode s thus the subscript is dropped.

EV	Lower order EV products
$\langle b^\dagger b c^\dagger c \rangle$	$\langle c^\dagger c \rangle \langle b^\dagger b \rangle - 2\langle b^\dagger \rangle \langle b \rangle \langle c^\dagger c \rangle$
$\langle b b c^\dagger v \rangle$	$2\langle b \rangle \langle b c^\dagger v \rangle - \langle b \rangle^2 \langle c^\dagger v \rangle$
$\langle b^\dagger b v^\dagger c \rangle$	$\langle b \rangle \langle b^\dagger v^\dagger c \rangle + \langle v^\dagger c \rangle \langle b^\dagger b \rangle - \langle b^\dagger \rangle \langle b \rangle \langle v^\dagger c \rangle$

Table 3.3: Table containing the three-particle EV expanded as lower order expectation value products. The cluster expansion is applied first and then all correlations are recast in terms of EV using the identities given in Table 3.2.

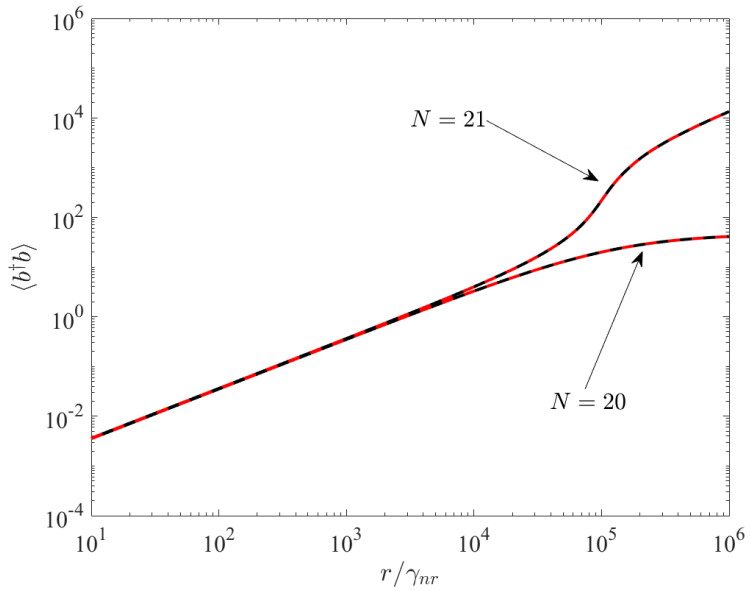

Figure 3.2: Plotting the photon number as a function of the pump for the correlation (black solid) and EV (red dashed) models. Parameter values: $\gamma = 10^4$, $\gamma_{nr} = 1$, $\gamma_c = 10$, $\gamma_{nl} = 1400$ and $g = 70$.

3.7 Model including the operator term $bc^\dagger c$

In this section the CIM is expanded to include the EV and correlation of the operator product of the field and carrier population, $bc^\dagger c$. This is a mixed two particle operator that does not appear in the system Hamiltonian. The extended correlation based CIM

is thus given by the following system of equations

$$d_t\langle c_l^\dagger c_l\rangle = r(1-\langle c_l^\dagger c_l\rangle) - (\gamma_{nl}+\gamma_{nr})\langle c_l^\dagger c_l\rangle - 2\mathfrak{Re}[g_l(\delta\langle bc_l^\dagger v_l\rangle + \langle b\rangle\langle c_l^\dagger v_l\rangle)], \tag{3.57}$$

$$d_t\delta\langle b^\dagger b\rangle = -2\gamma_c\delta\langle b^\dagger b\rangle + 2\mathfrak{Re}\sum_n g_n\delta\langle bc_n^\dagger v_n\rangle, \tag{3.58}$$

$$\begin{aligned} d_t\delta\langle bc_l^\dagger v_l\rangle = &-(\gamma+\gamma_c-i\Delta\nu)\delta\langle bc_l^\dagger v_l\rangle + g_l^*[\langle c_l^\dagger c_l\rangle + \delta\langle b^\dagger b\rangle(2\langle c_l^\dagger c_l\rangle - 1) \\ &- |\langle v_l^\dagger c_l\rangle|^2 + 2\langle b^\dagger\rangle\delta\langle bc_l^\dagger c_l\rangle], \end{aligned} \tag{3.59}$$

$$d_t\langle b\rangle = -(\gamma_c+i\nu)\langle b\rangle + \sum_n g_n^*\langle v_n^\dagger c_n\rangle, \tag{3.60}$$

$$d_t\langle v_l^\dagger c_l\rangle = -(\gamma+i\nu_{\varepsilon_l})\langle v_l^\dagger c_l\rangle + g_l[2\delta\langle bc_l^\dagger c_l\rangle + 2\langle b\rangle\langle c_l^\dagger c_l\rangle - \langle b\rangle], \tag{3.61}$$

$$\begin{aligned} d_t\delta\langle bc_l^\dagger c_l\rangle = &-(\gamma_c+\gamma_{nr}+i\nu_s)\delta\langle b_s c_l^\dagger c_l\rangle - g_l\langle b\rangle\delta\langle bc_l^\dagger v_l\rangle - g_l^*[\langle v_l^\dagger c_l\rangle\delta\langle b^\dagger b\rangle \\ &+ \langle c_l^\dagger c_l\rangle\langle v_l^\dagger c_l\rangle], \end{aligned} \tag{3.62}$$

where $\delta\langle bc^\dagger c\rangle$ enters into the system by coupling to the standard and assisted polarisations. Once more, the operator EVs and corresponding cluster expansion are found in Table 3.4 and Table 3.5, respectively. By inspecting Eq. (3.62) we can see that the decay rate for $\delta\langle bc^\dagger c\rangle$ is on the same order as that of the coherent field amplitude $\langle b\rangle$. This is orders of magnitude smaller than the decay rate of the polarisation thus we cannot neglect it on the grounds that it decays much faster than the other variables.

Using the identities given in Table 3.6 we recast Eqs. (3.57) - (3.62) into the equiv-

Particle order	Bosonic	Fermionic	Mixed
1	$\langle b \rangle$	$\langle c^\dagger c \rangle, \langle v^\dagger c \rangle$	N/A
2	$\langle b^\dagger b \rangle$	$\langle c_l^\dagger v_n^\dagger v_l c_n \rangle, \langle v_n^\dagger c_l^\dagger c_n c_l \rangle$	$\langle b c^\dagger v \rangle, \langle b c^\dagger c \rangle$
3	None	None	$\langle b^\dagger b c^\dagger c \rangle, \langle b b c^\dagger v \rangle, \langle b^\dagger b v^\dagger c \rangle$

Table 3.4: Table containing all of the EV that appear in the model truncated at the two-particle level where $\langle bb \rangle$ and $\langle b v^\dagger c \rangle$ are neglected.

alent EV based model

$$d_t\langle c_l^\dagger c_l\rangle = r(1-\langle c_l^\dagger c_l\rangle) - (\gamma_{nl}+\gamma_{nr})\langle c_l^\dagger c_l\rangle - 2\mathfrak{Re}(g_l\langle b c_l^\dagger v_l\rangle), \tag{3.63}$$

$$d_t\langle b^\dagger b\rangle = -2\gamma_c\langle b^\dagger b\rangle + 2\mathfrak{Re}\sum_n g_n\langle b c_n^\dagger v_n\rangle, \tag{3.64}$$

$$\begin{aligned} d_t\langle b c_l^\dagger v_l\rangle = &-(\gamma+\gamma_c+i\Delta\nu)\langle b c_l^\dagger v_l\rangle + g_l^*[\langle c_l^\dagger c_l\rangle + \langle b^\dagger b\rangle(2\langle c_l^\dagger c_l\rangle - 1) \\ &- 4\langle b^\dagger\rangle\langle b\rangle\langle c_l^\dagger c_l\rangle + 4\mathfrak{Re}(\langle b\rangle\langle b^\dagger c_l^\dagger c_l\rangle)] + \langle c_l^\dagger v_l\rangle\sum_{n\neq l} g_n^*\langle v_n^\dagger c_n\rangle, \end{aligned} \tag{3.65}$$

$$d_t\langle b\rangle = -(\gamma_c+i\nu)\langle b\rangle + \sum_n g_n^*\langle v_n^\dagger c_n\rangle, \tag{3.66}$$

$$d_t\langle v_l^\dagger c_l\rangle = -(\gamma+i\nu_{\varepsilon_l})\langle v_l^\dagger c_l\rangle + g_l[2\langle b c_l^\dagger c_l\rangle - \langle b\rangle], \tag{3.67}$$

$$\begin{aligned} d_t\langle b c_l^\dagger c_l\rangle = &-(\gamma_c+\gamma_{nr}+i\nu_s)\langle b_s c_l^\dagger c_l\rangle - \gamma_{nl}\langle b\rangle\langle c_l^\dagger c_l\rangle - g_l[2\langle b\rangle\langle b c_l^\dagger v_l\rangle - \langle b\rangle^2\langle c_l^\dagger v_l\rangle] \\ &- g_l^*[\langle v_l^\dagger c_l\rangle(\langle b^\dagger b\rangle - \langle b^\dagger\rangle\langle b\rangle) + \langle b\rangle\langle b^\dagger v_l^\dagger c_l\rangle] + \langle c_l^\dagger c_l\rangle\sum_{n\neq l} g_n^*\langle v_n^\dagger c_n\rangle. \end{aligned} \tag{3.68}$$

Fig. (3.3) illustrates once again that the correlation based model is mathematically equivalent with EV based model. However, it is also clear to see that a strange artefact is now present in the intensity response which now displays a dip. This makes it apparent that although we cannot ignore this term, it is not enough on its own and we will see in the following section that other terms are needed to correct the dip shown in the intensity.

EV	Cluster expansion
$\langle b^\dagger b\rangle$	$\delta\langle b^\dagger b\rangle + \langle b^\dagger\rangle\langle b\rangle$
$\langle bc^\dagger c\rangle$	$\delta\langle bc^\dagger c\rangle + \langle c^\dagger c\rangle\langle b\rangle$
$\langle bc^\dagger v\rangle$	$\delta\langle bc^\dagger v\rangle + \langle c^\dagger v\rangle\langle b\rangle$
$\langle c_l^\dagger v_n^\dagger v_l c_n\rangle$	$\boldsymbol{\delta\langle c_l^\dagger v_n^\dagger v_l c_n\rangle} + \langle c_l^\dagger c_n\rangle\langle v_n^\dagger v_l\rangle - \langle c_l^\dagger v_l\rangle\langle v_n^\dagger c_n\rangle$
$\langle v_n^\dagger c_l^\dagger c_n c_l\rangle$	$\boldsymbol{\delta\langle v_n^\dagger c_l^\dagger c_n c_l\rangle} + \langle v_n^\dagger c_l\rangle\langle c_l^\dagger c_n\rangle - \langle v_n^\dagger c_n\rangle\langle c_l^\dagger c_l\rangle$
$\langle b^\dagger bc^\dagger c\rangle$	$\boldsymbol{\delta\langle b^\dagger bc^\dagger c\rangle} + \langle b^\dagger\rangle\langle b\rangle\langle c^\dagger c\rangle + \langle c^\dagger c\rangle\delta\langle b^\dagger b\rangle + \langle b^\dagger\rangle\delta\langle bc^\dagger c\rangle + \langle b\rangle\delta\langle b^\dagger c^\dagger c\rangle$
$\langle bbc^\dagger v\rangle$	$\boldsymbol{\delta\langle bbc^\dagger v\rangle} + \langle b\rangle^2\langle c^\dagger v\rangle + 2\langle b\rangle\delta\langle bc^\dagger v\rangle$
$\langle b^\dagger bv^\dagger c\rangle$	$\boldsymbol{\delta\langle b^\dagger bv^\dagger c\rangle} + \langle b^\dagger\rangle\langle b\rangle\langle v^\dagger c\rangle + \langle b\rangle\delta\langle b^\dagger v^\dagger c\rangle + \langle v^\dagger c\rangle\delta\langle b^\dagger b\rangle$

Table 3.5: Table containing all cluster expansions of the EV in Table 3.4 where the terms in bold are thrown away at first sight in line with our approximations. All Bosonic operators are assumed to act on the cavity lasing mode s thus the subscript is dropped.

EV	Lower order EV products
$\langle b^\dagger bc^\dagger c\rangle$	$\langle c^\dagger c\rangle\langle b^\dagger b\rangle + \langle b^\dagger\rangle\langle bc^\dagger c\rangle + \langle b\rangle\langle b^\dagger c^\dagger c\rangle - 2\langle b^\dagger\rangle\langle b\rangle\langle c^\dagger c\rangle$
$\langle bbc^\dagger v\rangle$	$2\langle b\rangle\langle bc^\dagger v\rangle - \langle b\rangle^2\langle c^\dagger v\rangle$
$\langle b^\dagger bv^\dagger c\rangle$	$\langle b\rangle\langle b^\dagger v^\dagger c\rangle + \langle v^\dagger c\rangle\langle b^\dagger b\rangle - \langle b^\dagger\rangle\langle b\rangle\langle v^\dagger c\rangle$

Table 3.6: Table containing the three-particle EV expanded as lower order expectation value products. The cluster expansion is applied first and then all correlations are recast in terms of EV using the identities given in Table 3.5.

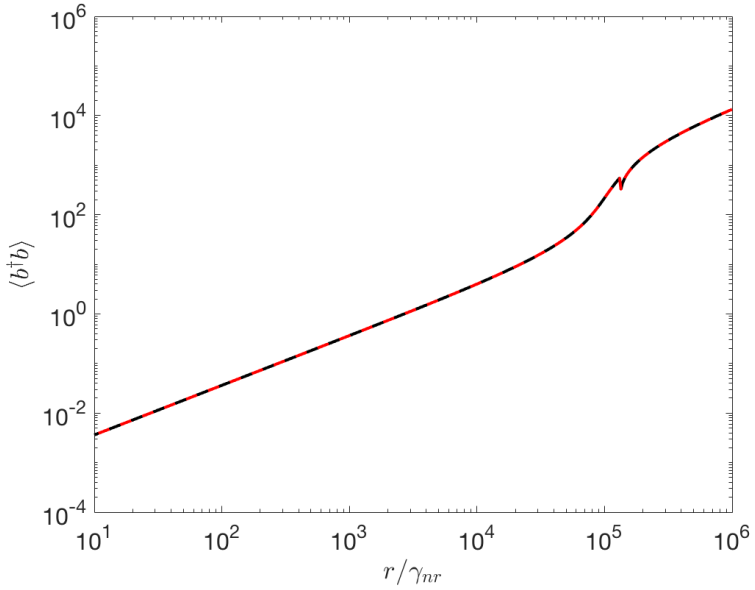

Figure 3.3: Plotting the photon number as a function of the pump for the correlation (black solid) and EV (red dashed) models where the term $\delta\langle bc^\dagger c\rangle$ ($\langle bc^\dagger c\rangle$) is not neglected. Parameter values: $\gamma = 10^4$, $\gamma_{nr} = 1$, $\gamma_c = 10$, $\gamma_{nl} = 1400$, $g = 70$ and $N = 21$.

3.8 All two-particle terms (except pure carrier terms)

Finally, we include the models in terms of correlations and EVs where the operator terms bb and $bv^\dagger c$ and their equations of motion are included. At the operator level, i.e., the system Hamiltonian, terms like this and their complex conjugates are neglected as under the RWA. However, they appear explicitly in the Heisenberg equation for $bc^\dagger c$ and implicitly through the three-particle operator terms; the cluster expansion of the higher order terms reveals them. Although these terms are not present in the system Hamiltonian they are present in the conservative part of the Heisenberg equations and through the Lindblad dissipative terms one can see that their losses are the same as the photon number and assisted polarisation, thus there can be no grounds for neglecting them due to rapid decay processes.

Using Table 3.7 and Table 3.8 the model, in terms of correlations, is then

$$d_t\langle b\rangle = -(\gamma_c + i\nu)\langle b\rangle + \sum_n g_n^*\langle v_n^\dagger c_n\rangle, \tag{3.69}$$

$$d_t\langle v_l^\dagger c_l\rangle = -(\gamma + i\nu_{\varepsilon_l})\langle v_l^\dagger c_l\rangle + g_l[2\delta\langle bc_l^\dagger c_l\rangle + 2\langle b\rangle\langle c_l^\dagger c_l\rangle - \langle b\rangle], \tag{3.70}$$

$$d_t\langle c_l^\dagger c_l\rangle = r(1 - \langle c_l^\dagger c_l\rangle) - (\gamma_{nl} + \gamma_{nr})\langle c_l^\dagger c_l\rangle - 2\mathfrak{Re}[g_l(\delta\langle bc_l^\dagger v_l\rangle + \langle b\rangle\langle c_l^\dagger v_l\rangle)], \tag{3.71}$$

$$d_t\delta\langle b^\dagger b\rangle = -2\gamma_c\delta\langle b^\dagger b\rangle + 2\mathfrak{Re}\sum_n g_n\delta\langle bc_n^\dagger v_n\rangle, \tag{3.72}$$

$$\begin{aligned} d_t\delta\langle bc_l^\dagger v_l\rangle = &-(\gamma + \gamma_c - i\Delta\nu)\delta\langle bc_l^\dagger v_l\rangle + g_l^*[\langle c_l^\dagger c_l\rangle + \delta\langle b^\dagger b\rangle(2\langle c_l^\dagger c_l\rangle - 1) \\ &- |\langle v_l^\dagger c_l\rangle|^2 + 2\langle b^\dagger\rangle\delta\langle bc_l^\dagger c_l\rangle], \end{aligned} \tag{3.73}$$

$$\begin{aligned} d_t\delta\langle bc_l^\dagger c_l\rangle = &-(\gamma_c + \gamma_{nr} + i\nu_s)\delta\langle b_s c_l^\dagger c_l\rangle - g_l[\langle c_l^\dagger v_l\rangle\boldsymbol{\delta\langle bb\rangle} + \langle b\rangle\delta\langle bc_l^\dagger v_l\rangle] \\ &- g_l^*[\langle b^\dagger\rangle\boldsymbol{\delta\langle bv_l^\dagger c_l\rangle} + \langle v_l^\dagger c_l\rangle\delta\langle b^\dagger b\rangle + \langle c_l^\dagger c_l\rangle\langle v_l^\dagger c_l\rangle], \end{aligned} \tag{3.74}$$

$$d_t\delta\langle bb\rangle = -2(\gamma_c + i\nu)\delta\langle bb\rangle + 2\sum_n g_{sn}^*\delta\langle bv_n^\dagger c_n\rangle, \tag{3.75}$$

$$\begin{aligned} d_t\delta\langle bv_l^\dagger c_l\rangle = &-[\gamma + \gamma_c + i(\nu + \nu_{\varepsilon_l})]\delta\langle bv_l^\dagger c_l\rangle + g_l[\delta\langle bb\rangle(2\langle c_l^\dagger c_l\rangle - 1) \\ &+ 2\langle b\rangle\delta\langle bc_l^\dagger c_l\rangle] - g_l^*\langle v_l^\dagger c_l\rangle^2, \end{aligned} \tag{3.76}$$

where $\Delta\nu = \Delta_\varepsilon - \nu$ and the new variables enter the equation for $\delta\langle bc^\dagger c\rangle$ (shown in bold). For the last time we make use of the identities in Table in order to transform

Particle order	Bosonic	Fermionic	Mixed
1	$\langle b\rangle$	$\langle c^\dagger c\rangle, \langle v^\dagger c\rangle$	N/A
2	$\langle b^\dagger b\rangle, \langle bb\rangle$	$\langle c_l^\dagger v_n^\dagger v_l c_n\rangle, \langle v_n^\dagger c_l^\dagger c_n c_l\rangle, \langle v_n^\dagger v_l^\dagger c_n c_l\rangle$	$\langle bc^\dagger v\rangle, \langle bc^\dagger c\rangle, \langle bv^\dagger c\rangle$
3	None	None	$\langle b^\dagger bc^\dagger c\rangle, \langle bbc^\dagger v\rangle, \langle b^\dagger bv^\dagger c\rangle, \langle bbc^\dagger c\rangle$

Table 3.7: Table containing all of the EV that appear in the model truncated at the two-particle level where two-particle carrier terms are neglected.

between models. The EV based model is thus given by

$$d_t\langle b\rangle = -(\gamma_c + i\nu)\langle b\rangle + \sum_n g_n^*\langle v_n^\dagger c_n\rangle, \tag{3.77}$$

$$d_t\langle v_l^\dagger c_l\rangle = -(\gamma + i\nu_{\varepsilon_l})\langle v_l^\dagger c_l\rangle + g_l[2\langle bc_l^\dagger c_l\rangle - \langle b\rangle], \tag{3.78}$$

$$d_t\langle c_l^\dagger c_l\rangle = r(1 - \langle c_l^\dagger c_l\rangle) - (\gamma_{nl} + \gamma_{nr})\langle c_l^\dagger c_l\rangle - 2\mathfrak{Re}(g_l\langle bc_l^\dagger v_l\rangle), \tag{3.79}$$

$$d_t\langle b^\dagger b\rangle = -2\gamma_c\langle b^\dagger b\rangle + 2\mathfrak{Re}\sum_n g_n\langle bc_n^\dagger v_n\rangle, \tag{3.80}$$

$$\begin{aligned} d_t\langle bc_l^\dagger v_l\rangle = &-(\gamma + \gamma_c + i\Delta\nu)\langle bc_l^\dagger v_l\rangle + g_l^*[\langle c_l^\dagger c_l\rangle + \langle b^\dagger b\rangle(2\langle c_l^\dagger c_l\rangle - 1) \\ &- 4\langle b^\dagger\rangle\langle b\rangle\langle c_l^\dagger c_l\rangle + 4\mathfrak{Re}(\langle b\rangle\langle b^\dagger c_l^\dagger c_l\rangle)] + \langle c_l^\dagger v_l\rangle\sum_{n\neq l} g_n^*\langle v_n^\dagger c_n\rangle, \end{aligned} \tag{3.81}$$

$$\begin{aligned} d_t\langle bc_l^\dagger c_l\rangle = &-(\gamma_c + \gamma_{nr} + i\nu_s)\langle b_s c_l^\dagger c_l\rangle - \gamma_{nl}\langle b\rangle\langle c_l^\dagger c_l\rangle - g_l[2\langle b\rangle\langle bc_l^\dagger v_l\rangle \\ &- 2\langle b\rangle^2\langle c_l^\dagger v_l\rangle + \langle c_l^\dagger v_l\rangle\langle bb\rangle] - g_l^*[\langle b^\dagger\rangle\langle bv_l^\dagger c_l\rangle - 2\langle b^\dagger\rangle\langle b\rangle\langle v_l^\dagger c_l\rangle \\ &+ \langle v_l^\dagger c_l\rangle\langle b^\dagger b\rangle + \langle b\rangle\langle b^\dagger v_l^\dagger c_l\rangle] + \langle c_l^\dagger c_l\rangle\sum_{n\neq l} g_n^*\langle v_n^\dagger c_n\rangle + r\langle b\rangle(1 - \langle c^\dagger c_l\rangle), \end{aligned} \tag{3.82}$$

$$\begin{aligned} d_t\langle bv_l^\dagger c_l\rangle = &-[\gamma + \gamma_c + i(\nu + \nu_{\varepsilon_l})]\langle bv_l^\dagger c_l\rangle + g_l[\langle bb\rangle(2\langle c_l^\dagger c_l\rangle - 1) - 4\langle b\rangle^2\langle c_l^\dagger c_l\rangle \\ &+ 4\langle b\rangle\langle bc_l^\dagger c_l\rangle] + \langle v_l^\dagger c_l\rangle\sum_{n\neq l} g_n^*\langle v_n^\dagger c_n\rangle, \end{aligned} \tag{3.83}$$

$$d_t\langle bb\rangle = -2(\gamma_c + i\nu)\langle bb\rangle + 2\sum_n g_{sn}^*\langle bv_n^\dagger c_n\rangle. \tag{3.84}$$

From Fig. 3.4 we can see that the additional terms bb and $bv^\dagger c$ and their equations have resulted in a correction of the dip which was caused by considering only bcc as an addition to the CIM.

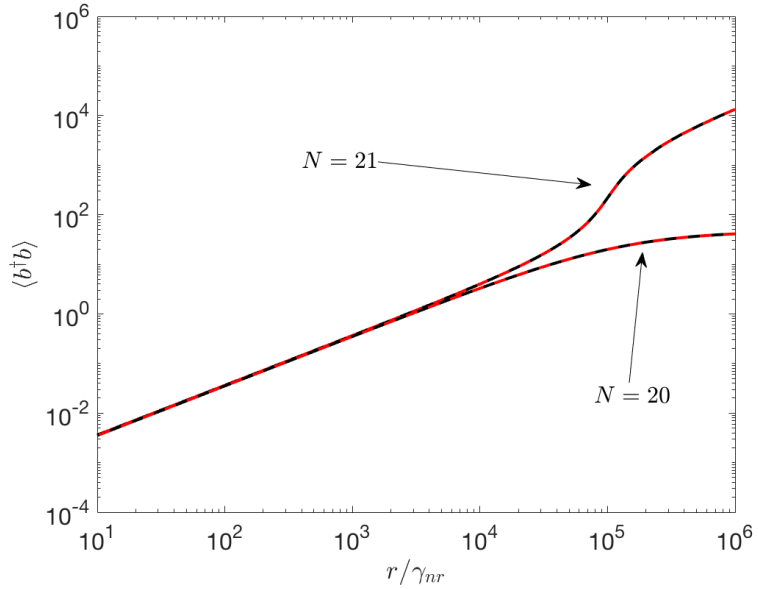

Figure 3.4: Plotting the photon number as a function of the pump for the correlation (black solid) and EV (red dashed) models where the correlations (EVs) of the two-photon like terms $bb, bv^\dagger c$ are included. Parameter values: $\gamma = 10^4$, $\gamma_{nr} = 1$, $\gamma_c = 10$, $\gamma_{nl} = 1400$ and $g = 70$.

EV	Cluster expansion
$\langle b^\dagger b\rangle$	$\delta\langle b^\dagger b\rangle + \langle b^\dagger\rangle\langle b\rangle$
$\langle bc^\dagger c\rangle$	$\delta\langle bc^\dagger c\rangle + \langle c^\dagger c\rangle\langle b\rangle$
$\langle bc^\dagger v\rangle$	$\delta\langle bc^\dagger v\rangle + \langle c^\dagger v\rangle\langle b\rangle$
$\langle c_l^\dagger v_n^\dagger v_l c_n\rangle$	$\boldsymbol{\delta\langle c_l^\dagger v_n^\dagger v_l c_n\rangle} + \langle c_l^\dagger c_n\rangle\langle v_n^\dagger v_l\rangle - \langle c_l^\dagger v_l\rangle\langle v_n^\dagger c_n\rangle$
$\langle v_n^\dagger c_l^\dagger c_n c_l\rangle$	$\boldsymbol{\delta\langle v_n^\dagger c_l^\dagger c_n c_l\rangle} + \langle v_n^\dagger c_l\rangle\langle c_l^\dagger c_n\rangle - \langle v_n^\dagger c_n\rangle\langle c_l^\dagger c_l\rangle$
$\langle b^\dagger bc^\dagger c\rangle$	$\boldsymbol{\delta\langle b^\dagger bc^\dagger c\rangle} + \langle b^\dagger\rangle\langle b\rangle\langle c^\dagger c\rangle + \langle c^\dagger c\rangle\delta\langle b^\dagger b\rangle + \langle b^\dagger\rangle\delta\langle bc^\dagger c\rangle + \langle b\rangle\delta\langle b^\dagger c^\dagger c\rangle$
$\langle bbc^\dagger v\rangle$	$\boldsymbol{\delta\langle bbc^\dagger v\rangle} + \langle b\rangle^2\langle c^\dagger v\rangle + \langle c^\dagger v\rangle\delta\langle bb\rangle + 2\langle b\rangle\delta\langle bc^\dagger v\rangle$
$\langle b^\dagger bv^\dagger c\rangle$	$\boldsymbol{\delta\langle b^\dagger bv^\dagger c\rangle} + \langle b^\dagger\rangle\langle b\rangle\langle v^\dagger c\rangle + \langle b\rangle\delta\langle b^\dagger v^\dagger c\rangle + \langle b^\dagger\rangle\delta\langle bv^\dagger c\rangle + \langle v^\dagger c\rangle\delta\langle b^\dagger b\rangle$
$\langle bbc^\dagger c\rangle$	$\boldsymbol{\delta\langle bbc^\dagger c\rangle} + \langle b\rangle^2\langle c^\dagger c\rangle + 2\langle b\rangle\delta\langle bc^\dagger c\rangle + \langle c^\dagger c\rangle\langle bb\rangle$
$\langle bb\rangle$	$\delta\langle bb\rangle + \langle b\rangle^2$
$\langle bv^\dagger c\rangle$	$\delta\langle bv^\dagger c\rangle + \langle b\rangle\langle v^\dagger c\rangle$
$\langle v_n^\dagger v_l^\dagger c_n c_l\rangle$	$\boldsymbol{\delta\langle v_n^\dagger v_l^\dagger c_n c_l\rangle} + \langle v_n^\dagger c_l\rangle\langle v_l^\dagger c_n\rangle - \langle v_n^\dagger c_n\rangle\langle v_l^\dagger c_l\rangle$

Table 3.8: Table containing all cluster expansions of the EV in Table 3.7 where the terms in bold are thrown away at first sight in line with our approximations. All Bosonic operators are assumed to act on the cavity lasing mode s thus the subscript is dropped.

EV	Lower order EV products
$\langle b^\dagger bc^\dagger c\rangle$	$\langle c^\dagger c\rangle\langle b^\dagger b\rangle + \langle b^\dagger\rangle\langle bc^\dagger c\rangle + \langle b\rangle\langle b^\dagger c^\dagger c\rangle - 2\langle b^\dagger\rangle\langle b\rangle\langle c^\dagger c\rangle$
$\langle bbc^\dagger v\rangle$	$2\langle b\rangle\langle bc^\dagger v\rangle - 2\langle b\rangle^2\langle c^\dagger v\rangle + \langle c^\dagger v\rangle\langle bb\rangle$
$\langle b^\dagger bv^\dagger c\rangle$	$\langle b\rangle\langle b^\dagger v^\dagger c\rangle + \langle v^\dagger c\rangle\langle b^\dagger b\rangle - 2\langle b^\dagger\rangle\langle b\rangle\langle v^\dagger c\rangle + \langle b^\dagger\rangle\delta\langle bv^\dagger c\rangle$

Table 3.9: Table containing the three-particle EV expanded as lower order expectation value products. The cluster expansion is applied first and then all correlations are recast in terms of EV using the identities given in Table 3.8.

3.9 Overview of chapter

In this chapter we have derived the system Hamiltonian and introduced the cluster expansion which allows for the systematic truncation of the equations of motion, decoupling them from higher-order correlations. The Heisenberg equations for all two-particle operator terms (excluding pure carrier operators greater than the single-particle level) have been given along with two types of models which are mathematically equivalent: (1) a correlation based model; and (2) an EV based model. We have illustrated that operator terms typically neglected, i.e. $bc^\dagger c, bb$ and $bv^\dagger c$, cannot be ignored as made clear by their rate of dissipation. Nevertheless, the order in which these terms are included, or not, is important. By only including the correlation (EV) term $\delta\langle bc^\dagger c\rangle$ ($\langle bc^\dagger c\rangle$) resulted in a surprising dip in the intensity as a function of the pump which is not accounted for. However, by including the operator terms neglected in the system Hamiltonian due to the RWA we recover the results of the CIM where the dip in intensity is corrected.

Chapter 4

Identical Emitters - A Justification

In the following chapters we assume that the coupling strength between the field and emitters is constant therefore all emitters N are modelled as being identical. In this brief chapter, the justification for this approximation is made.

Fluctuations in the coupling strength between e.m. field in the cavity and QDs can be ascribed to two different sources: 1. QD positioning relative to the local field value – which can be further decomposed into longitudinal and transverse distribution position –, and 2. QD spectral inhomogeneous broadening.

See **Appendix D** for simulations accounting for non-identical QDs.

4.1 Longitudinal positioning errors

We consider as an example a micropillar configuration (VCSEL-style) to fix the ideas. The technology is quite well established and a good example of the layers and their construction can be found in [35]. Quantum Dots are grown onto a wetting layer, made up of a Quantum Well (QW) with typical thickness $< 2nm$, and occupy themselves a layer of typical thickness $t_{QD} \approx 0.9nm$ [35] (other authors give up to $1.5nm$ [36], but the order of magnitude remains). Thus, we can estimate a total thickness for the combination QW/QD layer to be of the order of $3nm$ (others give $5nm$ for multiple

superposed layers) – Fig. 7 in [37]). Four layers would add to approximately $T_4 \approx 20nm$, depending on the specific realizations, i.e., $\pm 10nm$ around the peak of the field amplitude.

The cavity length, for a vacuum wavelength $\lambda_0 = 1\mu m$ in GaAs ($n \approx 3.3$), is $L = \frac{\lambda_0}{2n} \approx 150nm$ (the factor 2 in the denominator stems from the half-wavelength, standard cavity configuration), while the positioning uncertainty is at the monolayer level ($M \approx 3$ Å [38]). The error in the e.m. field strength, since the positioning is near the maximum, will be given by $\frac{\Delta z}{L}$, where with Δz we denote the generic positioning error.

Thus, we can examine three sources of longitudinal *error*:

a. Layer positioning: $\frac{M}{L} \approx 0.002$, which provides a negligible error ($O(10^{-6})$).

b. QD layer thickness: $\left(\frac{t_{QD}}{L}\right) \approx 0.007$, whose repercussion onto the field amplitude is $< 5 \times 10^{-5}$.

c. Multiple QD layer thickness: $\left(\frac{T_4}{2L}\right) \approx 0.07$, which amounts to a change in relative field amplitude $< 5 \times 10^{-3}$. Notice that we have considered four consecutive QWs in the example. Typically, this is done to obtain a larger amount of output power and, so far, it has not been used for nanolasers. Each QW will support a number N_{QD}. This is the number to which we refer in the transverse positioning analysis, which holds for any QW. Thus, we can think of the multiple QWs as supports which permit a multiplication by N_{QW} (number of QWs) of the number of QDs on each wetting layer. The "cost" in positioning error due to the additional layers remains negligible compared to the transverse positioning and can be considered a good strategy to increase the output power. It must also be noted that this scheme of stacking multiple QW can be scaled up by increasing the length of the cavity and distributing them on the different antinodes of the cavity mode. The implementation will dictate this strategy, i.e., it may be counter productive to increase the length of the cavity, thus the half wavelength restriction is kept; in this case the more QW that are stacked will increase the amount of off-resonance QDs. The final scheme implemented will depend greatly on the application of the

device.

4.2 Transverse positioning errors

The second source of coupling fluctuations is related to the transverse positioning of the QDs, due to the transverse shape of the intracavity electromagnetic field. Micropillar cavities (but the same holds for Photonic Crystals – PhC) operate on a single transverse mode (well-approximated by a Gaussian distribution) for diameters up to and beyond $3\mu m$ (high-quality commercial VCSELs are fabricated and sold with an excellent transverse field distribution by Philips-Ulm [39], for instance, with a diameter which can be estimated around 5 or $6\mu m$).

The important question is to know what the typical inter-QD distance may be to figure out how many QDs can be placed inside the modal volume.

Ref. [40] answers this question by indicating a QD density of the order of $10^{10} cm^{-2}$ (value confirmed by other sources, as well [41]). This provides an estimate for the QD surface density $\sigma_{QD} \approx 10^2 \mu m^{-2}$ (i.e., an interdot distance $d_{QD} \approx 100nm$), with a corresponding linear density $\mu_{QD} \approx 10\, QD\, \mu m^{-1}$.

Defining the diameter for the intensity of the gaussian beam r_I, we can extract from it the radius of the field r_b [42]:

$$r_b = \frac{\sqrt{2}}{2} r_I \,. \tag{4.1}$$

where the beam radius is given by the usual defintion $r_b = \frac{1}{e^2}$. Given the surface density of QDs (σ_{QD}) or its equivalent linear density (μ_{QD}), we can compute the radius of the area occupied by the QDs as follows:

$$r_d = \frac{\sqrt{N_{QD}}}{\mu_{QD}} \,. \tag{4.2}$$

As mentioned at the beginning of this section, the e.m. field in small cavities is well-approximated by a transverse, 2D gaussian function extending over the plane of the QDs. We are going to use the gaussian shape to compare the maximum deviation of

the field strength (relative to its on-axis value) by using the unnormalized Gaussian

$$G(r) \quad = \quad e^{-\frac{r^2}{2r_b^2}}, \tag{4.3}$$

where r describes the distance from the optical axis and whose maximum is $G(r = 0) = 1$. The value of the gaussian at the outer edge of the disk occupied by the QDs gives therefore a direct ratio of the local field strength to the maximum one, on-axis, and estimates the maximum deviation in field strength experienced by the QDs across the surface.

Three quantities can be easily plotted: $r_d(N_{QD})$, $G(r_b)$ and $G(N_{QD})$, where the latter uses simultaneously Eq. (4.3) and the inverted Eq. (4.2). Of course, the underlying assumption is that the QDs are homogeneously distributed across the allowed section.

Fig. 4.1 shows that up to $N_{QD} \approx 100$ the error is of the order of a few percent (4% for 100 QDs). Whereas, the error grows much larger when we reach 1000 QDs. One has to keep in mind that it is possible, for the future, to consider multiple QW layers supporting the same QD density ($N_{QW} = 5$ has already been implemented, even though for larger power applications).

4.3 Inhomogenous broadening

Technological developments have strongly improved the size homogeneity of QDs, thus leading to closer resonance frequencies and providing samples with a good degree of homogenous broadening. While in the early 2000s it was possible to observe wavelength (or energy) spreads of the order of 10%, current realizations are capable of obtaining $\gtrsim 60\%$ of QDs in a frequency interval which is within 0.4% of the common resonance wavelength (or frequency) [43] . Furthermore, Fig. 1d in [43] shows that the largest relative spread in wavelength (or frequency) observed in experimental samples is $\frac{\Delta\lambda}{\lambda} \approx 0.007$. This implies that we can expect fluctuations in coupling which may be of this order of magnitude, due to the differences in central resonance frequency of the different QDs.

One additional point of interest comes form the comparison between experimentally

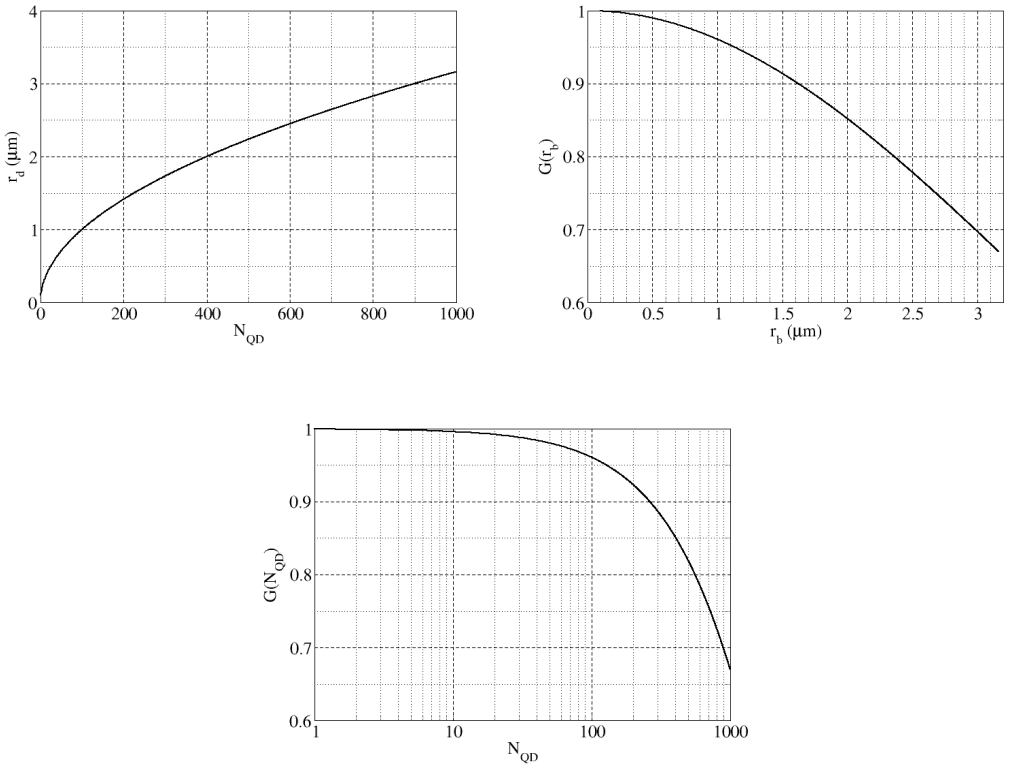

Figure 4.1: Top Left: radius r_b of the area occupied by the QDs as a function of their number, N_{QD}, for a linear density $\mu_{QD} = 10\,QD\,\mu m^{-1}$; Top Right: relative value of the Gaussian field distribution (representing the electric field amplitude for the fundamental TEM_{00} mode) at the radius r_b, relative to its maximum at $r_b = 0$; Bottom Centre: relative value of the Gaussian field distribution $G(N_{QD})$ at the edge of the area occupied by the QDs as a function of the QD number (N_{QD}).

estimated $N_{QD,e}$ and the corresponding one entered in a model which reproduces the experimental results, $N_{QD,m}$. This comparison suggests that 70% of the QDs are within the homogeneous width of the transition [44] and interact with the field. The remainder 30% does not effectively participate in the interaction. In other words, the *effective QD number* interacting with the field $N_{eff} \approx 0.7 \times N_{QD,e}$. This situation can arise due to differences in QD size and shape mean that they cannot couple strongly with the cavity mode. However, the rapid progress of technology promises improvements on relatively short timescales, thus lending further credibility to the realization of samples with high spectral homogeneity.

4.4 Conclusion

In summary, we can safely conclude that the coupling coefficient does not suffer from the longitudinal positioning of the QDs. Likewise, the transverse fluctuations in coupling constant remain in the range of a few percent for most of the reasonable configurations. In step with the rapid advancements in technology and engineering we can safely assume that the majority of the QDs can be considered as *effective emitters*, i.e. interacting with the intra-cavity field. Thus, in the following Chapters we assume that all QDs are identical.

Chapter 5

Thermal, Quantum Antibunching and Lasing Thresholds from Single Emitters to Macroscopic Devices

Mark Anthony Carroll derived the model equations, carried out their analytical analyses and wrote the code to produce the figuers. Reprinted with permission from [3] Copyright 2021 by the American Physical Society.

In this **Chapter** we start from the fully quantized Hamiltonian developed in **Chapter 3** for an ensemble of identical emitters coupled to the modes of an optical cavity, we determine analytically regimes of thermal, collective anti-bunching and laser emission that depend explicitly on the number of emitters. The lasing regime is reached for a number of emitters above a critical number—which depends on the light-matter coupling, detuning, and the dissipation rates—via a universal transition from thermal emission to collective anti-bunching to lasing as the pump increases. Cases where the second order intensity correlation fails to predict laser action are also presented.

Optical cavities containing emitters with discrete energy levels such as atoms, ions or quantum dots, have proved extremely effective both as a tool to investigate fun-

damental properties of light-matter interaction and as a way to produce light with engineered statistical properties. Historically, the earliest optical cavities contained very large numbers of emitters to overcome losses and occupied macroscopic volumes. Significant improvements in cavity quality have led in recent years to micro and nano cavities [17] that provide detectable fields even with very few emitters and promise commercial applications with uses ranging from components on integrated circuits to medicine [45]. Their small size comes with the benefit of lower energy consumption and increased energy efficiency, making them attractive for extreme miniaturization. Although the basic quantum interaction process between the cavity modes and the emitters is the same for all cavities, different approximations of the expectation values of light-matter interaction and photon number (correspondiong to the classical intensity) lead to two classes of models: one for micro and nano systems, the other for macroscopic systems. In the latter, e.g. the Maxwell-Bloch semi-classical models for macroscopic systems [46], the only expectation values considered are those of the emitters' raising and lowering operators, representing excitation and de-excitation of an electron, and of the cavity mode creation and destruction operators, representing emission and absorption of a photon. The expectation values of the destruction and creation operators correspond to the complex amplitude of the classical coherent field and its complex conjugate. Similarly, the expectation values of raising and lowering operators correspond to the amplitude of the medium polarization and its complex conjugate. Macroscopic models neglect correlations among these operators, both in the intensity and in the photon-matter coupling, also called the photon-assisted polarization. This approximation allows one to predict the threshold for laser emission, but is not suitable for the analysis of non-lasing emission because photon-assisted polarization is essential to model correctly spontaneous emission [33]. Quantum models for micro and nano lasers take the exact opposite approach: they consider only the correlations and neglect the expectation values [5, 15, 31, 33] corresponding to the amplitudes of the classical coherent field and polarization. With this approximation non-lasing emission can be modelled, but it is not possible to identify the onset of lasing. The same problem also affects rate equation models of micro- and nanolasers that add average

spontaneous emission to coherent emission, i.e., adding phenomenological terms for spontaneous emission to RE can describe emission above and below the laser threshold, but the threshold itself cannot be identified [1, 7, 23]. A key parameter related to the size of the system is the spontaneous emission factor, β, defined as the ratio of the spontaneous emission rate into the lasing mode to the total spontaneous emission. β^{-1}, proportional to the number of electromagnetic modes in the cavity volume, thus characterises the system size. In macroscopic systems $\beta \ll 1$, while $\beta = 1$ is the nanoscale limit, in which only the lasing mode remains accessible to spontaneous and stimulated emission. For this value of β the output power linearly follows the input power, and for this reason this laser is considered "thresholdless" [7, 22]. This regime poses questions on how to define the laser threshold [23] and identify coherent emission [24], which we address unambiguously in this text.

Starting from a fully quantized Jaynes-Cummings Hamiltonian in the Heisenberg picture, Eq. 3.11, we derive a model for the emission of any number of identical two-level emitters coupled to one mode of the cavity [47, 48]. However, we do not approximate the expectation values of intensity and light-matter interaction, including the variables of both macroscopic and nano lasers, and apply dynamical system methods defined for systems of any dimension [49] to identify the laser threshold. Analytical solutions seamlessly connect single emitter devices with devices containing millions of emitters, predicting where the thermal, quantum and coherent emission regimes lie with respect to one another. While the extent and existence of these regions in the space of parameters depend on the number of emitters, we find two universal features that are common to all lasing devices. The first is that lasing, when possible, is reached via a universal sequence of transitions as the pump is increased. The emission of the non-lasing state evolves continuously from thermal (with second order intensity correlation $1 < g^{(2)}(0) \leq 2$) to anti-bunching (with $0 \leq g^{(2)}(0) < 1$) until the laser threshold is crossed and the non-lasing state becomes unstable. A coherent laser field, due to a lasing collective state, appears at this threshold and its amplitude increases as a function of the pump. This is the same instability predicted for macroscopic laser by Maxwell-Bloch models. However, in these models the total field before the instability is

zero, while in our theory before the threshold only the coherent field is zero, while the incoherent field is non zero. The second universal feature of lasers is that the emerging coherent field has a well defined frequency: our model shows that neither the number of emitters nor the effective cavity volume (β factor) influence the frequency value, which remains a general feature of the cavity-emitter interaction. We give examples where the measurement of $g^{(2)}(0)$ cannot identify laser emission.

We consider identicalemitters with two energy levels and one electron, and assume that all transitions conserve the electron spin. This model applies to atoms and ions with suitable energy level structure, and also to shallow quantum dots (possessing two localized levels) at temperatures low enough to neglect Coulomb and phonon interactions. Assuming that detuning and coupling coefficients with the mode are identical [15, 40] is justified by numerical simulations for emitters with 10% random variations of detuning and coupling coefficients. In these simulations all emitters' variables – started from random initial conditions – after a transient converge to common values that match extremely well those obtained using the same parameters and expectation values for all emitters, see SM Fig. 2.

In the following $c^\dagger$, $v^\dagger$, $b^\dagger$ (c, v, b) are operators that create (annihilate), respectively, an electron in the upper energy level (conduction level in quantum dot terminology), in the lower energy level (valence level), and a photon in the laser mode. We take the expectation values of the Heisenberg equations for each operator in the Hamiltonian, truncating the resulting infinite hierarchy of coupled differential equations by keeping only correlation functions that appear in the cluster expansion of the Hamiltonian [33, 47]. The variables of the model are the expectation values of carrier population, $\langle c^\dagger c\rangle$, mode destruction operator, $\langle b\rangle$, and emitter lowering operator, $\langle v^\dagger c\rangle$, and the intensity and photon-polarization correlations, $\delta\langle b^\dagger b\rangle$ and $\delta\langle bc^\dagger v\rangle$. These correlations appear through the cluster expansions $\langle bc^\dagger v\rangle = \delta\langle bc^\dagger v\rangle + \langle b\rangle\langle c^\dagger v\rangle$ and $\langle b^\dagger b\rangle = \delta\langle b^\dagger b\rangle + \langle b^\dagger\rangle\langle b\rangle$ of terms in the Hamiltonian. Note that the equations for $\langle b^\dagger\rangle$, $\langle c^\dagger v\rangle$, $\langle b^\dagger v^\dagger c\rangle$ are the complex conjugated of the equation for $\langle b\rangle$, $\langle v^\dagger c\rangle$, $\langle bc^\dagger v\rangle$, so they are not explicitly

included in the model. The model equations are

$$\begin{aligned} d_t\langle c^\dagger c\rangle =& -(\gamma_{nl}+\gamma_{nr})\langle c^\dagger c\rangle + r(1-\langle c^\dagger c\rangle) \\ & - 2\mathfrak{Re}[g(\delta\langle bc^\dagger v\rangle + \langle b\rangle\langle c^\dagger v\rangle)], \end{aligned} \tag{5.1}$$

$$\begin{aligned} d_t\delta\langle bc^\dagger v\rangle =& -(\gamma_c+\gamma+i\Delta\nu)\delta\langle bc^\dagger v\rangle + g^*[\langle c^\dagger c\rangle \\ & + \delta\langle b^\dagger b\rangle(2\langle c^\dagger c\rangle - 1) - |\langle v^\dagger c\rangle|^2], \end{aligned} \tag{5.2}$$

$$d_t\delta\langle b^\dagger b\rangle = -2\gamma_c\delta\langle b^\dagger b\rangle + 2N\mathfrak{Re}(g\delta\langle bc^\dagger v\rangle), \tag{5.3}$$

$$d_t\langle b\rangle = -(\gamma_c+i\nu)\langle b\rangle + g^*N\langle v^\dagger c\rangle, \tag{5.4}$$

$$d_t\langle v^\dagger c\rangle = -(\gamma+i\nu_\varepsilon)\langle v^\dagger c\rangle + g[\langle b\rangle(2\langle c^\dagger c\rangle - 1)], \tag{5.5}$$

where r is the pump rate per emitter (the one for the whole system is Nr), with non resonant pump photons absorption and carrier transport effects approximated via an injection rate [15]. ν is the frequency of the resonant mode and ν_ε is the resonant frequency of emitters, $\Delta\nu = \nu_\varepsilon - \nu$ is the detuning between the field and emitter, g the light-matter coupling strength and N the number of emitters. The decay rates for the laser mode, γ_c, the population, γ_{nr}, and polarisation, γ, introduce dissipation. The dissipative part of these equations can be obtained by considering Lindblad terms describing the coupling to a Markovian bath [50,51]. γ_{nr} is due to non-radiative transitions, while the additional decay rate for the population, γ_{nl}, results from the adiabatic elimination of rapidly decaying non lasing modes [52]. The spontaneous emission factor, β, is related to the cavity losses by

$$\beta = \frac{\gamma_l}{\gamma_{nl}+\gamma_l}, \tag{5.6}$$

where γ_l is the rate of spontaneous emission into the lasing mode. γ_l is found from the system parameters

$$\gamma_l = \frac{2|g|^2}{\hbar(\gamma_c+\gamma)} \tag{5.7}$$

and its derivation is given in [31]. The expectation value of lower level population, $\langle v^\dagger v\rangle$ has been eliminated using $\langle c^\dagger c\rangle + \langle v^\dagger v\rangle = 1$. The variables $\langle b\rangle$ and $\langle v^\dagger c\rangle$ correspond to the amplitudes of the coherent field and the medium polarization of semi-classical mod-

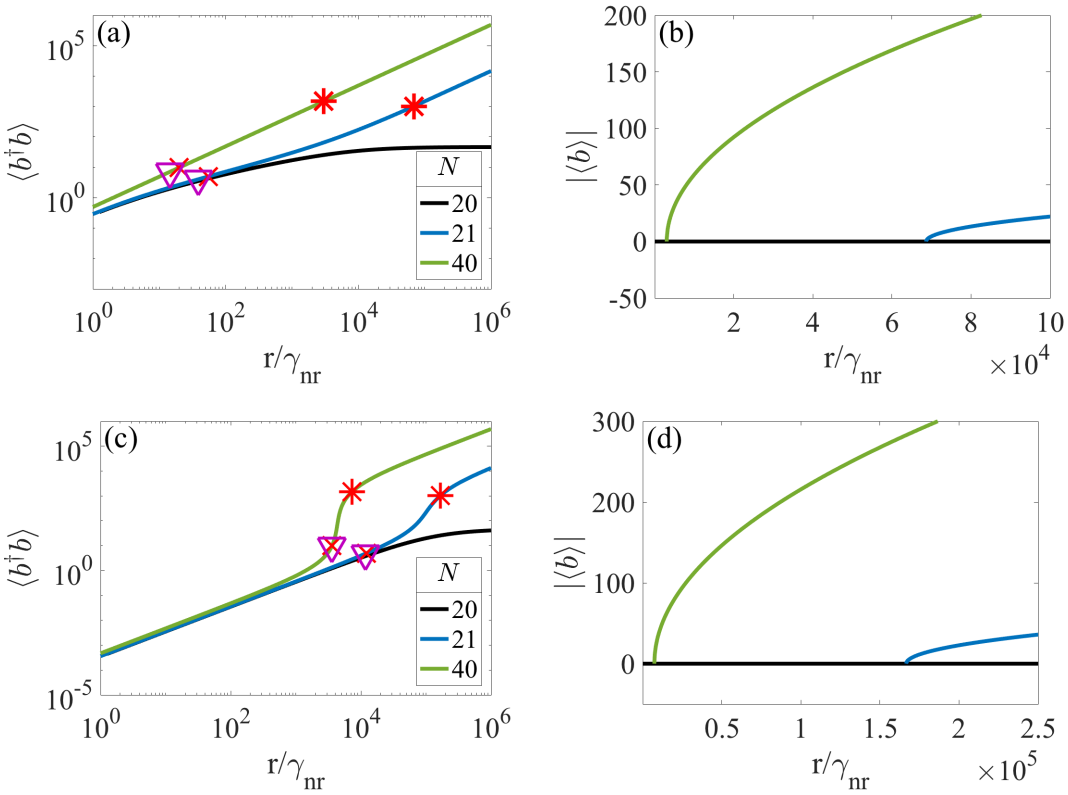

Figure 5.1: I/O curves: Intensity, $\langle b^\dagger b\rangle = \delta\langle b^\dagger b\rangle + \langle b^\dagger\rangle\langle b\rangle$, and coherent field amplitude for different N above and below N_c versus pump for $\beta = 1$ ($\gamma_{nl} = 0$), (a) and (b); and $\beta = 7 \times 10^{-4}$ ($\gamma_{nl} = 1.4 \times 10^{12} s^{-1}$ and $\gamma_l = 9.68 \times 10^8 s^{-1}$), (c) and (d). Laser and anti-bunching thresholds are marked by red stars and crosses, respectively. The purple triangles mark the anti-bunching threshold where we include higher order correlations (this shows our approximation to be valid). Note that a laser threshold is found even for a "thresholdless" device (green line in (a)). Parameters: $\gamma = 10^{13} s^{-1}$, $\gamma_c = 10^{10} s^{-1}$, $\gamma_{nr} = 10^9 s^{-1}$, and $g = 7 \times 10^{10} s^{-1}$. Losses are kept constant in all figures.

els of macroscopic lasers and were previously neglected in nanolasers. The imaginary coefficients in their the equations show that they have fast oscillations with frequency of the order of that of the cavity mode. Hence, we call them "fast" and the remaining variables "slow".

The non-lasing stationary state is found by setting to zero the fast variables and the time derivatives in Eqs.(5.1-5.3). This state exists for all values of the control parameters and its emission evolves continuously from thermal to anti-bunching. The boundary between these two regimes is identified by the curve $g^{(2)}(0) = 1$. We find a very good

analytical approximation of the $g^{(2)}(0) = 1$ curve assuming that the correlations used here are independent of higher order correlations [5], so that $g^{(2)}(0) \sim 2 + A/B$, see Appendix C. We determine the stability of the non-lasing state by deriving the equations that govern the evolution of small perturbations in the linear regime. We find that the perturbations of the fast variables are decoupled from the perturbations of the slow variables allowing us to determine analytically the stability of the non-lasing state. The non-lasing state is stable for $\langle c^\dagger c\rangle < \langle c^\dagger c\rangle_{th}$ and unstable for $\langle c^\dagger c\rangle > \langle c^\dagger c\rangle_{th}$ where

$$\langle c^\dagger c\rangle_{th} = \frac{1}{2} + \frac{\gamma_c\gamma}{2N|g|^2}\left[1 + \left(\frac{\Delta\nu}{\gamma_c+\gamma}\right)^2\right] \tag{5.8}$$

is the laser threshold. Because $\langle c^\dagger c\rangle < 1$, lasing can only happen when the number of emitters satisfies the condition

$$\frac{\gamma_c\gamma}{|g|^2}\left[1 + \left(\frac{\Delta\nu}{\gamma_c+\gamma}\right)^2\right] \leq N. \tag{5.9}$$

The laser frequency is determined using trial solutions $\langle b\rangle, \langle v^\dagger c\rangle \propto e^{-i\Omega}$ in Eqs.(5.4,5.5). The laser frequency is then the determined by finding the Ω that solves these equations and is

$$\Omega = \nu + \frac{\gamma_c\Delta\nu}{\gamma_c+\gamma}. \tag{5.10}$$

A few points are worth highlighting. Firstly, the laser frequency Ω is independent of the number of emitters, N. Secondly, the threshold can be calculated for any values of the decay rate γ_{nl}, including the so called "thresholdless" case $\gamma_{nl} = 0$. Third, neither $\langle c^\dagger c\rangle_{th}$ nor the critical number of emitters necessary to lase depend on β. However, the value of the pump per emitter required to reach $\langle c^\dagger c\rangle_{th}$ depends on β and decreases as β increases. The analytical solution for r is found by solving Eq. C.9 for the pump r at threshold, $|\langle b\rangle| = 0$, we get the following equation

$$r \geq \frac{(N|g|^2\Gamma_c^2 + \gamma\Delta_\Gamma)(2|g|^2\Gamma_c^2 + \Delta_\Gamma\Gamma_n)}{\Delta_\Gamma(N|g|^2\Gamma_c^2 - \gamma\Delta_\Gamma)} \tag{5.11}$$

where $\Gamma_c = \gamma + \gamma_c$, $\Delta_\Gamma = \gamma_c(\Gamma_c^2 + \Delta\nu^2)$, $\Gamma_n = \gamma_{nl} + \gamma_{nr}$, $\Gamma_t = 3\gamma_c + \gamma$ and $\Delta\Omega =$

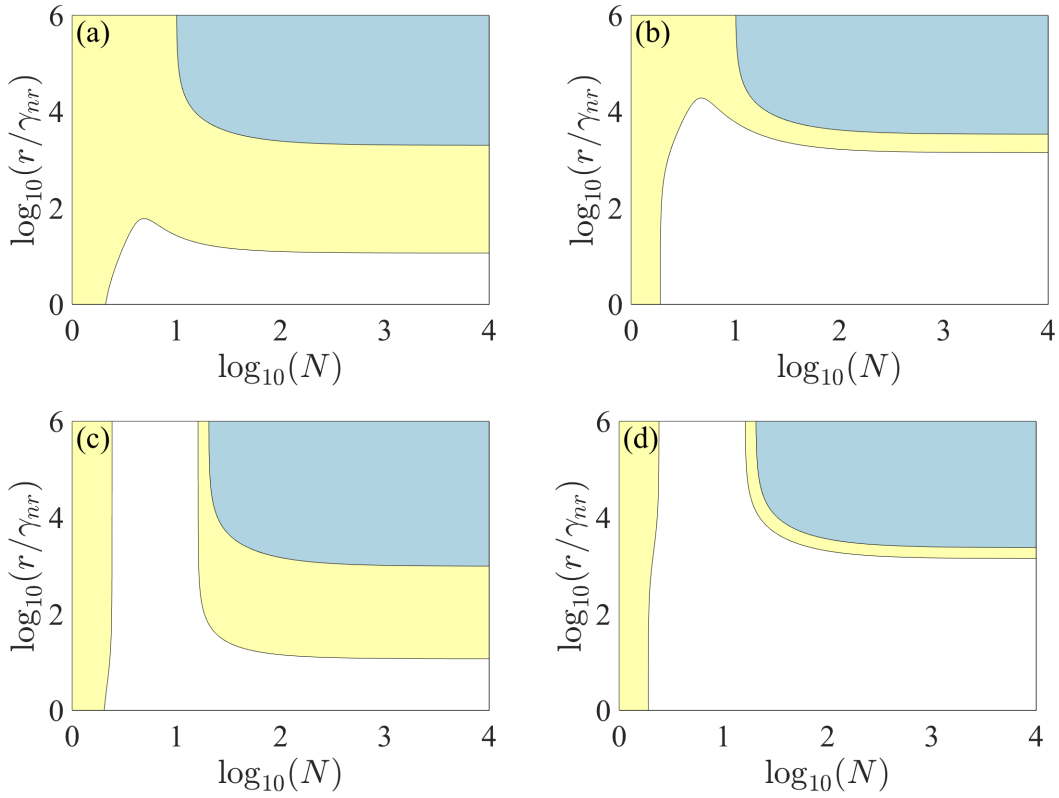

Figure 5.2: Phase Diagrams: thermal, anti-bunching and lasing regimes correspond to the white, yellow and blue regions, respectively. Where $\beta = 1$ and $g = 10^{11}s^{-1}$ in (a); $\beta = 7 \times 10^{-4}$ and $g = 10^{11}s^{-1}$ in (b); $\beta = 1$ and $g = 7 \times 10^{10}s^{-1}$ in (c); $\beta = 7 \times 10^{-4}$ and $g = 7 \times 10^{10}s^{-1}$ in (d). For large g the thermal region that extends to large pump values vanishes, and for a lasing a device with $\beta = 1$ the anti-bunching regime exists over greater values of the pump.

$\Delta\nu(1 - \frac{\gamma_c}{\Gamma_c})$. Imposing the physical conditions that r is positive and the denominator of Eq. 5.11 cannot be zero. When r is equal to the term on the right hand side in Eq. 5.11 marks the lasing threshold. We find the condition that satisfies the physical constraints of r to be the inequality

$$N > \frac{\gamma\Delta_\Gamma}{|g|^2\Gamma_c^2} \tag{5.12}$$

which is the same condition given in chapter 5 that states for a lasing threshold to exist there must be a critical number of emitters. If the condition in Eq. 5.12 is fulfilled then there is the solution for $|\langle b\rangle|$ and it grows in the shape of a pitchfork bifurcation.

In Fig. 5.1a and Fig. 5.1b the intensity and coherent field versus pump for a $\beta = 1$ device are shown. The different number of emitters correspond to values above (blue and olive curves) and below (black curves) the critical number, N_c, required for a laser using Eq.(7). Below N_c, the minimum integer that satisfies Eq.(5.9), the coherent field amplitude is always zero and the intensity saturates at high pump. Above N_c, $\langle b \rangle \neq 0$ emerges through a pitchfork bifurcation. The emergence of a pitchfork bifurcation also coincides with the growth of the intensity and a clear qualitative difference is apparent between the curves corresponding to lasing and non lasing devices. The I/O curve for 40 quantum dots (Fig. 5.1a) illustrates the impossible task of determining the laser threshold for a $\beta = 1$ device, identifiable only through the fast variables. Comparison of these thresholds with standard estimates is given in SM Fig. 4. Notice that all graphs plot pump for a single quantum dot. Thus, comparison between devices with different N requires multiplication of each horizontal scale by N. Variations in the I/O similar to those shown in Fig. 5.1a for $N = 21$ and $N = 40$ can be obtained with the same value of N and changing the detuning. This is observed in experiments where detuning decreases the effective number of quantum dots interacting with the field. See SM Fig. 6 for the effect of detuning. Experiments have obtained this kind of I/O response through cavity or thermal tuning [53–55]. While so far explained only through ad-hoc calculations, here the continuous transformation with change in characteristic I/O shape emerges thanks to self-consistent modeling.

Fig. 5.1c and Fig. 5.1d show the intensity and coherent field for a device where $\beta \ll 1$. One clear difference is that the intensity profile is no longer linear and there is the characteristic s-shaped I/O curve. Notable is the appearance of the bifurcation at the knee of the upper branch of the I/O curve, rather than at the inflection point (as from [23]). This points to a substantial contribution from the incoherent emission to the intensity growth before the bifurcation and highlights the difficulty intrinsic in determining threshold through the I/O curve.

Fig. 5.2 shows the analytic solutions of $g^{(2)}(0) = 1$ and the laser threshold as functions of the pump and N for different values of g and β. For a device capable of lasing there is a well defined path of emission as the pump increases (vertical cut in

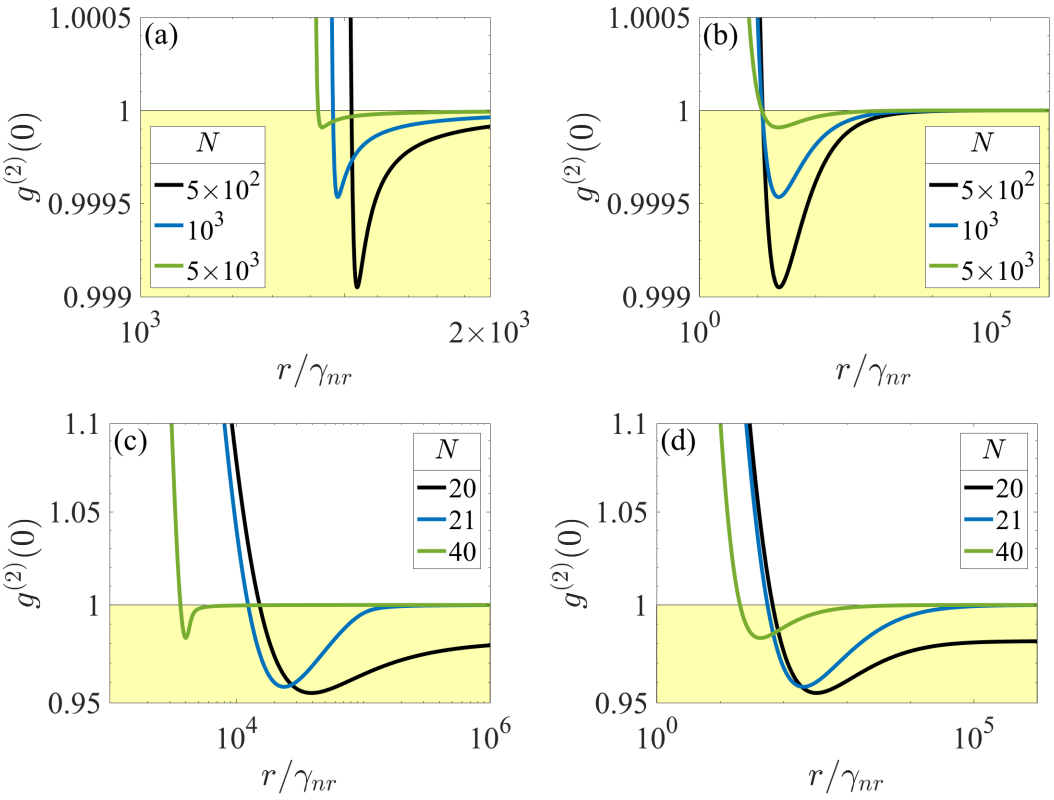

Figure 5.3: $g^{(2)}(0)$ versus pump for different N and β where the coloured regions correspond to the same in Fig. 5.2. In (a) and (c) $\beta = 7 \times 10^{-4}$; and in (b) and (d) $\beta = 1$. Note the large range of pump values in (a) and (b) where $g^{(2)}(0)$ is smaller, but very close to 1, making $g^{(2)}(0)$ difficult to use as an experimental indicator of lasing. All curves in (a) converge to the same value for larger pump values not shown. All curves are obtained for $g = 7 \times 10^{10} s^{-1}$ thus lasing occurs for $N = 21$.

the graph): from thermal to anti-bunching; then from anti-bunching to lasing. This is independent of the value of β. Fig. 5.2a and Fig. 5.2c show an anti-bunching regime that exists for a large region of the pump and extends from nano- to macroscopic lasers with $\beta = 1$. Anti-bunching has been observed in an experiment with a high cavity Q micropillar containing $N \approx 15$ pumped quantum dots [27] and in numerical simulations of quantum dot nanocavities [5], [56]. The observation is consistent with our prediction (Fig. 5.3), which shows stronger anti-bunching close to N_c; an increase in N reduces the range and amplitude, thus making an experimental observation much more difficult (no anti-bunching was in fact observed upon doubling of the quantum dot number [27]). Fig. 5.3a shows the three regimes for lasers with $\beta = 7 \times 10^{-4}$. Although anti-bunching is present in macroscopic lasers, $g^{(2)}(0)$ is so close to unity that it becomes very difficult to distinguish between a laser and a device emitting anti-bunched light, thus stressing that $g^{(2)}(0)$ is not a sufficient indicator of laser action. We show in Fig. 3 of the SM a comparison of Eqs. (1-5) with the master equation given in [23] and a cQED model [15].

In conclusion, we have derived a model that includes coherent and incoherent emission and derived analytically thresholds that separate thermal, anti-bunching and lasing emission regimes from single emitter to macroscopic devices. We predict the qualitative differences between the I/O curves of the photon number above and below threshold and find analytically the number of intracavity emitters necessary for laser action to occur. We identify a universal route leading from thermal to coherent emission, through a collective anti-bunching regime that always precedes lasing. The coherent laser field always emerges from a bifurcation with a well defined threshold and has a frequency independent from the number of emitters. Interferometric measurements of the coherence time [57, 58] ($g^{(1)}(\tau)$) – equivalent to detecting the existence of a well-defined frequency at the bifurcation – can in principle be used to unambiguously identify lasing in all devices. This also holds for $\beta = 1$ (or close to this boundary), where the I/O characteristics cannot carry useful information and measurements of $g^{(2)}(0)$ are poor indicators of lasing, leading to wrong conclusions on the existence or position of the laser threshold. The accurate characterization of the coherence properties of nanolasers holds promise for quantitative predictions to be used in a variety of applica-

tions, ranging from telecommunications and optical chips [59], to the spectroscopic use of nanosources [60], nanosensing [61] and biophysical applications [62]. These applications can greatly benefit from a detailed understanding and predictive power of designs where control in the number of quantum dots (now technologically feasible [43, 63]) coupled to effective coupling allow for tailored emission properties. In addition, at the micro and nano scale this new theory can be used to investigate the interaction of emitters with nanostructures and arrays of particles [64–68] and obtain predictions for new effects emerging from quantum interactions.

Chapter 6

Photon-number squeezing in nano- and microlasers

Mark Anthony Carroll derived the model equations, carried out their analytical analyses and wrote the code to produce the figures. Reproduced from [69], with the permission of AIP Publishing.

Based on the theoretical predictions in **Chapter 5** where antibunching was observed below the laser threshold at the nano- and microscale, we analyze the amount of photon number squeezing in the laser emission. Up to 3 dB photon number noise reduction is obtained in comparison with coherent emission, with output power in the range of pW and with negliable effects due to pump fluctuations. It is acknowledged that power in the nW range is of interest and whilst more output power is always welcomed, it should be noted that the photon number described here comes for 'free' and is an encouraging start into the investigation of non-classical emission described by the model outlined in **Chapter 5**. The scheme requires a moderately high Q cavity and holds promise for the construction of a simple and effective photon-number squeezed source.

A squeezed state of light involves a reduction of quantum noise in one quadrature below the standard quantum limit whilst preserving the minimum uncertainty product due to increased quantum noise in the other quadrature. In this chapter photon number squeezing, or amplitude squeezed light is discussed. Photon number squeezing occurs when the noise in the uncertainty of the photon number is reduced at the ex-

pense of enhancing the phase noise - as outlined above this is the trade-off between the two quadratures that ensures the minimum uncertainty product is preserved. Understanding squeezing is acutely important in applications that are noise-sensitive. Measurement systems are eventually limited in their performance by the presence of noise, whose reduction benefits metrology, quantum imaging, optical communications and measurements, gravitational wave detection, quantum information, etc. [10, 11, 70–72]. The strongest efforts to reduce photon number noise through light squeezing have been concentrated onto the single emitter regime, with a record fluctuation reduction of about 3 dB in single Quantum Dot resonance fluorescent emission [73].

Photon number squeezing was investigated early on [74, 75] for its relative ease of implementation and for its compatibility with a large photon flux. Numerous implementations, based on direct photon number squeezing [76] on pulsed nonlinear schemes with up to 10^{10} photons [77, 78], or superadiant effects [79, 80] have been predicted but they often produce only a low amount of squeezing (fraction of a dB). More recently, squeezing has been obtained from a set up based on cold atomic samples but at the cost of a complex realization [81].

Clustering of emitters or entangled photon ensembles represent another way of producing multiphoton squeezed states for sophisticated computing or cryptographic applications [82–84]. Polaritons in the strong coupling regimes have produced a good amount of squeezing and hold promise as sources of light for continuous variable quantum information encoding and cryptography [85]. Advanced nonlinear resonator concepts [86–88] now enable the realisation of interesting and flexible schemes which could find use in integrated devices. However, all previous schemes require rather complex experimental setups and recently interest is developing for sources where intensity noise can be reduced with simpler schemes [89,90] (and references therein). The device which we propose provides below-threshold squeezing and is based on a nanostructure. Thus, in spite of an output power lower than what has been previously obtained, it offers several advantages: small footprint and thermal load, thus enabling on-chip integration; avoidance of multimode anticorrelations which, while providing squeezed light [91], render the photon stream not usable for numerous applications [92]; avoidance of feed-

back schemes [93–95] and of cooling requirements [96, 97]. The intrinsic integrability of the proposed source into optical chips offsets its intrinsic low photon flux, since virtually all photons can be used in a guided structure. In addition, giant nonlinearities emerging in nanostructures [98], metamaterials [99], plasmonics [100] and quantum interference [101] hold strong promise for the exploitation of weak signals in integrated structures.

In line with these developments, the recent quantum-dot based Coherent-Incoherent model (CIM), where the coherent and incoherent field components are independently described [3], predicts from first principles the existence of a pre-threshold regime where photon antibunching, thus squeezing [102], is naturally observed.The CIM model has been derived under the experimentally verified conditions [103] that the decay rate of the material polarization is much larger than that of the photons in the cavity. In this case it is well known [34] that the emitters are independent from each other and that correlations between emitters are negligible even close to laser threshold. The pump range in which antibunching appears is broad enough to promise experimental accessibility and the resulting degree of squeezing sizeable enough to warrant consideration. Antibunching has been experimentally observed and modeled [27] for a low number of emitters. In this letter we predict that squeezing with large photon number occurs at extremely low power supply for nano and micro laser with emitter numbers up to 10^3 in the anti-bunching region [3]. The advantage of this prediction is that the photon antibunched behaviour appears to naturally precede lasing, in a cw regime of operation, without the need for any special experimental arrangements and promises to provide photon fluxes comparable or larger than those of more complex, pulsed techniques.

In order to introduce the ideas, we generalize the relationship between average and variance in a Poisson process by introducing a sub-Poissonian coefficient a:

$$\langle \Delta n^2 \rangle \quad = \quad a \langle n \rangle \,, \tag{6.1}$$

with n photon number, $\langle\rangle$ temporal average and $\langle \Delta n^2 \rangle$ corresponding to the variance, where a subpossonian statistics, i.e. squeezed emission, emerges for $a < 1$. In order

to connect squeezing to antibunching we introduce this modified distribution into the definition of the zero-dealy second-order autocorrelation function

$$g^{(2)}(0) \quad = \quad \frac{\langle n^2 \rangle - \langle n \rangle}{\langle n \rangle^2} = 1 - \frac{1-a}{\langle n \rangle}\,. \tag{6.2}$$

Photons are antibunched when $g^{(2)}(0) < 1$, so that $g^{(2)}(0)$ is a standard measure of the degree of antibunching. Solving equation (6.2) for a, we notice that it linearly depends on the average photon number $\langle n \rangle$. As the photon number grows, the apparent degree of antibunching is reduced for a same reduction in the relative fluctuation eq. (6.1) as illustrated in Fig. 6.1. Thus, even though the antibunching may appear to be small, it is possible to maintain a good amount of photon number noise reduction, thus squeezing since $g^{(2)}(0) < 1$ (see Refs. [104–106] and references therein), in the photon number for macroscopic signals. These qualitative considerations point to a potential interest even in a moderate amount of antibunching emerging from the model [3].

The main interest of the scheme is its intrinsic simplicity and the potential for effective photon number squeezing with considerable large photon numbers. The fact that a below-threshold nanolaser may spontaneously emit photon streams in a more ordered fashion than an equivalent coherent source [107] hints to potential interest for a variety of applications. Indeed, in this configuration there is no need to destroy phase coherence to reduce photon number noise, contrary to what is required of above-threshold lasers.

We test the idea by using a quantum model [3], derived using the cluster expansion technique [33, 47], that includes both coherent and incoherent field components; previous cluster expansion based models neglect the expectation values of the coherent variables [5, 15, 31].Its key feature resides in the univocal determination of a lasing threshold irrespective of cavity characteristics (even for $\beta = 1$, the fraction of spontaneous emission coupled into the lasing mode), thus establishing a clear boundary between the squeezed and coherent emission regime. The medium is assumed to be an ensemble of identical but independent two-level emitters coupled with a single cavity lasing mode. We remember that the rapid polarisation dephasing permits one to omit inter-emitter correlations [31, 34]. The incoherent dynamical variables are the popula-

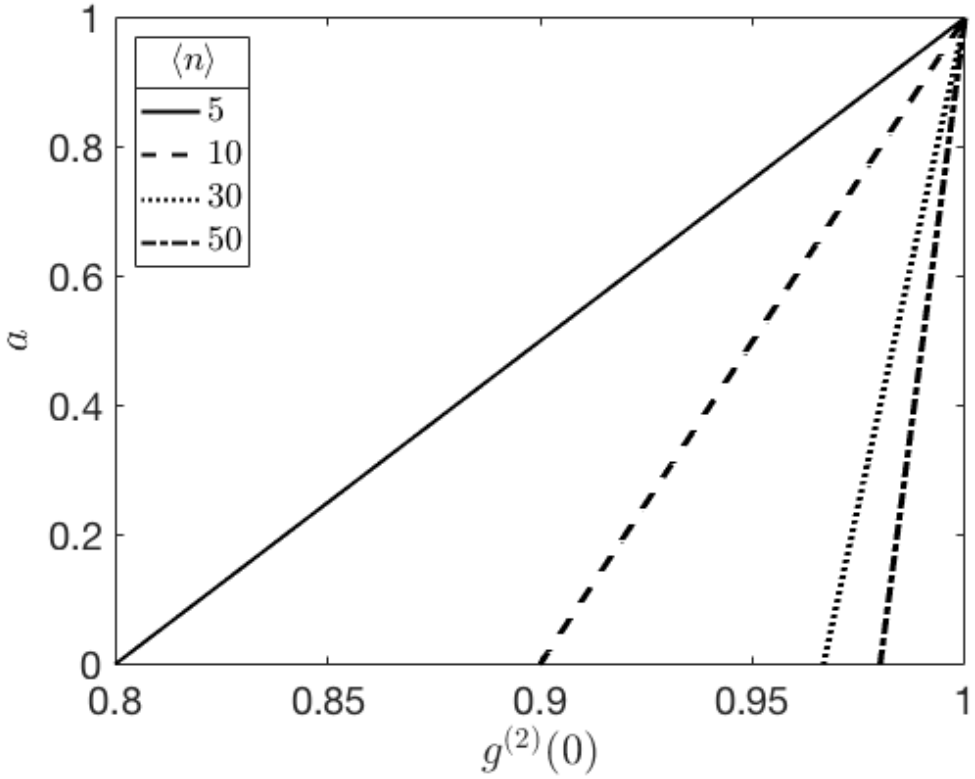

Figure 6.1: Subpoissonian coefficient a (defined in eq. (6.1)) as a function of the value of $g^{(2)}(0)$ for different values of the average photon number $\langle n \rangle$.

Parameter	Value	Description
g	$7{\times}10^{10}s^{-1}$	Light-matter coupling strength
γ_c	$7 \times 10^{9}s^{-1}$	Cavity decay rate
γ	$10^{13}s^{-1}$	Dephasing rate of active medium
γ_{nr}	$10^{9}s^{-1}$	nonradiative decay rate
γ_{nl}	$1.4 \times 10^{12}s^{-1}$	Decay rate into the nonlasing modes
β	7×10^{-4}	Spontaneous emission factor

Table 6.1: Parameters that appear in the model used to compute $g^{(2)}(0)$, equation (6.3). The values in this table are used in all figures unless stated otherwise.

tion density of the excited state, $\langle c^\dagger c\rangle$; the photon assisted polarisation of the medium, $\delta\langle bc^\dagger v\rangle$; and the number of photons, $\delta\langle b^\dagger b\rangle$. These are coupled to the coherent variables, i.e. the electric field amplitude $\langle b\rangle$ and the classical polarisation $\langle v^\dagger c\rangle$.

The lasing threshold exists only if the total number N of emitters in the cavity is larger than a critical value N_c. If this condition is fulfilled, then at sufficiently large pump values a stable coherent field begins to grow inside the cavity. This has also been confirmed in a standard rate equation model that includes stochastic noise terms [1] as well as experimentally [15].

Using this model we have computed the intra-cavity value of

$$g^{(2)}(0) = \frac{\langle b^\dagger b^\dagger bb\rangle}{\langle b^\dagger b\rangle^2} \tag{6.3}$$

expressed in terms of field creation and destruction operators, as a function of the model parameters summarised in table 6.1. The important parameters that control and characterise squeezing are the pump parameter per emitter, r, the number of emitters, N, the cavity decay rate, γ_c and the light-matter coupling strength, g. The remaining system parameters are the decay rate of the medium, γ; the non-radiative decay rate, γ_{nr}; and the decay rate into non-lasing modes, γ_{nl}. The latter controls β, where the ultimate limit of $\beta = 1$ corresponds to $\gamma_{nl} = 0$.

From here on, we concentrate on parameter values which match a microlaser, simply because we aim at obtaining macroscopic amounts of output power. The findings, however, generally hold for all devices down to the extreme nanoscale, with features

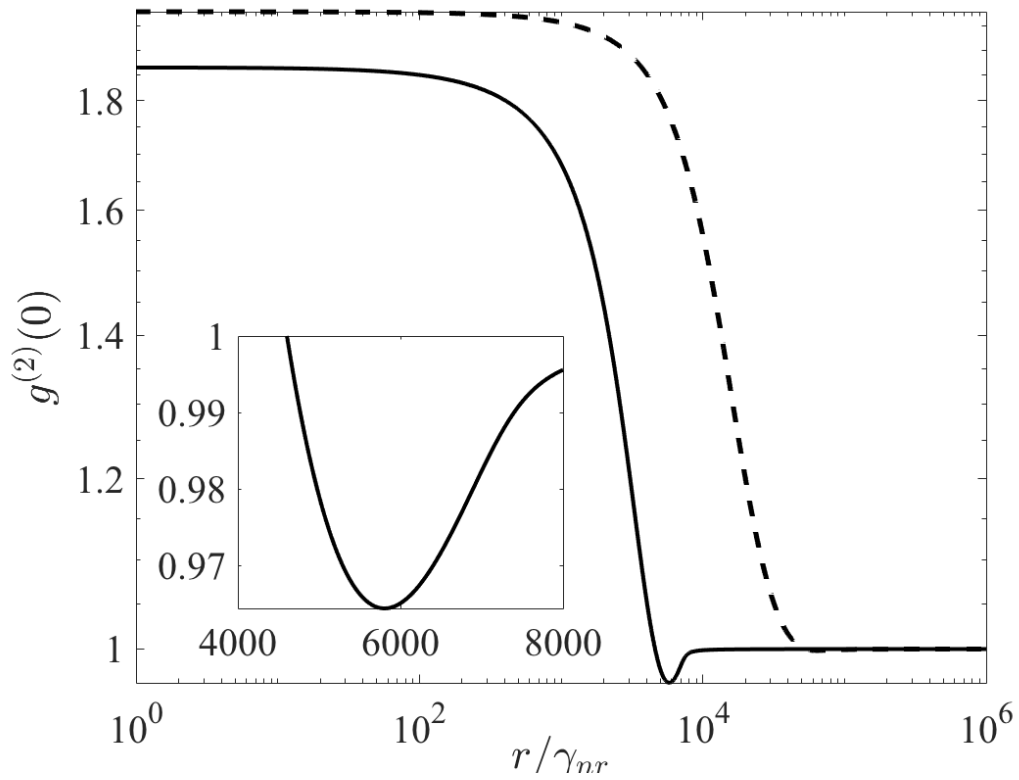

Figure 6.2: The intensity autocorrelation function versus pump r for different paired values of the cavity losses γ_c and number of emitters N above the critical number N_c required for lasing. In order to meet the condition for lasing, as the cavity losses increase so to must the number of emitters, therefore $N = \{21, 150\}$ and $\gamma_c = \{7 \times 10^9 \mathrm{s}^{-1}, 7 \times 10^{10} \mathrm{s}^{-1}\}$ for the solid and dashed curves respectively. simulations were performed on

which only change quantitatively. In Fig. 6.2 we plot the steady state values of $g^{(2)}(0)$ as a function of the pump for two different lasing devices. As the pump increases the two photon statistics (depending on the device) enter three different regimes: from super-Poissonian (thermal light) to sub-Poissonian (squeezed light), and, then, to Poissonian (coherent light) – in the good cavity limit ($\gamma_c < g$, solid line); when cavity losses are equal to the coupling strength (dashed line) the antibunching becomes negligibly small and disappears entirely in the bad cavity regime ($\gamma_c > g$, not plotted). The anti-bunching region shows a sensitive dependence on the number of emitters as there is only a small window of pump values for which squeezing can occur and this becomes narrower as the number of intra-cavity emitters increases [3]. As we later show, this constraint does not strongly affect the scheme's implementability.

Concentrating on $\gamma_c < g$, we remark that while squeezing is possible with a very small number of emitters, provided the coupling g is sufficiently strong, a substantial amount of power is obtained only from devices which are capable of passing the laser threshold [3], i.e. with $N > N_c$. We thus concentrate on this regime keeping the remaining values of table 6.1 fixed, as their influence on the final result is only minor.

To estimate the photon number noise reduction we directly compute the relative fluctuation of the photon number,

$$\frac{\langle \Delta n \rangle}{\langle n \rangle} = \frac{\sqrt{\langle b^\dagger b b^\dagger b \rangle - \langle b^\dagger b \rangle^2}}{\langle b^\dagger b \rangle}. \tag{6.4}$$

which can be transformed into an expression containing $g^{(2)}(0)$ by the normal-ordering [47] of $\langle b^\dagger b b^\dagger b \rangle$:

$$\langle b^\dagger b b^\dagger b \rangle = \langle b^\dagger b \rangle + \langle b^\dagger b^\dagger b b \rangle, \tag{6.5}$$

where Eq.(6.5) follows from standard application of Bosonic commutation relation. Now, substituting the equation for $g^{(2)}(0)$

$$g^{(2)}(0) = \frac{\langle b^\dagger b^\dagger b b \rangle}{\langle b^\dagger b \rangle^2} \tag{6.6}$$

into Eq.(6.4) we arrive at

$$\frac{\langle \Delta n \rangle}{\langle n \rangle} = \sqrt{\langle b^\dagger b \rangle^{-1} + g^{(2)}(0) - 1}. \tag{6.7}$$

As expected, noise reduction appears for $g^{(2)}(0) < 1$. It is also important to note that as N increases $g^{(2)}(0)$ approaches 1 and we recover the relative fluctuations of the classical limit, i.e. $1/\sqrt{n}$.

However, the presence of antibunching ensures a more regular temporal distribution of photons than the random occurrences of coherent emission [107], thus squeezing, which we quantify by defining an attenuation coefficient

$$A_{\mathrm{dB}} = 20 \log_{10} \left(\frac{\langle \Delta n \rangle}{\langle n \rangle} \right), \tag{6.8}$$

and comparing its value [108] to the one which characterizes coherent emission ($g^{(2)}(0) = 1$).

We first consider the case of an ideal pump with no fluctuations and evaluate the attenuation at the minimum of $g^{(2)}(0)$, i.e., where squeezing is greatest. Fig. 6.3 compares the noise attenuation as a function of the emitter number (black circles) to the reference coherent field emission (red circles) obtained by imposing $g^{(2)}(0) = 1$ in eq. (6.7). The inset shows the difference between the two. The best squeezing, -3 dB, for $N = 13$, just below the critical number of emitters required for lasing, $N = 15$, for the parameters used in Fig. 6.3. We see that even with 100 emitters there is still approximately 1.5 dB of squeezing. This is obtained with standard laser parameter values. With some technological efforts in the realization of dedicated devices and some optimization better results can be obtained.

The case just considered neglects pump fluctuations. However, incorporating them is of vital importance if we are to understand the viability of potential devices. Pump stabilization has been one of the first means of obtaining squeezing [109, 110] and technology is capable of achieving stability values well below 1% for the currents needed to pump a small device. We therefore consider a maximum amplitude fluctuation in the pump by $\pm 1\%$ and observe its influence on the photon number noise reduction.

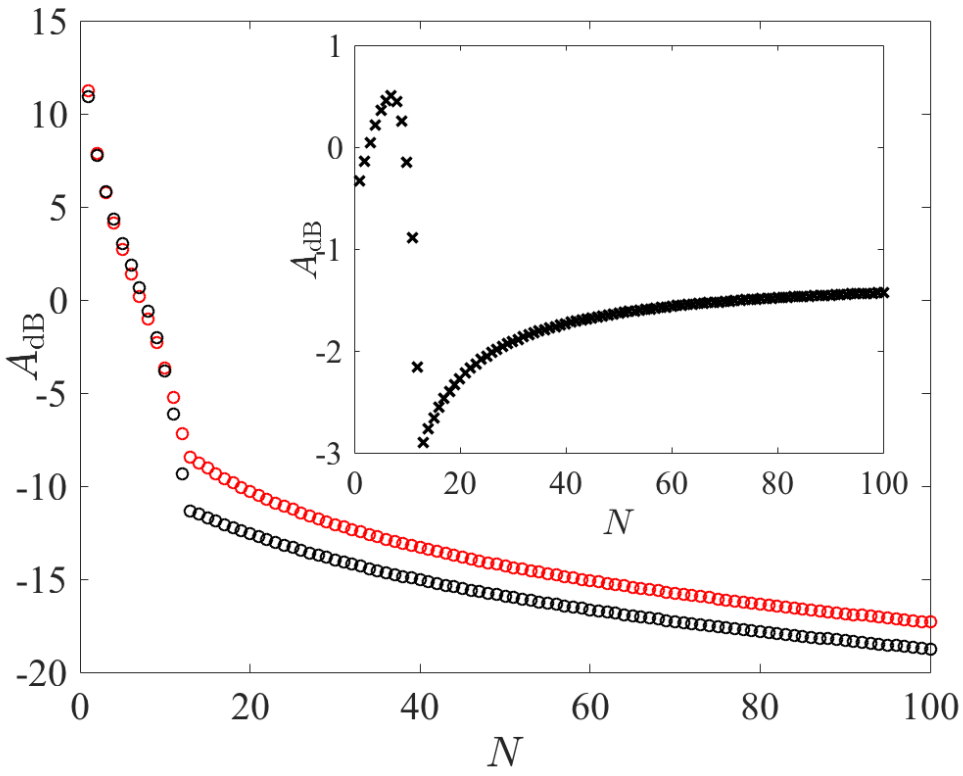

Figure 6.3: Squeezing as a function of N. The black curve is obtained from equation (6) at the minimum of $g^{(2)}(0)$ calculated from the CIM, whereas the red curve shows squeezing for a coherent field. The inset shows how much squeezing is gained compared to a coherent field with the same photon number.

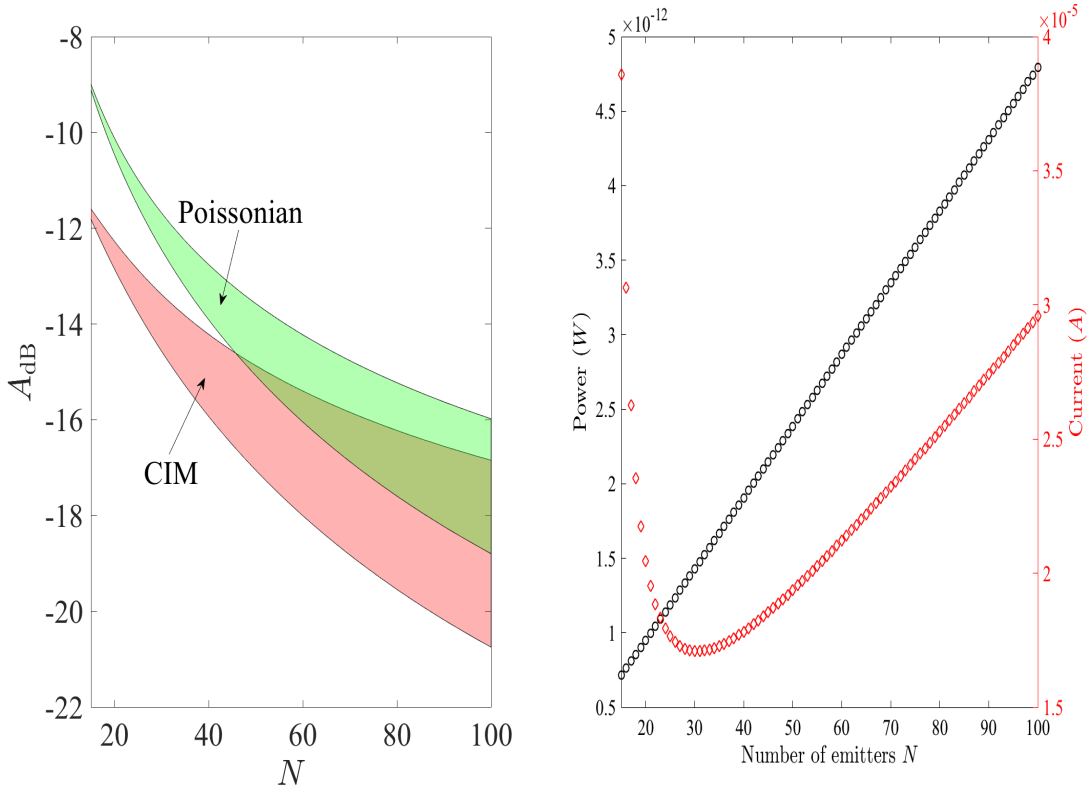

Figure 6.4: Left panel: Spread in squeezing of the antibunching and coherent sources in Fig. 6.3 due to $\pm 1\%$ fluctuations in the pump as a function of N (taken above N_c). Right panel: Output power (black) and pump current (red) as a function of $N > N_c$. All points are evaluated at the minimum of $g^{(2)}(0)$. The driving current is calculated as follows: $r_{min}\gamma_{nr}Ne$, where r_{min} is the value of the pump at the minimum of the $g^{(2)}(0)$ curve and e is the electron charge.

Fig. 6.4 shows the absolute noise reduction (as in the main panel of Fig. 6.3) for the below-threshold laser (orange shaded area) and for a coherent signal (green shaded area). The lower curve delimiting the region corresponds, for both cases, to a positive 1% fluctuation – enhancing the amount of power – while the upper one represents the boundary set by a negative 1% fluctuation. In either case, the spread increases from something extremely small at when the number of emitters is at the minimum value, $N = 15$, to a sizeable fluctuation for $N = 100$. The fact that the antibunched curves lie below the coherent ones signal the fact that a large part of the contribution to the fluctuation originates from the change in photon number, rather than in a modification in the amount of antibunching (cf. inset in Fig. 6.3). Only the differentially larger growth of the fluctuation in the below-threshold laser (upper bound of the fluctuation, corresponding to the steeper part of the antibunching curve – inset of Fig. 6.3) is to be attributed to come to a change in the amount of antibunching. Since we have considered a rather large pump fluctuation, compared to what is technologically feasible, and the laser injection current can be controlled to a much better degree, it is reasonable to consider the influence of pump noise negligible.

The right panel of Fig. 6.4 displays the absolute amount of current needed to pump the laser at the optimum antibunching value as a function of the emitter number. The injected current is is, at $N = 15$, about 40 μA (red symbols) and, as already mentioned, can be easily stabilized to better than 1%. The accompanying outcoupled output power (black circles – computed on the basis of the intracavity photon number, cavity losses and photon energy at $\lambda = 1$ μm) is about 0.7 pW (i.e., $\approx 10^7$ photons) around the intracavity -3dB squeezing level, and grows to ≈ 5 pW for 100 emitters (and ≈ 1.5 dB squeezing). Given that better pump stabilization is achievable, we have checked the results with pump fluctuations of the order of 0.1%. The stability is greatly improved and the output power can grow to 50 pW with 1000 emitters with ≈ 1.25 dB squeezing still gained compared to a coherent source .

It is important to remark that the conditions we have examined here correspond to a "good cavity" device ($Q \approx 2 \times 10^4$, following the definition of Ref. 48), as observed in Ref. 39 with a number of quantum dots consistent with the numbers used in this work.

Larger photon fluxes can be obtained by increasing the cavity losses (thus decreasing Q) provided the coupling factor g is correspondingly increased. Since we have used a standard value for g, routinely achieved in technological realizations, there is some margin for improvement there. It is likely that a careful choice of parameters and technological efforts may improve by one order of magnitude the power expected at the output of the device.

In summary, a recent model, which treats the incoherent and coherent parts of the field for lasers to describe the emission of Quantum-Dot based small-scale (nano- and micro-) lasers, predicts the appearance of photon emission with antibunched statistics before the lasing threshold [3]. Following the lead that this more regular photon emission produces reduced fluctuations, we have analyzed its properties with realistic physical construction parameters of a microlaser in the intent of obtaining a macroscopic output. The model predicts up to 3 dB photon-number squeezing with little influence of pump fluctuations, compared to the noise floor of an equivalent coherent field and output power approximately 0.7 pW. The squeezing is naturally produced by the physical interaction, without the need for any external action, since – contrary to standard squeezing of coherent output – below threshold there is no macroscopic phase to be degraded. It is important to note that the calculations and simulations performed in this chapter are limited in scope with respect to only considering the noise inside the cavity. As a result, developments of this investigation include its extension to nanolasers to explore the exploitation of the same phenomenon at low photon numbers as well as work to include mode partition noise on the output coupler [111] which is fundamental to understand the models true utility applied to real applications.

Chapter 7

Multi-electron model

We extend on a previously derived microscopic model, where the system comprises of more than one electron [5, 31], to include the coherent field and standard polarisation. The changes with respect to Eqs. (5.1)-(5.5) are: $\langle c^\dagger c\rangle$ is replaced by $\langle c^\dagger c\rangle^2$ in Eq. (5.2) and $-\gamma_{nl}\langle c^\dagger c\rangle$ is replaced by $-\gamma_{nl}\langle c^\dagger c\rangle^2$ in Eq. (5.1). These changes take place at the level of the cluster expansion and are a byproduct of the non-vanishing operator expectation value $\langle c_l^\dagger v_n^\dagger c_n v_l\rangle$ which is also the source term of spontaneous emission. In the case of the single electron system, two annihilation operators applied to the same state yield zero. Subsequently, we get

$$\frac{d}{dt}\langle b\rangle = -(\gamma_c + i\nu)\langle b\rangle + Ng^*\langle v^\dagger c\rangle \tag{7.1a}$$

$$d_t\langle c^\dagger v\rangle = -(\gamma - i\nu_\epsilon)\langle c^\dagger v\rangle + g^*\langle b^\dagger\rangle(2\langle c^\dagger c\rangle - 1) \tag{7.1b}$$

$$\begin{aligned}\frac{d}{dt}\langle c^\dagger c\rangle &= r(1-\langle c^\dagger c\rangle) - \gamma_{nl}\langle c^\dagger c\rangle^2 - \gamma_{nr}\langle c^\dagger c\rangle \\ &\quad - 2\Re g(\delta\langle bc^\dagger v\rangle + \langle b\rangle\langle v^\dagger c\rangle)\end{aligned} \tag{7.1c}$$

$$\begin{aligned}\frac{d}{dt}\delta\langle bc^\dagger v\rangle &= -(\gamma_c + \gamma - i\Delta\nu)\delta\langle bc^\dagger v\rangle + g^*\Big[\langle c^\dagger c\rangle^2 \\ &\quad + \delta\langle b^\dagger b\rangle(2\langle c^\dagger c\rangle - 1) - |\langle c^\dagger v\rangle|^2\Big]\end{aligned} \tag{7.1d}$$

$$\frac{d}{dt}\delta\langle b^\dagger b\rangle = -2\gamma_c\delta\langle b^\dagger b\rangle + 2N\Re g\delta\langle bc^\dagger v\rangle \tag{7.1e}$$

where the afore mentioned nonlinear terms are now included.

The two sets of equations constitute the single-electron CNQED, Eqs. (5.1)-(5.5),

and the multi-electron CNQED, equations (7.1a-7.1e), models.

7.1 Linear Stability Analysis

It is well known that a non-zero coherent field is one of the criteria required to identify laser emission, therefore, a non-lasing device will have zero coherent field amplitude. The single electron CNQED and multi electron CNQED models are therefore ideal to investigate the stability properties of the zero solution of the variables associated with laser emission, namely the coherent field amplitude and standard polarisation. Their zero solutions will be stable if the device is not capable of laser action. Using linear stability analysis (LSA) we study the dynamics of small perturbations around the zero solution of $\langle b \rangle$ and $\langle v^\dagger c \rangle$ for both models. If the perturbation grows then the fixed point is unstable and if it decays asymptotically then the fixed point is a stable one. The bifurcation point where this solution becomes unstable is the laser threshold and its existence is the condition for the device to be able to lase.

We see that the imaginary coefficients of the coherent field amplitude $\langle b \rangle$ and the standard polarisation $\langle v^\dagger c \rangle$ are of the order of the frequency of the cavity field mode and therefore oscillate rapidly with respect to the other dynamical variables. Thus, we call the variables associated with coherence "fast" and the remaining incoherent variables "slow". We group the coherent and incoherent variables in two groups, $\boldsymbol{c} = \{\langle b \rangle, \langle b^\dagger \rangle, \langle v^\dagger c \rangle, \langle c^\dagger v \rangle\}$ and $\boldsymbol{i} = \{\langle c^\dagger c \rangle, \delta\langle b^\dagger b \rangle, \delta\langle b c^\dagger v \rangle, \delta\langle b^\dagger v^\dagger c \rangle\}$, respectively and write the two CNQED models, Eqs. (5.1)-(5.5) and Eqs. (7.1a-7.1e), more compactly as

$$\frac{d\boldsymbol{i}}{dt} = \boldsymbol{F}(\boldsymbol{i}, \boldsymbol{c}), \tag{7.2}$$

$$\frac{d\boldsymbol{c}}{dt} = \boldsymbol{G}(\boldsymbol{i}, \boldsymbol{c}), \tag{7.3}$$

where $\boldsymbol{G}(\boldsymbol{i}, \boldsymbol{c})$ and $\boldsymbol{F}(\boldsymbol{i}, \boldsymbol{c})$ are non-linear vector functions of $\boldsymbol{i}$ and $\boldsymbol{c}$ whose components are the right-hand side of both models studied. For instance, $G_{\langle b \rangle}(\boldsymbol{i}, \boldsymbol{c})$ and $G_{\langle v^\dagger c \rangle}(\boldsymbol{i}, \boldsymbol{c})$ are the right-hand sides of the equations evaluated at the solution $\boldsymbol{i}, \boldsymbol{c}$. The linear

dynamics of small perturbations $\boldsymbol{\eta}_i, \boldsymbol{\eta}_c$ of a fixed point solution $\boldsymbol{i}, \boldsymbol{c}$ is given by

$$\frac{d}{dt}\begin{bmatrix} \eta_i \\ \eta_c \end{bmatrix} = \begin{bmatrix} \boldsymbol{\nabla}_{\mathbf{i}} \otimes \mathbf{F}(\mathbf{i},\mathbf{c}) & \boldsymbol{\nabla}_{\mathbf{c}} \otimes \mathbf{F}(\mathbf{i},\mathbf{c}) \\ \boldsymbol{\nabla}_{\mathbf{i}} \otimes \mathbf{G}(\mathbf{i},\mathbf{c}) & \boldsymbol{\nabla}_{\mathbf{c}} \otimes \mathbf{G}(\mathbf{i},\mathbf{c}) \end{bmatrix} \begin{bmatrix} \eta_i \\ \eta_c \end{bmatrix}. \tag{7.4}$$

Each block in the matrix on the right-hand side of Eq. (7.4) is of dimension 4×4 and is the Jacobian with respect to the $\mathbf{i}$ and $\mathbf{c}$ variables; $\otimes$ denotes the outer product between the column vector of the derivative operators and the row vector of the nonlinear vector functions. For any solution with $\boldsymbol{c} = 0$ one has $\boldsymbol{\nabla_i} \otimes \boldsymbol{G}(\boldsymbol{i}, 0) = 0$, so that the perturbation of the coherent variables decouple and their dynamics is given by

$$\frac{d}{dt}\boldsymbol{\eta}_c = \boldsymbol{\nabla_c} \otimes \boldsymbol{G}(\boldsymbol{i}, \mathbf{0})\boldsymbol{\eta}_c = \begin{bmatrix} J & 0 \\ 0 & J^\dagger \end{bmatrix} \boldsymbol{\eta}_c, \tag{7.5}$$

where

$$\begin{aligned} J &= \begin{bmatrix} \partial_{\langle b \rangle} G_{\langle b \rangle}(\mathbf{i},0) & \partial_{\langle v^\dagger c \rangle} G_{\langle b \rangle}(\mathbf{i},0) \\ \partial_{\langle b \rangle} G_{\langle v^\dagger c \rangle}(\mathbf{i},0) & \partial_{\langle v^\dagger c \rangle} G_{\langle v^\dagger c \rangle}(\mathbf{i},0) \end{bmatrix} \\ &= \begin{bmatrix} -\gamma_c & g^* N \\ g(2\langle c^\dagger c \rangle - 1) & -(\gamma + i\Delta\nu) \end{bmatrix}. \end{aligned} \tag{7.6}$$

This matrix depends on the system parameters and the excited state population. It is important to note that the structure the stability matrix is the same for both single and multi electron CNQED models, however, since J depends on the excited state population the eigenvalues are different.

In order to investigate the stability of the fast variables zero solution we look for the condition that satisfies $\mathrm{Re}(\lambda) > 0$. Noting that the physical range of the excited state population is $0 \leq \langle c^\dagger c \rangle \leq 1$ and substituting for $\langle c^\dagger c \rangle = 1$ we find that the condition for an instability to exist is

$$N > \frac{\gamma\gamma_c}{|g|^2}\Big[1 + \Big(\frac{\Delta\nu}{\gamma + \gamma_c}\Big)^2\Big]. \tag{7.7}$$

For an instability to exist the number of quantum dots must be greater than the critical

number given by Eq.(7.7). This critical number is independent from the spontaneous emission factor, β, and applies to both the CIM and multilevel model. Physically this means that the minimum number of quantum dots needed for lasing with the losses and detuning. Although the condition for an instability to exist is independent of the pump, this does not mean that a device will automatically operate as a laser if N is above the critical number; one must make also sure that sufficient pump power is provided so that the laser threshold is surpassed, as we will see in the following discussion.

7.2 Discussion of results

Armed with the knowledge of where the instabilities exist we now investigate how the dynamics of the systems are affected below and above the instability threshold. The cluster expansion of $\langle b^\dagger b\rangle$ results in a sum of two terms; the fluctuating part and the modulus squared of the coherent field amplitude, i.e., $\langle b^\dagger b\rangle = \delta\langle b^\dagger b\rangle + \langle b^\dagger\rangle\langle b\rangle$. Since $\langle b\rangle = 0$ when the device is not operating as a laser, at the level of the cluster expansion the photon number is given exclusively by the fluctuating part of the expansion. Fig. 7.1 illustrates the affect of including the fast variables, which have been neglected historically, for the CIM and the multilevel model presented in the previous section. For an instability to exist for the parameter considered here, $N > 20$. Below the critical number, as the pump increases the photon number saturates and the coherent field amplitude remains zero, confirming the absence of laser emission. For a number of quantum dots just above the minimum number for lasing, i.e. 21, there is a clear jump in photon number accompanied by an emerging non-zero coherent field amplitude, i.e. a pitchfork bifurcation. Since the photon number is given by

$$\langle b^\dagger b\rangle = \delta\langle b^\dagger b\rangle + |\langle b^\dagger\rangle|^2 \tag{7.8}$$

we can see from Fig. 7.1 that the initial growth in photon number is due to incoherent emission. The device containing double the number of quantum dots required for an instability to exist (red curve) passes the laser threshold before the device with fewer quantum dots. Its I-O curve also has a more pronounced s-shape displaying a

steeper transition from lower to upper branch. This does not make it easier to identify the laser threshold as the bifurcation occurs far from the inflection point here. It becomes apparent as N increases that the differences between the models begin to show. The multilevel model reaches threshold for lower values of the pump and as a result the fraction of incoherent emission making up the initial growth in photon number is reduced. Although the photon number diverges between the models as N increases, the critical number of emitters needed for an instability to exist does not change; only the pump power required to excite the instability changes.

These results highlight the need for the fast variables that describe the coherent processes of the laser. The position of the laser bifurcation with respect to the I-O curves show that it is not sufficient to simply visually inspect I-O curves as this will lead to the incorrect identification of the lasing threshold. Without the coherent variables it would be impossible to accurately locate the laser threshold and comment on the composition of the photon stream leaving the cavity.

7.3 Threshold dependence on detuning

From the LSA, we find that Eq. (7.7) can be recast in terms of $\Delta\nu$ and that the instability only exists if the following condition imposed on the detuning is met

$$\Delta\nu < (\gamma_c + \gamma)\sqrt{\frac{N|g^2|}{\gamma\gamma_c} - 1}. \tag{7.9}$$

This condition states that there is an upper bound to how far the detuning of a lasing device can be pushed before the coherent field becomes zero. Forcing $\Delta\nu$ to be real yields the following condition

$$N \geq \frac{\gamma\gamma_c}{|g|^2} \tag{7.10}$$

which is the stability condition at resonance for the critical number of emitters needed to lase. Fig. 7.2 illustrates the two regions, deliminated by equation (7.9), where the lower and upper regions correspond to the regimes where the coherent field is non-zero and zero, respectively. As this condition comes directly from the LSA it is general with

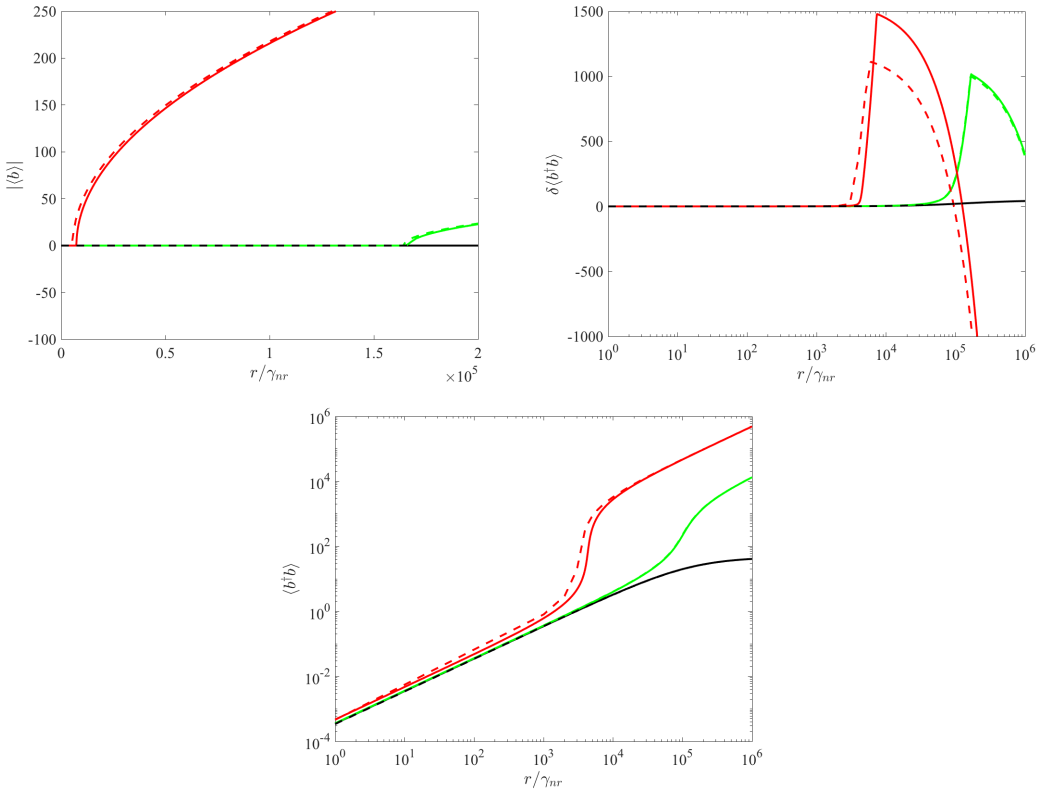

Figure 7.1: The coherent field amplitude (top left), photon number fluctuation (top right) and average photon number (bottom centre) as a function of the pump, respectively for the CIM (solid) and the multilevel model (dashed). The three devices considered are above - $N = 21$ (green) and $N = 40$ (red) - and below - $N = 20$ (black) - the critical number of emitters needed to achieve lasing.

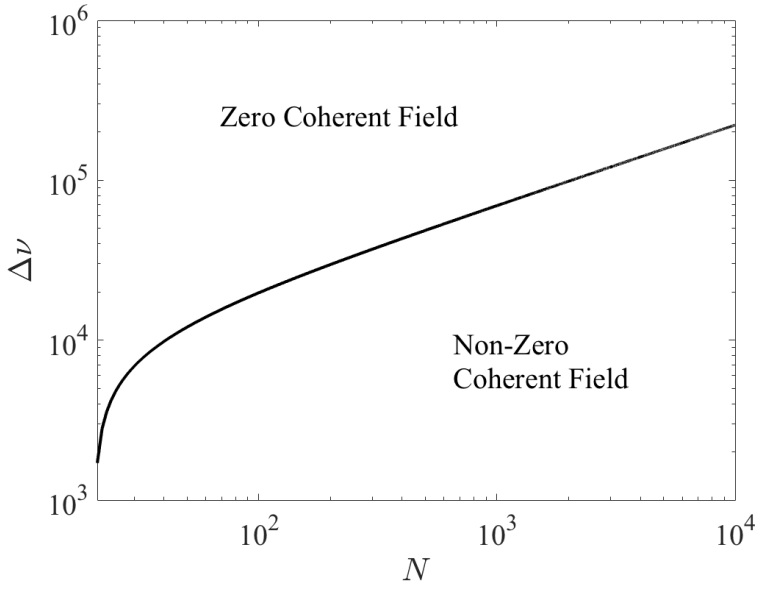

Figure 7.2: The system detuning $\Delta\nu$ as a function of the number of quantum dots, N, for lasing devices. The lower region corresponds to physical values of the detuning whereas the upper region corresponds to unphysical values of $\Delta\nu$, i.e., where the coherent filed is zero. The x-axis starts from $N = 21$; all devices corresponding to $1 \leq N < 21$ for the parameters considered are not capable of lasing.

respect to the both the single and multi electron models. For all lasing devices there is a limit to the amount of detuning present between the cavity and the transition frequency of the emitters. This increases as the number of emitters increases. Once the detuning is substantial enough such that we are in the upper region of Fig. 7.2 any coherent field dies out and there is no lasing.

7.4 Threshold dependence on β

From the analytic solution of the coherent field amplitude (see Appendix B) we are able to extract the solution to the value of the pump at laser threshold. Thus, we are able to understand how the pump threshold changes as a function of the system size characterised by β. Fig. 7.3 illustrates how the pump threshold changes as a function of β for different devices with changing N. As we move from the macroscopic, or thermodynamic, limit towards the microscopic limit we see that the input power

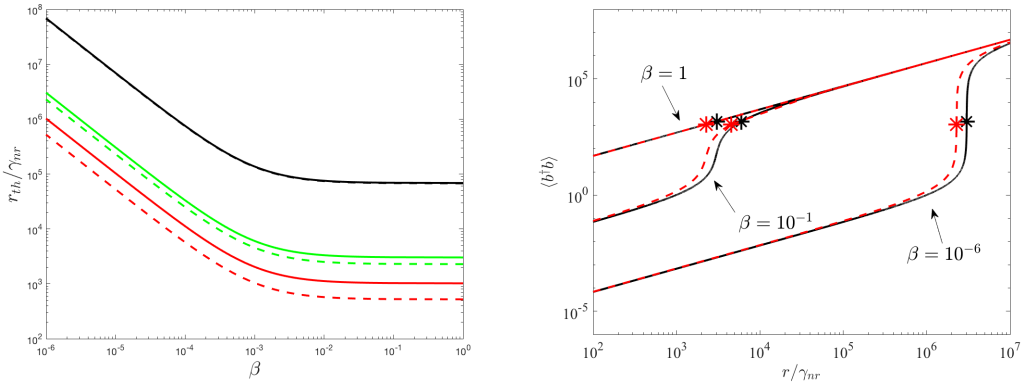

Figure 7.3: Left: The pump threshold for the CIM (solid) and multilevel model (dashed) as a function of the spontaneous emission factor, β, for different numbers of emitters N=(21:black, 10^2:green, 10^3:red). Right: I-O curve for a lasing device with $N = 40$ quantum dots for different values of β. The black (red) stars identify the laser bifurcation for the CIM (multilevel model).

required to reach the laser threshold for all devices decreases with a clear delimiting region between the thermodynamic and CQED limits occurring at the microscopic regime $\beta \approx 10^{-3}$. For any value of β the pump required to reach the laser threshold decreases as the number of emitters increases.

The right panel of Fig. 7.3 depicts the I-O curves for lasing devices, $N = 40$, where β decreases from the ideal nanolaser limit to typical macroscopic lasers. As we move towards the thermodynamic limit, but still firmly in the regime of small lasers we see that the characteristic s-shaped I-O curve begins to appear but that it is still smoothed out to the point that identifying the lasing threshold with confidence is still small. However, through LSA we know that the lasing bifurcation occurs at the knee of the upper branch signalling that all of the growth in the photon number comes as a result of incoherent emission. Reducing β still we see that well into the macroscopic laser regime the bifurcation point moves down from the upper branch and ultimately settles at the inflection point of the I-O curve. Thus, we find that the CIM confirms that the laser threshold of macroscopic devices occurs at the inflection point of the s-shaped curve on a log-log plot.

In summary, this chapter has highlighted that there are no significant differences between the single- and multi-electron models. Through LSA we have seen that the

condition required for instabilities to exist is the same for both models. Only when the two models are compared as functions of the pump do we see that the multi-electron model reaches threshold sooner than the single-electron model. For QD numbers just above the critical number the difference is not large, however, as the number of QDs is increased an appreciable difference between pump value at threshold emerges. We have also seen that in the thermodynamic limit the classical interpretation of laser threshold is recovered, i.e. the lasing bifurcation moves from the knee of the upper branch of the I-O to the inflection point.

Chapter 8

Conclusion

In conclusion, we have identified a gap in the theoretical modelling of nanolasers and developed a new class of quantum models that are capable of describing very well the behaviour of low- and high-β devices. Historically, REs have been used in the area of QED to model small lasers due to their simplicity and ability to describe emission above and below laser threhosld, but they fall short of being able to identify the threshold itself. Semiclassical approaches have been used to describe macroscopic lasers and are capable of identifying the laser threshold. However, they cannot give us any information about the incoherent emission below threshold. The models developed in Chapter 3 combine the unique features of the REs and semiclassical equations by including the variables needed to describe both incoherent *and* coherent emission. And as a result they have allowed us to observe the true laser threshold mathematically through bifurcation analysis in Chapter 5. This has allowed us to lay to rest the question regarding "thresholdless" lasers since even in the fundamental limit $\beta = 1$ there is a clear and well defined threshold. Without the inclusion of the coherent variables it would not be possible to observe the lasing bifurcation.

The usefulness of the CIM model does not stop at identifying the true laser threshold. We have also shown that it is capable of observing antibunched light below the laser threshold. Thus, in Chapter 6 we presented a simple experimental scheme that could take advantage of this quantum signature of light. The benefit of the antibunched light predicted by the CIM comes from the fact that it comes for "free". This is meant in

the sense that the antibunching is naturally produced compared with typical squeezed sources which are gained at the cost of complex experimental setups in order to degrade the macroscopic phase of the coherent source, i.e. above laser threshold.

Finally, we have also shown in Chapter 7 that the classical description of laser threshold is recovered by the CIM. For macroscopic lasers in the thermodynamic limit there is a sharp and almost discontinuous jump between the branches on the I-O plot which is taken to be the point of inflection of the I-O curve. It was shown that the laser bifurcation moves from the knee of the upper branch of the I-O curve towards the inflection point in the thermodynamic limit.

Appendix A

Non-identical emitters

A.1 The equations for non-identical emitters

The free energy and the light-matter interaction are given, in the Heisenberg picture, by the fully quantized Hamiltonian [5]

$$H = \hbar \sum_{q} \nu_q (b_q^\dagger b_q + \frac{1}{2}) + \sum_{q,n} [\varepsilon_{c,n} c_n^\dagger c_n + \varepsilon_{v,n} v_n^\dagger v_n - i\hbar (g_{nq} b_q c_n^\dagger v_n - g_{nq}^* b_q^\dagger v_n^\dagger c_n)], \quad \text{(A.1)}$$

where ν_q is the frequency of the $q-th$ mode of the laser cavity, $b_q, b_q^\dagger$ are the destruction and creation operators for $q-th$ mode photons. $\varepsilon_{c,n}$ and $\varepsilon_{v,n}$ are the energies of the electors in the conduction and valence level in the $n-th$ quantum dot and $c_n, c_n^\dagger$ and $v_n, v_n^\dagger$ are creation and destruction operators, respectively, for conduction and valence electrons of the $n-th$ quantum dot. The equations for $\langle c_n^\dagger c_n \rangle$, $\delta\langle b_q c_n^\dagger v_n \rangle$, $\delta\langle b_q^\dagger b_q \rangle$, $\langle b_q \rangle$, and $\langle v_n^\dagger c_n \rangle$ are:

$$d_t\langle c_l^\dagger c_l\rangle = -\gamma_{nr}\langle c_l^\dagger c_l\rangle + r(1-\langle c_l^\dagger c_l\rangle) - 2\sum_q \mathfrak{Re} g_{ql}(\delta\langle b_q c_l^\dagger v_l\rangle + \langle b\rangle\langle c_l^\dagger v_l\rangle), \tag{A.2}$$

$$\begin{aligned} d_t\delta\langle b_q c_l^\dagger v_l\rangle &= -[\gamma_q+\gamma+i(\nu_q-\Delta\varepsilon_l)]\delta\langle b c_l^\dagger v_l\rangle + g_{ql}^*[\langle c_l^\dagger c_l\rangle \\ &\quad + \delta\langle b_q^\dagger b_q\rangle(2\langle c_l^\dagger c_l\rangle - 1) - \langle c_l^\dagger v\rangle\langle v_l^\dagger c_l\rangle], \end{aligned} \tag{A.3}$$

$$d_t\delta\langle b_q^\dagger b_q\rangle = -2\gamma_q\delta\langle b_q^\dagger b_q\rangle + 2\sum_l \mathfrak{Re} g_{ql}\delta\langle b_q c_l^\dagger v_l\rangle, \tag{A.4}$$

$$d_t\langle b_q\rangle = -(\gamma_q + i\nu_q)\langle b_q\rangle + g_{ql}^* N\langle v_l^\dagger c_l\rangle, \tag{A.5}$$

$$d_t\langle v_l^\dagger c_l\rangle = -(\gamma + i\Delta\varepsilon_l)\langle v_l^\dagger c_l\rangle + \sum_q g_{ql}[\langle b_q\rangle(2\langle c_l^\dagger c_l\rangle - 1)], \tag{A.6}$$

where the dissipative terms are obtained with a Lindblad formalism [50, 51]. Neglecting intensities and field amplitudes of the non resonant modes $q \neq 0$ and eliminating adiabatically the correlations $\delta\langle b_q c_l^\dagger v_l\rangle$, we find that non resonant modes can be accounted for by the additional decay rate for the population γ_{nr}. Assuming that only one mode is resonant with the cavity and the N emitters coupled to the laser mode are identical [15, 40], leads to the simpler equations given to Eqs. (5.1) - (5.5) in Section 5, which give the dynamic of the system after a temporal transient in which the emitters' variables are equalized.

Appendix B

Effect of two-particle fermion incoherent variable

In the Comment [2], the authors claim that the laser threshold identified in Ref. [3] using a new coherent-incoherent model (CIM) is "unattainable" when the term $\sum_{n\neq l}\delta\langle c_l^\dagger v_l v_n^\dagger c_n\rangle$ is added to the equation for the photon assisted polarization $\delta\langle bc^\dagger v\rangle$. Moreover, they identify the classical polarization $|P|^2$ with $\sum_{n,l}\langle c_l^\dagger v_l v_n^\dagger c_n\rangle$ and on this basis claim that neglecting $\sum_{n\neq l}\delta\langle c_l^\dagger v_l v_n^\dagger c_n\rangle$ violates the quantum to classical correspondence.

In this reply we show that: 1) the claim that the threshold is "unattainable" for the model in [2] is factually wrong, the threshold exists and is observable; 2) correctly taking into account terms of the order of $\sum_{n\neq l}\delta\langle c_l^\dagger v_l v_n^\dagger c_n\rangle$ and the spatial nonlocality of this sum confirms that the CIM model provides accurate values of the laser threshold.

We reiterate that in nanolasers, terms like $\sum_{n\neq l}\delta\langle c_l^\dagger v_l v_n^\dagger c_n\rangle$ account for collective effects (CE) like superradiance, which, for the majority of devices, are not observed because of strong dephasing due to high carrier density screening [31]. It is shown in [34] that in the limit of strong polarisation dephasing $(\gamma_c/\gamma) \ll 1$ (where γ_c and γ are the cavity decay and dephasing rates, respectively) the correlations describing CE are negligible and that CE are only important in low-Q cavities where $(\gamma_c/\gamma) \geq 1$. Our model [3] matches the parameters of (GaAs-based) QDs most commonly used in nanolasers, with a very rapid decay of the intrinsic polarization [103] and negligible

polarization correlations.

We start our rebuttal from the claim that $|P|^2$ corresponds to $\sum_{n,l}\langle c_l^\dagger v_l v_n^\dagger c_n\rangle$. By imposing normal ordering on the operators we find

$$\sum_{n,l}\langle c_l^\dagger v_l v_n^\dagger c_n\rangle = \langle c_l^\dagger c_l\rangle - \sum_{n,l}\langle c_l^\dagger v_n^\dagger v_l c_n\rangle \tag{B.1}$$

where $\langle c_l^\dagger c_l\rangle$ is the excited state population and $\sum_{n,l}\langle c_l^\dagger v_n^\dagger v_l c_n\rangle$ is the sum of the expectation value of the product of polarisations between QDs placed in different positions, which is a spatially nonlocal term. As the classical polarization is a local function of position in the Maxwell-Bloch equations that is independent of the population, the presence of the population and of the nonlocal term above demonstrates that $\sum_{n,l}\langle c_l^\dagger v_l v_n^\dagger c_n\rangle$ does not correspond to $|P|^2$. The term that corresponds to the amplitude squared of the local polarization from the Maxwell-Bloch equations is instead the term $|\langle v^\dagger c\rangle|^2$, present in our model (see Eq. (2) in [3]) but arbitrarily and inconsistently removed from Eq. (1) in [2].

As for the equation for expectation value $\langle c_l^\dagger v_n^\dagger v_l c_n\rangle$, the correct form is

$$\begin{aligned} d_t\langle c_l^\dagger v_n^\dagger v_l c_n\rangle = &-(2\gamma + i\Delta\varepsilon)\langle c_l^\dagger v_n^\dagger v_l c_n\rangle \\ &+g_{ls}^*\big[\langle b_s^\dagger v_n^\dagger c_n\rangle(1-2\langle c_l^\dagger c_l\rangle) \\ &-2\langle v_n^\dagger c_n\rangle\langle b_s^\dagger c_l^\dagger c_l\rangle + 2\langle b_s^\dagger\rangle\langle c_l^\dagger c_l\rangle\langle v_n^\dagger c_n\rangle\big] \\ &+g_{ns}\big[\langle b_s c_l^\dagger v_l\rangle(1-2\langle c_n^\dagger c_n\rangle) \\ &-2\langle c_l^\dagger v_l\rangle\langle b_s c_n^\dagger c_n\rangle + 2\langle b_s\rangle\langle c_n^\dagger c_n\rangle\langle c_l^\dagger v_l\rangle\big] \end{aligned} \tag{B.2}$$

where the coefficients g_{ns} depend on the cavity-mode field at the position of the QDs [112]. The phase difference between QDs is not an issue in those terms containing products of coupling coefficients and polarization operators that belong to the same QD, as there is a phase invariance that allows one to eliminate the phases from the coupling coefficients. However, this is no longer the case for the driving terms in Eq. (B.2) that, as a result of the spatial nonlocality mentioned above, include products of the coupling coefficient of the l-th QD with the operators $v_n^\dagger c_n$ that correspond to

the polarization of the n-th QD. Neglecting these phase differences, as done in [2], means assuming that all QDs are identical, and that they lie on the intersection of an equiamplitude and an equiphase surface that depend on the cavity-mode field [112]. For vector solutions of Maxwell's equations, this is an extremely strict condition, which cannot be satisfied by all QDs especially in presence of physical boundary conditions.

We show in Fig. B.1 the effect of these assumptions on the position of the laser threshold and confirm the full validity of our model in [3]. The bifurcation point at the lowest value of pump (blue star) is obtained with the CIM, the one at the highest (black star) with the CIM plus the Eq. (1) given in [2]. Note that even in this case the bifurcation is present, although the model ignores a large number of terms of comparable size and, as a result, is unbalanced and unstable after the bifurcation. Including consistently [3] the same order variables as done in Eq. (B.2), but keeping the non physical assumption of [2] that all QDs have coupling coefficients with the same phase and amplitude, stabilizes the dynamic after the bifurcation and moves the threshold to the red star point in Fig. B.1. This is already much closer to the CIM threshold than to the version of the theory suggested in [2]. Assuming that amplitude and phase of the coupling coefficients are identical on only 90% of the QDs moves the threshold significantly closer to the CIM (red diamond). Finally, assuming that only 50% of the QDs have virtually the same coupling coefficients puts the bifurcation (red cross) very close to that of the CIM. In summary: bifurcations leading to coherent fields can always be observed, and the model of [3] is correct and of wide application contrary to what is claimed in [2].

We conclude our rebuttal of the Comment's analysis of Eq. (2) of our Letter by noting that neglecting $\delta\langle b^\dagger b c^\dagger c\rangle$ and $\delta\langle b^\dagger b v^\dagger v\rangle$ is the standard procedure with cluster expansions [47] truncated at the two-particle level where these terms are perturbative [31]. There is a further misunderstanding about the emission after the bifurcation in [3]. The bifurcation analysis carried out in [3] does not mean that the coherent field immediately takes over, only that a fraction of the photon field emerges with a coherent phase and single frequency.

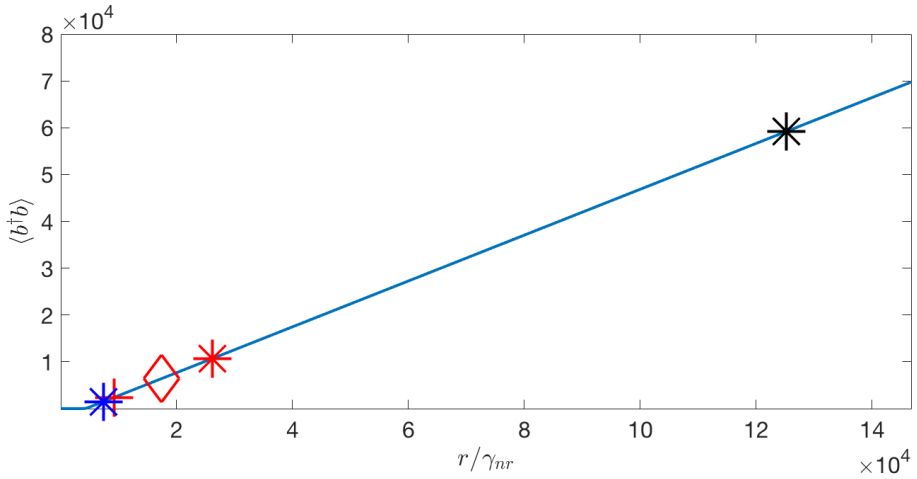

Figure B.1: Photon number versus pump for 40 QDs where the laser threshold of the CIM plus the equation given in [2] (black star) and CIM [3] (blue star) are shown. The red star corresponds to the bifurcation in the model which accounts for the variables ignored in [2]; the red diamond (red cross) shows the bifurcation point assuming that only 90% (50%) of the QDs have coupling coefficients with the same phase and amplitude. All parameter values are the same as in Ref. [3].

Appendix C

Analytic solutions

We present the analytic results of the non-lasing and lasing solutions. The following notation is used throughout: $\Gamma_c = \gamma + \gamma_c$, $\Delta_\Gamma = \gamma_c(\Gamma_c^2 + \Delta\nu^2)$, $\Gamma_n = \gamma_{nl} + \gamma_{nr}$, $\Gamma_t = 3\gamma_c + \gamma$ and $\Delta\Omega = \Delta\nu(1 - \frac{\gamma_c}{\Gamma_c})$. Parameter definitions are: light-matter coupling, g; cavity decay rate, γ_c; polarisation dephasing, γ; non-radiative decay, γ_{nr}; non-lasing decay, γ_{nl}; detuning, $\Delta\nu$; and the number of emitters, N.

C.1 Non-lasing solutions and $g^{(2)}(0)$

The photon number is given solely in terms of the system parameters:

$$\delta\langle b^\dagger b\rangle = \frac{1}{8|g|^2\gamma_c\Gamma_c}\{-(\Gamma_n + r)\Delta_\Gamma - |g|^2\Gamma_c[2\gamma_c + N(\Gamma_n - r)] + F^{1/2}\} \tag{C.1}$$

where F is

$$\begin{aligned} F = (N\Gamma_c|g|^2 + \Delta_\Gamma)^2\Gamma_n^2 - 2(N\Gamma_c|g|^2 + \Delta_\Gamma)((N\Gamma_c|g|^2 - \Delta_\Gamma)r - 2|g|^2\gamma_c\Gamma_c)\Gamma_n \\ +(N\Gamma_c|g|^2 - \Delta_\Gamma)^2r^2 + 12\gamma_c\Gamma_c g^2(N\Gamma_c|g|^2 + \frac{\Delta_\Gamma}{3})r + 4|g|^4\gamma_c^2\Gamma_c^2. \end{aligned} \tag{C.2}$$

The carrier density can then be given as a function of the photon number:

$$\langle c^\dagger c\rangle = \frac{1}{\Gamma_n + r}\left(r - 2\,\frac{\gamma_c\delta\langle b^\dagger b\rangle}{N}\right). \tag{C.3}$$

Appendix C. Analytic solutions

Of the three fundamental variables within the non-lasing solutions the photon polarisation is the only complex variable and we give it in terms of the carrier density $\langle c^\dagger c\rangle$ and photon number $\delta\langle b^\dagger b\rangle$

$$\delta\langle bc^\dagger v\rangle = \frac{g^*(\Gamma_c - i\Delta\nu)}{\Gamma_c^2 + \Delta\nu^2}\Big[\langle c^\dagger c\rangle + \delta\langle b^\dagger b\rangle(2\langle c^\dagger c\rangle - 1)\Big]. \tag{C.4}$$

The equation for $g^{(2)}(0)$ is given by

$$g^{(2)}(0) = 2 + \frac{\delta\langle b^\dagger b^\dagger bb\rangle}{\delta\langle b^\dagger b\rangle^2} \tag{C.5}$$

where $A = \delta\langle b^\dagger b^\dagger bb\rangle$ and $B = \delta\langle b^\dagger b\rangle^2$ from chapter 5. As seen from Eq. C.5, in order to calculate $g^{(2)}(0)$ one must solve higher order correlation functions up to the four-particle level of the type $\delta\langle b^\dagger b^\dagger bb\rangle$. These higher order correlations couple to the photon assisted polarisation through the three-particle carrier-photon correlation $\delta\langle b^\dagger bc^\dagger c\rangle$. As an approximation we neglect correlations greater than two-particles from the dynamics of $\langle c^\dagger c\rangle$, $\delta\langle b^\dagger b\rangle$ and $\delta\langle bc^\dagger c\rangle$. This turns out to be a very good approximation as can be seen from the purple triangle markers in Fig. 1 of chapter 5. With the aforementioned approximation we find analytically the solution to $\delta\langle b^\dagger b^\dagger bb\rangle$ as a function of the carrier density and photon number

$$\delta\langle b^\dagger b^\dagger bb\rangle = \frac{C}{D} \tag{C.6}$$

where

$$\begin{aligned} D = \{&(2\gamma_c + \gamma_{nr})[Ng^2\Gamma_t(2\langle c^\dagger c\rangle - 1) - \gamma_c(\Delta\nu^2 + \Gamma_t^2)] \\ &- 4g^2\Gamma_t\gamma_c(2\delta\langle b^\dagger b\rangle + 1)\}(\Delta\nu^2 + \Gamma_c^2)^2 \end{aligned} \tag{C.7}$$

and

$$C = 4|g|^2\Gamma_t\Big\{4|g|^2N\Gamma_c^2(2\gamma_c+\gamma_{nr})(\delta\langle b^\dagger b\rangle^2\langle c^\dagger c\rangle^2+\delta\langle b^\dagger b\rangle\langle c^\dagger c\rangle^2)+[2\gamma_c(\Gamma_c^2+\Delta\nu^2)^2 \\ -4|g|^2N\Gamma_c^2(2\gamma_c+\gamma_{nr})]\delta\langle b^\dagger b\rangle^2\langle c^\dagger c\rangle+|g|^2N\Gamma_c^2(2\gamma_c+\gamma_{nr})\langle c^\dagger c\rangle^2+2\gamma_c(\Delta\nu^2 \\ +\Gamma_c^2)^2\delta\langle b^\dagger b\rangle^3+[\gamma_c(\Gamma_c^2+\Delta\nu^2)^2+|g|^2N\Gamma_c^2(2\gamma_c+\gamma_{nr})]\delta\langle b^\dagger b\rangle^2 \\ +[-2|g|^2N\Gamma_c^2(2\gamma_c+\gamma_{nr})+\gamma_c(\Delta\nu^2+\Gamma_c^2)^2]\delta\langle b^\dagger b\rangle\langle c^\dagger c\rangle\Big\} \tag{C.8}$$

C.2 Analytic laser solutions

The *Modulus of* the Coherent field (solution exists only when $|\langle b\rangle| \geq 0$) is given by

$$|\langle b\rangle| = \frac{1}{\gamma|g|\Delta_\Gamma}\left[\frac{(N|g|^2\Gamma_c^2-\gamma\Delta_\Gamma)\Delta_\Gamma r-(N|g|^2\Gamma_c^2+\gamma\Delta_\Gamma)(\Delta_\Gamma\Gamma_n+2|g|^2\Gamma_c^2)}{4(N-1)}(\gamma^2+\Delta\Omega^2)N\right]^{\frac{1}{2}} \tag{C.9}$$

where the expectation value of the coherent field is defined as $\langle b\rangle = |\langle b\rangle|e^{-i(\Omega t+\phi)}$; the phase ϕ is undetermined and there are in principle an infinite set of solutions. Note that for $\Omega \neq 0$ the bifurcation is a Hopf bifurcation; however, $e^{-i\Omega t}$ can be factored out and the bifurcation reduced to a pitchfork bifurcation. The steady state solution of the carrier density is

$$\langle c^\dagger c\rangle = \frac{1}{2}\left(1+\frac{\gamma\Delta_\Gamma}{N|g|^2\Gamma_c^2}\right) \tag{C.10}$$

and the standard polarisation of the medium is defined as

$$\langle v^\dagger c\rangle = \frac{g}{\gamma+i\Delta\Omega}\langle b\rangle(2\langle c^\dagger c\rangle-1). \tag{C.11}$$

The solution of the intensity correlation is

$$\delta\langle b^\dagger b\rangle = \frac{N}{2\gamma_c}\left[r-(\Gamma_n+r)\langle c^\dagger c\rangle-\frac{2|g|^2\gamma}{\gamma^2+\Delta\Omega^2}|\langle b\rangle|^2(2\langle c^\dagger c\rangle-1)\right], \tag{C.12}$$

and the solution to the photon assisted polarisation is

$$\delta\langle bc^{\dagger}v\rangle = \frac{g^{*}}{\Gamma_c + i\Delta\nu}\Big[\langle c^{\dagger}c\rangle + \delta\langle b^{\dagger}b\rangle(2\langle c^{\dagger}c\rangle - 1) - |\langle v^{\dagger}c\rangle|^2\Big]. \tag{C.13}$$

C.3 The value of the pump at the laser threshold

C.4 Phase diagrams with detuning

In Fig. C.1 the affect of detuning is shown for devices with different values of β. In both cases we find that increasing the detuning shifts the value of N_c towards larger values of N. This is confirmed by inspecting the numerator in Eq. 5.12 where increasing the detuning results in a larger value of N to satisfy the physical conditions put in place for r.

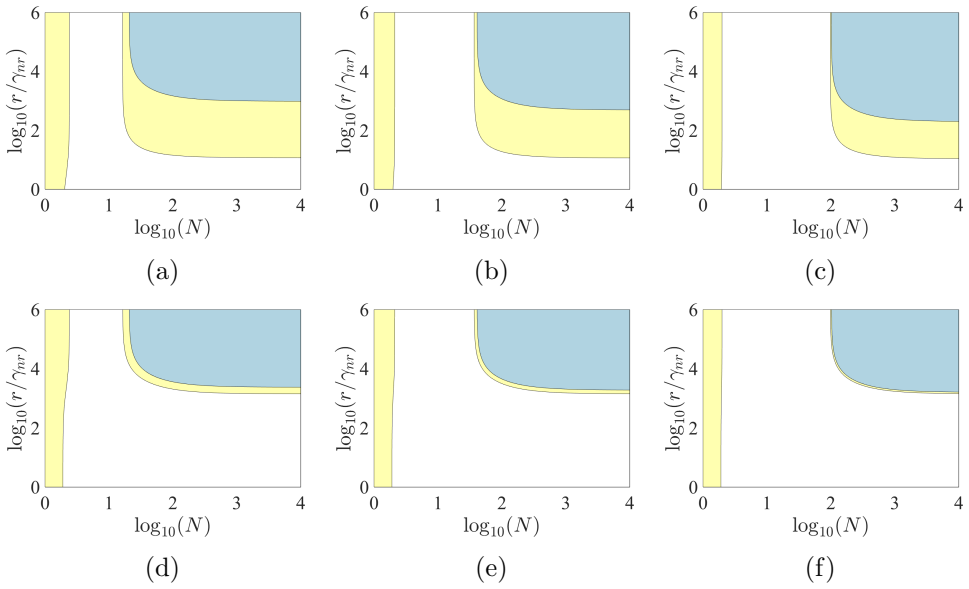

Figure C.1: Phase diagrams for devices with changing detuning and spontaneous emission factor $\beta = 1$ (a)-(c), and 7×10^{-4} (d)-(f). The detunings are in (a) and (d), $\Delta\nu = 10^{12}s^{-1}$; (b) and (e), $\Delta\nu = 10^{13}s^{-1}$; (c) and (f), $\Delta\nu = 2 \times 10^{13}s^{-1}$. Common to both values of β is the increase of N_c as the detuning increases, and in both cases we find that the extent of the anti-bunching regime as a function of the pump is reduced. Parameters: $\gamma = 10^{13}s^{-1}$, $\gamma_c = 10^{10}s^{-1}$, $\gamma_{nr} = 10^{9}s^{-1}$, and $g = 7 \times 10^{10}s^{-1}$. The white region corresponds to the thermal regime; yellow to the anti-bunching regime; and blue to the lasing regime.

Appendix D

Numerical tests

A comparison between the analytic solutions and the numerical steady state values in Fig. D.1 shows a perfect agreement indicating that the numerical simulations are on firm ground.

Following on from this in Fig. D.2 we give the steady state solutions of the photon number versus the pump rate r for two cases: the first assumes all emitters to be identical and as such only requires one equation for each variable for N emitters, Eqs. (1-5) in chapter 5(solid lines); and in the second case we modify the model to include N equations for $\langle c^\dagger c\rangle$, $\langle v^\dagger c\rangle$ and $\delta\langle bc^\dagger v\rangle$ (dashed lines). In the latter case, we include values for the detuning $\Delta\nu$ and coupling coefficient g that are varied by up to 10% of the values used to obtain the solid curves (the random numbers used were drawn from a uniform distribution). In both cases, which are initiated with random initial conditions, after a temporal transient the variables steady state values converge establishing a collective state.

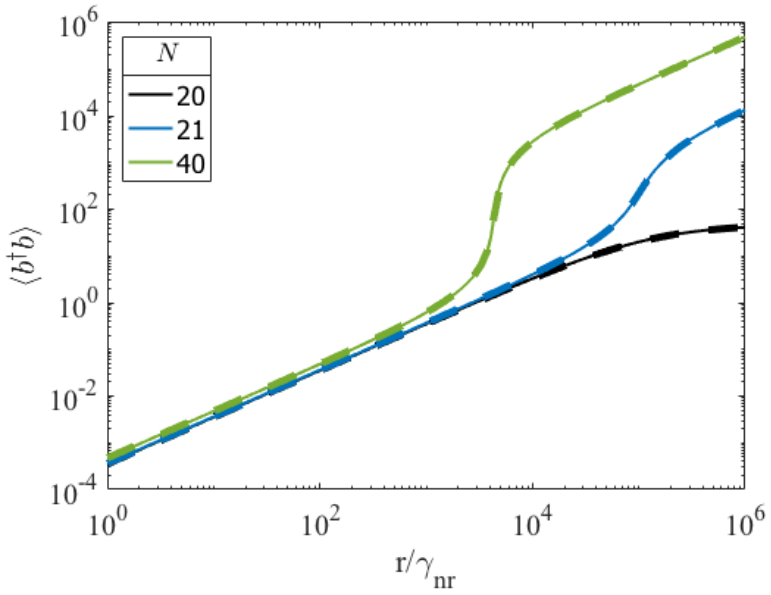

Figure D.1: Comparison of the analytic (solid lines) and numerical (dashed lines) results of the intensity versus pump rate r for different numbers of emitters. Parameters: $\beta = 7 \times 10^{-4}$, $\gamma_{nl} = 1.4 \times 10^{12} s^{-1}$, $\gamma_l = 9.68 \times 10^8 s^{-1}$, $\gamma = 10^{13} s^{-1}$, $\gamma_c = 10^{10} s^{-1}$, $\gamma_{nr} = 10^9 s^{-1}$ and $g = 7 \times 10^{10} s^{-1}$.

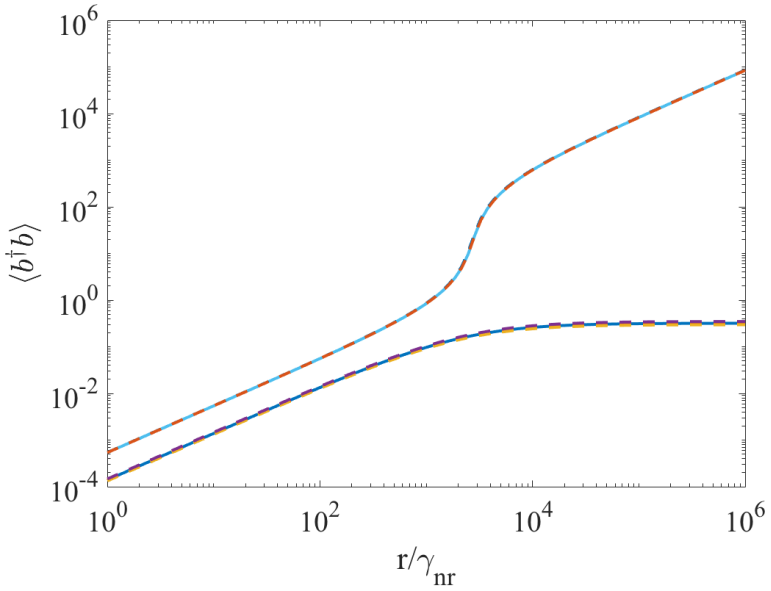

Figure D.2: Intensity as a function of the pump rate for five quantum dots where in the lower branch $g = 7 \times 10^{10} s^{-1}$ ($\beta = 7 \times 10^{-4}$) and in the upper branch $g = 25 \times 10^{10} s^{-1}$ ($\beta = 9 \times 10^{-3}$) . The dashed lines are obtained from simulations where g and $\Delta\nu$ are varied randomly up to 10% of the values used to obtain the solid lines. Parameters: $\gamma = 10^{13} s^{-1}$, $\gamma_c = 10^{10} s^{-1}$, $\gamma_{nr} = 10^9 s^{-1}$, $\gamma_{nl} = 1.4 \times 10^{12} s^{-1}$ and $\Delta\nu = 10^{12} s^{-1}$.

Appendix E

Comparison with rate and master equation models

We make here a direct comparison between Eqs. (5.1) - (5.5) in Section 5 with a fully quantized master equation [23] and a cQED model [15] for the case of $\beta = 1$. Under the condition of $\beta = 1$ the results of the master equation are calculated via Eq. 8a and Eq. 36 from [23]. The main difference between Eqs. (5.1) - (5.5) and the master equation given in [23] is that the master equation derives from the two rate equation variables, intensity and excited carrier number, and does not include the medium polarisation. Without the polarisation there are only correlations between the carrier number and intensity, whereas we have correlations between the field and polarisation of the medium which leads to the anti-bunching. Fig. E.1 shows a comparison of the intensity obtained through Eqs. (5.1) - (5.5) of chapter 5 with a fully quantized master equation. The divergence between the red and the blue curves in Fig. E.1a for low pump rate can be accounted for by noting that in [15] the term responsible for spontaneous emission is nonlinear whereas in Eq. (2) of chapter 5 it is linear resulting from the assumption of two-level emitters.

In Fig. E.2 we show the intensity versus pump above and below threshold. Using the usual procedure of linear extrapolation of the intensity down to zero and comparing the value of the laser threshold with that obtained from Eqs. (5.1) - (5.5) in chapter 5. The red star marks the position of the lasing threshold calculated from Eqs. (5.1) - (5.5) from

Appendix E. Comparison with rate and master equation models

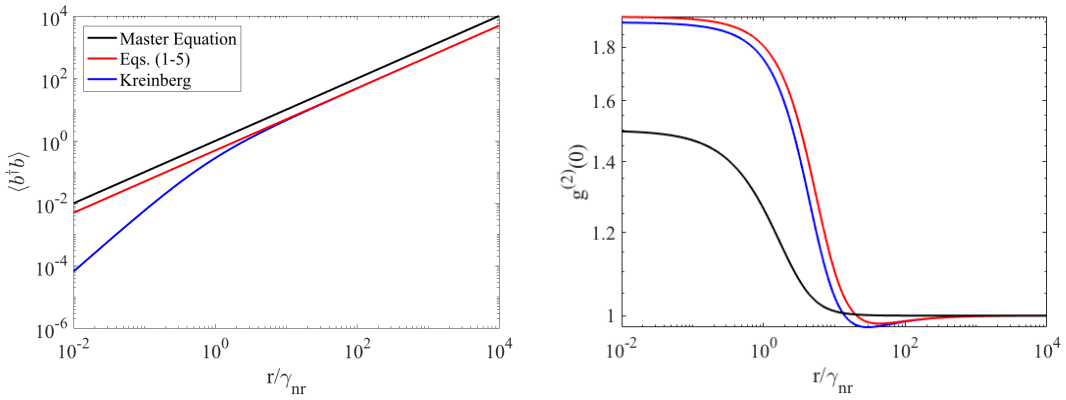

(a) (b)

Figure E.1: Comparison of the intensity between a fully quantized master equation and Eqs. (5.1) - (5.5) in Section 5 where $\beta = 1$. Parameters: $g = 7 \times 10^{10} s^{-1}$, $\gamma = 10^{13} s^{-1}$, $\gamma_c = 10^{10} s^{-1}$, $\gamma_{nr} = 10^{9} s^{-1}$ and $N = 40$.

chapter 5 and the blue triangle marks where the linear extrapolation of the intensity crosses zero. There are two points to note: the value of the laser threshold predicted from linear extrapolation occurs at the point of initial rapid growth of photons; and, the position of the red star occurs after this rapid growth in photon number.

Finally, in Fig. E.3 we compare the intensity versus pump highlighting the differences between Eqs. (5.1) - (5.5) in chapter 5 with and without the fast variables and rate equations derived from Eqs. (5.1) - (5.5). In order to derive rate equations we consider only the slow variables and insert the adiabatic solution of the photon assisted polarisation into the equations for the carrier population and intensity. The rate equations and the model with only the slow variables produce almost identical values of the intensity. The inclusion of the fast variables changes slightly the intensity, with the change being more significant for larger values of the decay of the medium polarisation, γ, with respect to the cavity decay rate, γ_c. The key role that the fast variables play, is that without them it is not possible neither to define a laser threshold nor to determine the well defined lasing frequency that is established after this bifurcation.

Appendix E. Comparison with rate and master equation models

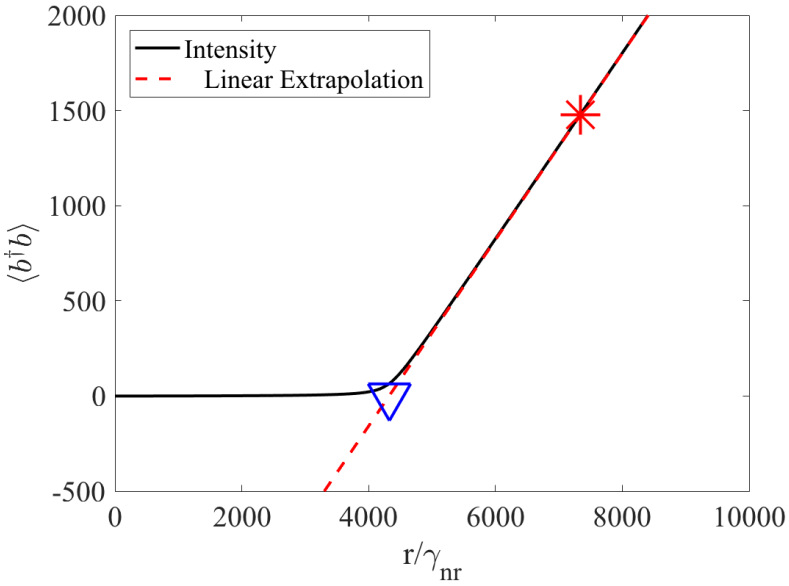

Figure E.2: Linear plot of intensity versus pump rate r (black) and the extrapolated fit (red) where $\beta = 7 \times 10^{-4}$. The red star marks the position of the lasing bifurcation and the blue triangle shows where the linear extrapolation of the intensity crosses zero. Parameters: $g = 7 \times 10^{10} s^{-1}$, $\gamma = 10^{13} s^{-1}$, $\gamma_c = 10^{10} s^{-1}$, $\gamma_{nr} = 10^{9} s^{-1}$, $\gamma_{nl} = 1.4 \times 10^{12} s^{-1}$ and $N = 40$.

Appendix E. Comparison with rate and master equation models

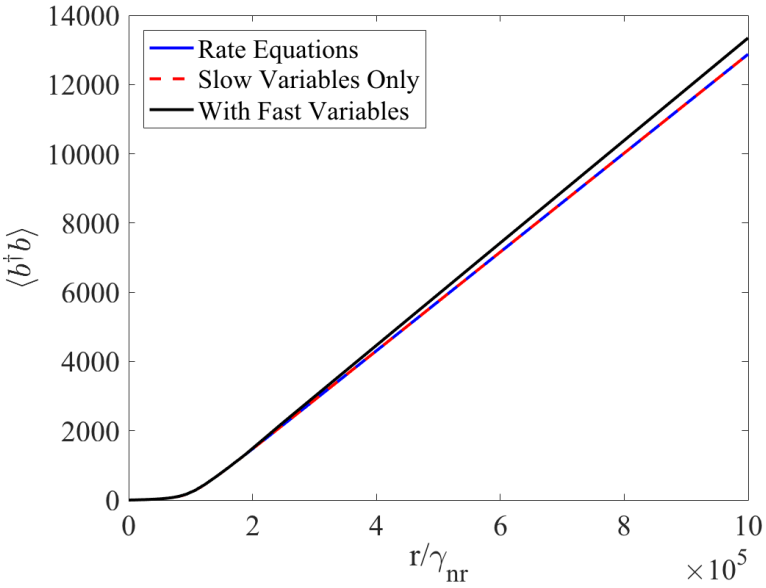

Figure E.3: Comparison of the intensity versus pump for three cases: rate equations; the model with only slow variables; and the model with slow and fast variables. Parameters: $g = 7 \times 10^{10} s^{-1}$, $\gamma = 10^{13} s^{-1}$, $\gamma_c = 10^{10} s^{-1}$, $\gamma_{nr} = 10^9 s^{-1}$, $\gamma_{nl} = 1.4 \times 10^{12} s^{-1}$ and $N = 21$. The equations corresponding to ignoring the fast variables are Eqs. (5.1) - (5.3); with the fast variables computed with Eqs. (5.4) - (5.5).

Appendix F

Lasing and non-lasing decay rates

Performing an adiabatic elimination of the photon-assisted polarisation where $q \neq s$ allows us to formally introduce the decay rate into non-lasing modes [31]. The steady state solution of the photon-assisted polarisation describing non-lasing modes is given by

$$\delta\langle b_q c_l^\dagger v_l\rangle = \frac{g_{ql}^*}{\gamma_q + \gamma - i\Delta\nu}\Big[\langle c_l^\dagger c_l\rangle + \delta\langle b_q^\dagger b_q\rangle\Big(2\langle c_l^\dagger c_l\rangle - 1\Big) - |\langle c_l^\dagger v_l\rangle|^2\Big]. \tag{F.1}$$

This can be simplified by noting that spontaneous emission will be the dominant mode in which photons are generated, thus we can neglect the term proportional to the photon number in the non-lasing mode. In the same vein, we neglect coherent processes which are also negligible in this regime therefore the standard polarisation also drops out of the above equation

$$\delta\langle b_q c_l^\dagger v_l\rangle = \frac{g_{ql}^*}{\gamma_q + \gamma - i\Delta\nu}\langle c_l^\dagger c_l\rangle. \tag{F.2}$$

Extracting the lasing mode from the sum in the equation for the carrier population yields

$$\frac{d}{dt}\langle c_l^\dagger c_l\rangle = -\gamma_{nr}\langle c_l^\dagger c_l\rangle - 2\Re g_{ns}\Big(\delta\langle b_s c_l^\dagger v_l\rangle + \langle b_s\rangle\langle v_l^\dagger c_l\rangle\Big) - 2\Re\sum_{q\neq s} g_{nq}\delta\langle b_q c_l^\dagger v_l\rangle \tag{F.3}$$

where we again set to zero coherent processes which are negligible within the non-lasing mode. Substituting the steady state photon-assisted polarisation in to the above

equation results in

$$\frac{d}{dt}\langle c_l^\dagger c_l\rangle = -(\gamma_{nl}+\gamma_{nr})\langle c_l^\dagger c_l\rangle - 2\Re g_{ns}\Big(\delta\langle b_s c_l^\dagger v_l\rangle + \langle b_s\rangle\langle v_l^\dagger c_l\rangle\Big) \tag{F.4}$$

where we define the decay rate into non-lasing modes as

$$\gamma_{nl} = \frac{2}{\hbar}\Re\sum_{q\neq s}\frac{|g_{ql}|^2}{\gamma_q+\gamma-i\Delta\nu}. \tag{F.5}$$

The carriers in the system are generated by an incoherent pump injection directly into the excited state by means of thermalisation of the upper states. Thus r is the pump rate per emitter and Nr is the total pump rate of the system

$$\frac{d}{dt}\langle c_l^\dagger c_l\rangle = -(\gamma_{nl}+\gamma_{nr})\langle c_l^\dagger c_l\rangle + r(1-\langle c_l^\dagger c_l\rangle) - 2\Re g_{ns}\Big(\delta\langle b_s c_l^\dagger v_l\rangle + \langle b_s\rangle\langle v_l^\dagger c_l\rangle\Big). \tag{F.6}$$

Bibliography

[1] J. Mork and G.L. Lippi. Rate equation description of quantum noise in nanolasers with few emitters. *Applied Physics Letters*, 112(14):141103, 2018.

[2] AA Vyshnevyy and D Yu Fedyanin. Comment on" thermal, quantum antibunching and lasing thresholds from single emitters to macroscopic devices". *arXiv preprint arXiv:2106.15242*, 2021.

[3] Mark Anthony Carroll, Giampaolo D'Alessandro, Gian Luca Lippi, Gian-Luca Oppo, and Francesco Papoff. Thermal, quantum antibunching and lasing thresholds from single emitters to macroscopic devices. *Physical Review Letters*, 126(6):063902, 2021.

[4] Koen Schakenraad, Andreas S Biebricher, Maarten Sebregts, Brian Bensel, Erwin JG Peterman, Gijs JL Wuite, Iddo Heller, Cornelis Storm, and Paul Schoot. Hyperstretching dna. *Nature communications*, 8(1):2197, 2017.

[5] W.W Chow, F. Jahnke, and C. Gies. Emission properties of nanolasers during the transition to lasing. *Light: Science & Applications*, 3:e201, 2014.

[6] Stefan Strauf and Frank Jahnke. Single quantum dot nanolaser. *Laser & Photonics Reviews*, 5(5):607–633, 2011.

[7] H. Yokoyama and S. D. Brorson. Rate equation analysis of microcavity laser. *J. Appl. Phys.*, 66:4801–4805, 1989.

[8] Arthur L Schawlow and Charles H Townes. Infrared and optical masers. *Physical Review*, 112(6):1940, 1958.

[9] TH Maiman. Stimulated optical radiation in ruby. *Nature*, 187(4736):493–494, 1960.

[10] U.L. Andersen, G. Leuchs, and C. Silberhorn. Continuous-variable quantum information processing. *Laser & Photonics Reviews*, 4(3):337–354, 2010.

[11] Carlton M Caves. Quantum-mechanical noise in an interferometer. *Physical Review D*, 23(8):1693, 1981.

[12] B. P. Abbott. Observation of gravitational waves from a binary black hole merger. *Phys. Rev. Lett.*, 116:061102, Feb 2016.

[13] T Sakaguchi, F Koyama, and K Iga. Vertical cavity surface-emitting laser with an algaas/alas bragg reflector. *Electronics Letters*, 24(15):928–929, 1988.

[14] Yong-Hee Lee, JL Jewell, Axel Scherer, SL McCall, JP Harbison, and LT Florez. Room-temperature continuous-wave vertical-cavity single-quantum-well microlaser diodes. *Electronics Letters*, 25(20):1377–1378, 1989.

[15] S. Kreinberg, W.W. Chow, J. Wolters, C. Schneider, C. Gies, F. Jahnke, S. Höfling, M. Kamp, and S. Reitzenstein. Emission from quantum-dot high-β microcavities: transition from spontaneous emission to lasing and the effects of superradiant emitter coupling. *Light: Science & Applications*, 6:e17030, 2017.

[16] M Langner, M Sudzius, H Fröb, VG Lyssenko, and K Leo. Selective excitation of laser modes in an organic photonic dot microcavity. *Applied Physics Letters*, 95(9):091109, 2009.

[17] M.T. Hill and M.C. Gather. Advances in small lasers. *Nature Photon.*, 8:908–918, 2014.

[18] Bobby Jones, Shohini Ghose, James P Clemens, Perry R Rice, and Leno M Pedrotti. Photon statistics of a single atom laser. *Physical Review A*, 60(4):3267, 1999.

[19] Anders Moelbjerg, Per Kaer, Michael Lorke, Bjarne Tromborg, and Jesper Mørk. Dynamical properties of nanolasers based on few discrete emitters. *IEEE Journal of Quantum Electronics*, 49(11):945–954, 2013.

[20] Anthony Mark Fox, Mark Fox, et al. *Quantum optics: an introduction*, volume 15. Oxford university press, 2006.

[21] HBG Casimir and D Polder. The influence of retardation on the london-van der waals forces. *Physical Review*, 73(4):360, 1948.

[22] Cun-Zheng Ning. What is laser threshold? *IEEE Journal of Selected Topics in Quantum Electronics*, 19(4):1503604–1503604, 2013.

[23] Perry R Rice and HJ Carmichael. Photon statistics of a cavity-qed laser: A comment on the laser–phase-transition analogy. *Physical Review A*, 50(5):4318, 1994.

[24] I.D.W. Samuel and G.A. Turnbull E.B. Namdas. How to recognize lasing. *Nature Photonics*, 3:546–549, 2009.

[25] F De Martini and GR Jacobovitz. Anomalous spontaneous–stimulated-decay phase transition and zero-threshold laser action in a microscopic cavity. *Physical review letters*, 60(17):1711, 1988.

[26] H Jeff Kimble, Mario Dagenais, and Leonard Mandel. Photon antibunching in resonance fluorescence. *Physical Review Letters*, 39(11):691, 1977.

[27] J. Wiersig *et al.* Direct observation of correlations between individual photon emission events of a microcavity laser. *Nature*, 460:245–250, 2009.

[28] XT Zou and L Mandel. Photon-antibunching and sub-poissonian photon statistics. *Physical Review A*, 41(1):475, 1990.

[29] Hermann Haken. Theory of coherence of laser light. *Physical Review Letters*, 13(11):329, 1964.

[30] Gunnar Bjork and Yoshihisa Yamamoto. Analysis of semiconductor microcavity lasers using rate equations. *IEEE Journal of Quantum Electronics*, 27(11):2386–2396, 1991.

[31] C. Gies, J. Wiersig, M. Lorke, and F. Jahnke. Semiconductor model for quantum-dot-based microcavity lasers. *Phys. Rev. A*, 75:013803, 2007.

[32] Larry A Coldren, Scott W Corzine, and Milan L Mashanovitch. *Diode lasers and photonic integrated circuits*, volume 218. John Wiley & Sons, 2012.

[33] Mackillo Kira and Stephan W Koch. *Semiconductor quantum optics*. Cambridge University Press, 2011.

[34] Igor E Protsenko, Alexander V Uskov, Emil C André, Jesper Mørk, and Martijn Wubs. Quantum langevin approach for superradiant nanolasers. *New J. Phys.*, 23(6):063010, 2021.

[35] G Sęk, P Poloczek, K Ryczko, J Misiewicz, A Löffler, JP Reithmaier, and A Forchel. Photoreflectance determination of the wetting layer thickness in the in x ga 1- x as/ ga as quantum dot system for a broad indium content range of 0.3–1. *Journal of applied physics*, 100(10):103529, 2006.

[36] F Klopf, JP Reithmaier, and A Forchel. Highly efficient gainas/(al) gaas quantum-dot lasers based on a single active layer versus 980 nm high-power quantum-well lasers. *Applied Physics Letters*, 77(10):1419–1421, 2000.

[37] H Diwu and B Arda. *Quantum Dot Lasers. ECE580 Term project 2007, University of Rochester; downloaded from: http://www2.ece.rochester.edu/courses/ECE580/docs/Quantum_Dot_Lasers.pdf on 09/12/2020.*, 2007.

[38] Mohammadreza Shahzadeh and Mohammad Sabaeian. The effects of wetting layer on electronic and optical properties of intersubband p-to-s transitions in strained dome-shaped inas/gaas quantum dots. *AIP Advances*, 4(6):067113, 2014.

[39] Cf., e.g., specification sheets for: Single mode VCSEL 980 ±1nm TO46 and TEC.

[40] Galan Moody, Mawussey Segnon, Isabelle Sagnes, Rémy Braive, Alexios Beveratos, Isabelle Robert-Philip, Nadia Belabas, Frank Jahnke, Kevin L Silverman, Richard P Mirin, et al. Delayed formation of coherence in the emission dynamics of high-q nanolasers. *Optica*, 5(4):395–401, 2018.

[41] A very close value is given in [44] $\sigma_{QD} \approx 5 \times 10^9 cm^{-2}$. notice that the devices of ref [40] and ref [44] are built in different facilities: the first ones at the c2n in paris, the second one at the university of wurzburg. the agreement with the estimates proves the reliability of the processes. other sources give $\sigma_{QD} \approx \times 10^{11} cm^{-2}$, thus the value chosen for the discussion is a reasonable mid-range estimate.

[42] Anthony E Siegman. Lasers university science books. *Mill Valley, CA*, 37(208):169, 1986.

[43] A. Kaganskiy, S. Kreinberg, X. Porte, and S. Reitzenstein. Micropillar lasers with site-controlled quantum dots as active medium. *Optica*, 6(4):404–409, 2019.

[44] Steffen Karl Holzinger. *Quantum Dot Microlasers subject to Delayed Optical Feedback*. Technische Universitaet Berlin (Germany), 2019.

[45] R.M. Ma and R.F. Oulton. Applications of nanolasers. *Nature Nanotechnol.*, 14:12–22, 2019.

[46] L.M. Narducci and N.B. Abraham. *Laser Physics and Laser Instabilities*. (World Scientific, 1988.

[47] J. Fricke. Transport Equations Including Many-Particle Correlations for an Arbitrary Quantum System: A General Formalism. *Annals of physics*, 252:479–498, 1996.

[48] T. Feldtmann, L. Schneebeli, M. Kira, and S. W. Koch. Quantum theory of light emission from a semiconductor quantum dot. *Phys. Rev. B*, 73:155319, 2006.

[49] H. Solari, M. Natiello, and G. Mindlin. *Nonlinear Dynamics: A Two-way Trip from Physics to Math*. CRC Press, 1996.

[50] M. Florian, C. Gies, F. Jahnke, H.A.M. Leymann, and J. Wiersig. Equation-of-motion technique for finite-size quantum-dot systems: Cluster expansion method. *Phys. Rev. B*, 87:165306, 2013.

[51] H.A.M. Leymann, A. Foerster, and J. Wiersig. Expectation value based equation-of-motion approach for open quantum systems: A general formalism. *Phys. Rev. B*, 89:085308, 2014.

[52] W.W Chow and F. Jahnke. On the physics of semiconductor quantum dots for applications in lasers and quantum optics. *Prog. Quantum. Electron.*, 37:109–184, 2014.

[53] M. Takiguchi *et al.* Systematic study of thresholdless oscillation in high-β buried multiple-quantum-well photonic crystal nanocavity lasers. *Opt. Express*, 24:3441–3450, 2016.

[54] Y. Ota, M. Kakuda, K. Watanabe, S.Iwamoto, and Y. Arakawa. Thresholdless quantum dot nanolaser. *Opt. Express*, 25:19981–19994, 2017.

[55] S.T. Jagsch *et al.* A quantum optical study of thresholdless lasing features in high-β nitride nanobeam cavities. *Nature Commun.*, 9:564, 2018.

[56] C. Gies, F. Jahnke, and W.W. Chow. Photon antibunching from few quantum dots in a cavity. *Phys. Rev. A*, 91:061804(R), 2015.

[57] A. Lebreton, I. Abram, R. Braive, I. Sagnes, I. Robert-Philip, and A. Beveratos. Unequivocal differentiation of coherent and chaotic light through interferometric photon correlation measurements. *Phys. Rev. Lett.*, 110:163603, Apr 2013.

[58] S. M. Ulrich, C. Gies, S. Ates, J. Wiersig, S. Reitzenstein, C. Hofmann, A. Löffler, A. Forchel, F. Jahnke, and P. Michler. Photon statistics of semiconductor microcavity lasers. *Phys. Rev. Lett.*, 98:043906, Jan 2007.

[59] D.A.B. Miller. Attojoule optoelectronics for low-energy information processing and communications. *J. Lightwave Technol.*, 35:346–396, 2017.

[60] P. Melentiev *et al.* Plasmonic nanolaser for intracavityspectroscopy and sensorics. *Appl. Phys. Lett.*, 111:213104, 2017.

[61] M.I. Stockman. Nanoplasmonic sensing and detection. *Science*, 348:287–288, 2015.

[62] A.H. Fikouras, M. Schubert, M. Karl, J.D. Kumar, S.J. Powis, A. Di Falco, and M.C. Gather. Non-obstructive intracellular nanolasers. *Nature Commun.*, 9:4817, 2018.

[63] J. Große, M. von Helversen, A. Koulas-Simos, M. Hermann, and S. Reitzenstein. Development of site-controlled quantum dot arrays acting as scalable sources of indistinguishable photons. *APL Photonics*, 5:096107, 2020.

[64] F. Papoff and B. Hourahine. Geometrical Mie theory for resonances in nanoparticles of any shape. *Opt. Express*, 19:21432–21444, 2011.

[65] K. Imura, K. Ueno, H. Misawa, H. Okamoto, D. McArthur, B. Hourahine, and F. Papoff. Plasmon modes in single gold nanodiscs. *Opt. Express*, 22:12189–12199, 2014.

[66] D. McArthur, B. Hourahine, and F. Papoff. Enhancing ultraviolet spontaneous emission with a designed quantum vacuum. *Opt. Express*, 25:12189–12199, 2017.

[67] D. McArthur and F. Papoff. Gap enhanced fluorescence as a road map for the detection of very weakly fluorescent emitters from visible to ultraviolet. *Sci. Rep.*, 7:14191, 2017.

[68] D. McArthur, A.M. Yao, and F. Papoff. Scattering of light with angular momentum from an array of particles. *Phys. Rev. Research*, 2:013100, 2020.

[69] Mark Anthony Carroll, Giampaolo D'alessandro, Gian Luca Lippi, Gian-Luca Oppo, and Francesco Papoff. Photon-number squeezing in nano-and microlasers. *Applied Physics Letters*, 119(10):101102, 2021.

[70] V Giovannetti, S Lloyd, and L Maccone. Photonic quantum simulators. *Nat Photonics*, 5:222–229, 2011.

[71] Y Yamamoto and HA Haus. Preparation, measurement and information capacity of optical quantum states. *Reviews of Modern Physics*, 58(4):1001, 1986.

[72] Junaid Aasi, J Abadie, BP Abbott, Richard Abbott, TD Abbott, MR Abernathy, Carl Adams, Thomas Adams, Paolo Addesso, RX Adhikari, et al. Enhanced sensitivity of the ligo gravitational wave detector by using squeezed states of light. *Nature Photonics*, 7(8):613–619, 2013.

[73] Hui Wang, Jian Qin, Si Chen, Ming-Cheng Chen, Xiang You, Xing Ding, Y-H Huo, Ying Yu, C Schneider, Sven Höfling, et al. Observation of intensity squeezing in resonance fluorescence from a solid-state device. *Physical Review Letters*, 125(15):153601, 2020.

[74] Y Yamamoto, S Machida, and O Nilsson. Stiskanje amplitude u laserskom oscilatoru potisnutom bukom pumpe. *Fiz. Vlč. A*, 34(5):4025–4042, 1986.

[75] Susumu Machida and Yoshihisa Yamamoto. Ultrabroadband amplitude squeezing in a semiconductor laser. *Physical review letters*, 60(9):792, 1988.

[76] A. Heidmann, R. J. Horowicz, S. Reynaud, E. Giacobino, C. Fabre, and G. Camy. Observation of quantum noise reduction on twin laser beams. *Phys. Rev. Lett.*, 59:2555–2557, Nov 1987.

[77] D. T. Smithey, M. Beck, M. Belsley, and M. G. Raymer. Sub-shot-noise correlation of total photon number using macroscopic twin pulses of light. *Phys. Rev. Lett.*, 69:2650–2653, Nov 1992.

[78] P. Sharapova, A. M. Pérez, O. V. Tikhonova, and M. V. Chekhova. Schmidt modes in the angular spectrum of bright squeezed vacuum. *Phys. Rev. A*, 91:043816, Apr 2015.

[79] Vasily V. Temnov and Ulrike Woggon. Photon statistics in the cooperative spontaneous emission. *Opt. Express*, 17(7):5774–5782, Mar 2009.

[80] D. Meiser and M. J. Holland. Intensity fluctuations in steady-state superradiance. *Phys. Rev. A*, 81:063827, Jun 2010.

[81] Justin G Bohnet, Zilong Chen, Joshua M Weiner, Dominic Meiser, Murray J Holland, and James K Thompson. A steady-state superradiant laser with less than one intracavity photon. *Nature*, 484(7392):78–81, 2012.

[82] OA Shcherbina, GA Shcherbina, M Manceau, S Vezzoli, L Carbone, M De Vittorio, A Bramati, E Giacobino, MV Chekhova, and G Leuchs. Photon correlations for colloidal nanocrystals and their clusters. *Optics letters*, 39(7):1791–1794, 2014.

[83] Georg Harder, Tim J Bartley, Adriana E Lita, Sae Woo Nam, Thomas Gerrits, and Christine Silberhorn. Single-mode parametric-down-conversion states with 50 photons as a source for mesoscopic quantum optics. *Physical review letters*, 116(14):143601, 2016.

[84] Luo Qi, Mathieu Manceau, Andrea Cavanna, Fabian Gumpert, Luigi Carbone, Massimo de Vittorio, Alberto Bramati, Elisabeth Giacobino, Lukas Lachman, Radim Filip, et al. Multiphoton nonclassical light from clusters of single-photon emitters. *New Journal of Physics*, 20(7):073013, 2018.

[85] T Boulier, M Bamba, A Amo, C Adrados, A Lemaitre, E Galopin, I Sagnes, J Bloch, C Ciuti, E Giacobino, et al. Polariton-generated intensity squeezing in semiconductor micropillars. *Nature communications*, 5(1):1–7, 2014.

[86] Marc-Antoine Lemonde, Nicolas Didier, and Aashish A Clerk. Antibunching and unconventional photon blockade with gaussian squeezed states. *Physical Review A*, 90(6):063824, 2014.

[87] H. Flayac and V. Savona. Unconventional photon blockade. *Phys. Rev. A*, 96:053810, Nov 2017.

[88] H. J. Snijders, J. A. Frey, J. Norman, H. Flayac, V. Savona, A. C. Gossard, J. E. Bowers, M. P. van Exter, D. Bouwmeester, and W. Löffler. Observation of the unconventional photon blockade. *Phys. Rev. Lett.*, 121:043601, Jul 2018.

[89] Jesper Mork and Kresten Yvind. Squeezing of intensity noise in nanolasers and nanoleds with extreme dielectric confinement. *Optica*, 7(11):1641–1644, 2020.

[90] A Musial, K Zolnacz, N Srocka, O Kravets, J Große, J Olszewski, K Poturaj, G Wojcik, P Mergo, K Dybka, et al. Plug&play fibre-coupled 73 khz single-photon source operating in the telecom o-band. adv. *Quantum Technol*, 202000018, 2020.

[91] Shuichiro Inoue, Hitoshi Ohzu, Susumu Machida, and Yoshihisa Yamamoto. Quantum correlation between longitudinal-mode intensities in a multimode squeezed semiconductor laser. *Phys. Rev. A*, 46:2757–2765, Sep 1992.

[92] F. Marin, A. Bramati, E. Giacobino, T. C. Zhang, J. Ph. Poizat, J. F. Roch, and P. Grangier. Squeezing and intermode correlations in laser diodes. *Phys. Rev. Lett.*, 75:4606–4609, Dec 1995.

[93] MJ Freeman, H Wang, Duncan G Steel, R Craig, and DR Scifres. Wavelength-tunable amplitude-squeezed light from a room-temperature quantum-well laser. *Optics letters*, 18(24):2141–2143, 1993.

[94] Hailin Wang, Michael J. Freeman, and Duncan G. Steel. Squeezed light from injection-locked quantum well lasers. *Phys. Rev. Lett.*, 71:3951–3954, Dec 1993.

[95] J. Kitching, A. Yariv, and Y. Shevy. Room temperature generation of amplitude squeezed light from a semiconductor laser with weak optical feedback. *Phys. Rev. Lett.*, 74:3372–3375, Apr 1995.

[96] W. H. Richardson, S. Machida, and Y. Yamamoto. Squeezed photon-number noise and sub-poissonian electrical partition noise in a semiconductor laser. *Phys. Rev. Lett.*, 66:2867–2870, Jun 1991.

[97] MJ Freeman, H Wang, DG Steel, R Craig, and DR Scifres. Amplitude-squeezed light from quantum-well lasers. *Optics letters*, 18(5):379–381, 1993.

[98] Mengxin Ren, Baohua Jia, Jun-Yu Ou, Eric Plum, Jianfa Zhang, Kevin F MacDonald, Andrey E Nikolaenko, Jingjun Xu, Min Gu, and Nikolay I Zheludev. Nanostructured plasmonic medium for terahertz bandwidth all-optical switching. *Advanced Materials*, 23(46):5540–5544, 2011.

[99] Jun-Yu Ou, Eric Plum, Jianfa Zhang, and Nikolay I. Zheludev. Giant nonlinearity of an optically reconfigurable plasmonic metamaterial. *Advanced Materials*, 28(4):729–733, 2016.

[100] Pavel N Melentiev, Anton E Afanasiev, Artur A Kuzin, Andrey S Baturin, and Victor I Balykin. Giant optical nonlinearity of a single plasmonic nanostructure. *Optics express*, 21(12):13896–13905, 2013.

[101] S. Houver, A. Lebreton, T. A. S. Pereira, G. Xu, R. Colombelli, I. Kundu, L. H. Li, E. H. Linfield, A. G. Davies, J. Mangeney, J. Tignon, R. Ferreira, and S. S. Dhillon. Giant optical nonlinearity interferences in quantum structures. *Science Advances*, 5(10):eaaw7554, 2019.

[102] H. J. Carmichael. Photon antibunching and squeezing for a single atom in a resonant cavity. *Phys. Rev. Lett.*, 55:2790–2793, Dec 1985.

[103] Mitsuru Sugawara, Kohki Mukai, Yoshiaki Nakata, Hiroshi Ishikawa, and Akira Sakamoto. Effect of homogeneous broadening of optical gain on lasing spectra in self-assembled $\mathrm{in}_x\mathrm{ga}_{1-x}\mathrm{As}$/GaAs quantum dot lasers. *Phys. Rev. B*, 61:7595–7603, Mar 2000.

[104] L Mandel. Non-classical states of the electromagnetic field. T12:34–42, jan 1986.

[105] Luiz Davidovich. Sub-poissonian processes in quantum optics. *Rev. Mod. Phys.*, 68:127–173, Jan 1996.

[106] A. M. van der Lee, N. J. van Druten, M. P. van Exter, J. P. Woerdman, J.-Ph. Poizat, and Ph. Grangier. Critical petermann K factor for intensity noise squeezing. *Phys. Rev. Lett.*, 85:4711–4714, Nov 2000.

[107] Rajiv Boddeda, Quentin Glorieux, Alberto Bramati, and Simon Pigeon. Generating strong anti-bunching by interfering nonclassical and classical states of light. *Journal of Physics B: Atomic, Molecular and Optical Physics*, 52(21):215401, 2019.

[108] Kevin Zelaya, Sanjib Dey, and Véronique Hussin. Generalized squeezed states. *Physics Letters A*, 382(47):3369–3375, 2018.

[109] Y. Yamamoto and S. Machida. High-impedance suppression of pump fluctuation and amplitude squeezing in semiconductor lasers. *Phys. Rev. A*, 35:5114–5130, Jun 1987.

[110] S. Machida, Y. Yamamoto, and Y. Itaya. Observation of amplitude squeezing in a constant-current–driven semiconductor laser. *Phys. Rev. Lett.*, 58:1000–1003, Mar 1987.

[111] Shuichiro Inoue, Seema Lathi, and Yoshihisa Yamamoto. Longitudinal-mode-partition noise and amplitude squeezing in semiconductor lasers. *JOSA B*, 14(11):2761–2766, 1997.

[112] N Baer, C Gies, J Wiersig, and F Jahnke. Luminescence of a semiconductor quantum dot system. *The European Physical Journal B-Condensed Matter and Complex Systems*, 50(3):411–418, 2006.